Development of Positron Annihilation Spectroscopy Techniques Applied to Damaged Polyimide Film

Jacob Solomon Hughes

A thesis submitted for the degree of
Doctor of Philosophy of
The Australian National University

December, 2018

Declaration

This thesis is an account of research undertaken between February 2013 and December 2018 at The Research School of Physics and Engineering, College of Physical and Mathematical Sciences, The Australian National University, Canberra, Australia. Except where acknowledged in the customary manner, the material presented in this thesis is, to the best of my knowledge, original and has not been submitted in whole or part for a degree in any university.

Acknowledegments

A Ph. D. is a gigantic undertaking and there are many people that I would like to acknowledge and express my heartfelt thanks to.

Firstly, I would like to thank James Sullivan, my primary supervisor, the chair of my supervisory committee, and the leader of the Positron Group at ANU. James' direction and support were paramount in the undertaking this work.

I would like to thank David Sprouster, who provided expertise in materials science and helped design the experimental programme for this work, as well as great mentoring and guidance.

I would like to thank Stephen Buckman not only for his role on my supervisory committee, but additionally for his role as a teacher in the Honours programme in the year before I began my Ph. D.

I would like to acknowledge and thank the members of the positron group at the Australian National University (in no particular order): Tamara Babij, Daniel Murtagh, Colin Campbell, David Stevens, Simon Armitage, and Josh Mahacek. Ross Tranter and Stephen Battison, the technical staff, were invaluable help and a continual source of support.

Cormac Corr and Sam Cousens from the Department of Plasma Physics helped with the use of MAGPIE and generously spent a lot of their own time babysitting me and the Kapton samples I was exposing to plasma.

Johannes Postler helped kick start all of the digital measurement efforts.

Gregory Lane at the Department of Nuclear Physics provided me with great advice in spectroscopy and HPGe detectors.

Finally, my thanks go to the espresso machine in the positron laboratory, that is to this day the hardest working member of the positron group. The laboratory and group members would surely fall to ruin without the daily support of this under-appreciated paragon of caffeinated beverages.

Abstract

Studying and understanding the internal structure of materials is important to development of device quality materials with well-defined electrical and mechanical properties. More and more, modern materials for highly optimised applications are manufactured material composites, or processed in some way. To understand macroscopic properties exhibited by these materials often atomic or nano scale changes need to be characterised and understood, as they can be the drivers for these effects.

Positron annihilation spectroscopy (PAS) is an established analytical technique used to investigate the internal structure of materials, as the different techniques are non-destructive and sensitive at the molecular (sub-nanometre) level. Developing high quality positron spectroscopy experiments can aid in the understanding of the evolution of materials over time in damaging environments, or precisely monitor material behaviour during fabrication and processing. The information obtained from PAS can identify the underlying causes of desirable macroscopic material properties and inform the design and manufacture of these materials for better performance.

At the Australian National University, the positron research group has developed positron annihilation lifetime spectroscopy (PALS) which relates the time taken for an implanted positron to annihilate inside a material to defect size and concentration. This thesis outlines the implementation of a complementary PAS technique added to the positron materials beamline, Doppler broadening of annihilation radiation (DBAR), which provides additional information on the chemical environment at positron annihilation sites.

The successful implementation of the DBAR experiment was used to characterise ion implanted and plasma exposed Kapton polyimide, in conjunction with existing positron techniques. The damage study explored the effects of damage similar to environmental exposure in long term space missions, where Kapton components from satellites or spacecraft interact with trapped ion plasmas inside the Earth's magnetic field, planetary atmospheres, and the solar wind.

Contents

List of Figures

Chapter 1

Introduction

The body of work presented in this thesis has been divided into two main sections. Firstly, this work covers the design, implementation, and characterisation of a positron annihilation spectroscopy experiment added to the established positron materials beamline in the positron group at the Australian National University. Secondly, the suite of positron annihilation spectroscopy measurements are used to characterise Kapton, a polyimide used in spacecraft shielding, that has been damaged by ion implantation and plasma exposure, in a manner related to the environmental conditions that are found in our solar system and likely satellite orbit paths.

The positron materials beamline at the Australian National University makes use of the positron annihilation lifetime spectroscopy technique (PALS), which correlates the lifetime of a positron implanted into a material to the internal structure of that particular material. The implanted positrons are sensitive to damage to the material in the form of vacancies, pores, and voids, however a single measurement requires several hours to complete. The additional experimental technique to be implemented examines the Doppler broadening of annihilation radiation (DBAR), which measures the momentum of annihilation photons within material targets. By implementing the DBAR technique a complementary and supportive measurement can be made in significantly less time, which augments the information gained from the existing positron annihilation lifetime spectroscopy technique already in use.

Following the implementation and characterisation of the Doppler broadening of annihilation radiation technique, the experiment will be used to characterise Kapton polyimide samples relevant to spacecraft applications. The polyimide samples, which are used for thermal and electrical insulation in spacecraft, will be damaged to varying degrees by ion implantation and exposure to plasma in a manner which relates to the type of damage

that could occur in the galactic environment or within atmosphere of a planet in the solar system. The measurements aim to begin an investigation into not only the effects of ion implantation at different preparation temperatures, but how any induced damage is influenced by exposure to plasma. The suite of conditions are designed to mimic the harsh space environment that Kapton would be exposed to, while providing a set of experiments that can characterise the damage found.

1.1 Characterisation of Materials

The manipulation of the electrical and mechanical properties of a material can be performed by processing techniques that affect the base material at the molecular level, yet still produce large scale changes. Well known examples of nanoscale material changes that have important macroscopic effects are doped semiconductors. These materials are extremely important for electronic devices, and are manufactured by introducing small percentages of dopant species, which can dramatically change how these semiconductors behave. Controlling the amount of dopants as a stoichiometric parameter will determine whether these electrical properties manifest as desired: too little or too much and this doped silicon will not function as desired and be useless.

Similarly to using dopants, using ions to damage a material can also change its macroscopic properties, as the implantation process damages the target material and contaminates the target with the implanted species. Careful control of the target material, implanted ion species, and implantation dose can transform the target material. An example of this is the processing of organic polymer materials into molecular filters using ion implantation.

Damage to materials can often be a slow process which builds up over time, especially when the damage is primarily from the environment in which the material operates. In these cases chemical reactions can drive damage processes through exposed surfaces interacting with the substances in the environment. Using high resolution techniques to analyse these materials at different stages of environmental degradation, we can attempt to determine which particular processes drive damage, as well as finding the likely outcomes of this damage. The changes to specific properties can be characterised as a function of environmental exposure, and measures taken to mitigate or avoid these reactions.

The nanoscale changes that create macroscopic effects require a sensitivity of material preparation and characterisation, and to be fully controlled the effects need to be well understood. A key technique used for this type of study is positron annihilation spectroscopy (PAS). PAS is a highly sensitive, high resolution, non-destructive technique which is capable of sensing changes to materials at the atomic level.

Developing quality PAS experiments can help us to understand and improve material fabrication methods, and lead to better device quality materials.

Chapter 2

Positron Annihilation Spectroscopy

Positron annihilation spectroscopy (PAS) is a technique used in condensed matter and materials physics studies to learn about the internal structure of a particular material. The wider field of PAS is made up of several different experiment types, which each exploit a particular facet of the physics surrounding positron annihilation in order to reveal information about a sample.

To fully understand and interpret the information in the results of PAS techniques, it is first important to understand the fundamental properties of the positron and mechanics in positron-matter interaction.

This chapter will detail the physics involved in positron-matter interaction, in particular focusing in topics relevant to positron annihilation spectroscopy experiments. For these positron spectroscopy techniques, the experimental method, data acquisition, and data interpretation will be discussed, detailing the information obtained with each technique.

2.1 The Positron

The positron is the anti-particle counterpart to the electron and it is a charged lepton, meaning it is an elementary particle with spin 1/2 which has a charge of $+1e$.

The discovery of the positron is relatively recent and the origins of the positron begin in 1929 with the publication of Dirac's paper *The Quantum Theory of the Electron* [1]. The Dirac equation allowed for negative energy solutions, which could not be discarded due to the quantum nature of the problem, unlike some negative energy solutions obtained

in classical mechanics. Early interpretations of these negative energy solutions caused uncertainty in the scientific community at the time, and initially no-one had a universally satisfactory explanation.

Throughout 1929 Dirac continued his work on these problems, with growing interest and input from other physicists from around the world. Notably, at this time German physicist Weyl attempted to reconcile gravitation and mass with the electromagnetic field, using the Dirac equation, but failed [2]. The promising clue from his work points at these "negative energy electrons" having the same mass as electrons. Dirac remained concerned by the implications of his work so far. It appeared as though electrons could freely jump from positive energy states to negative ones, which would have the effect of flipping their charge, violating conservation of charge [3].

In 1930, Dirac suggests that the negative energy solutions could in fact be protons, despite the huge difference in mass [4]. This suggestion is rebuked by Oppenheimer in a letter, who comments that allowing protons and electrons to annihilate would make all atoms very unstable, and since we observe a matter rich, stable universe, this cannot be the case [5].

A new suggestion is put forward by Dirac in 1931 in the paper *Quantised Singularities in the Electromagnetic Field*. Negative energy states must not be protons, thus this is a new particle, yet to be observed: "A hole, if there was one, would be a new kind of particle, unknown to experimental physics, having the same mass and opposite charge to an electron" [6]. In parallel to the theoretical prediction of the positron from Dirac, the experimental discovery of the positron was attributed to Carl Anderson. From 1930 to 1933, Carl Anderson was working for Millikan observing charged particles in cloud chambers. Amongst other observations, he found unusual particles which curved in a magnetic field like positively charged species, yet were unlike protons in that they left light tracks through the chamber, much more like lightweight electrons.

To dispel any doubt on this unreported phenomena, a lead plate was installed in the cloud chamber in order to slow incoming particles and high energy cosmic rays. The "wrongly curving electrons" remained visible despite this shielding. The anti-electron had been found.

The results of Anderson's hard work was published in 1933, in a paper entitled *The*

Positive Electron. The 'positron' was suggested by the journal's editor as a more elegant name for this new particle [7].

In the same year, Blackett and Occhialini confirmed Anderson's work [8], and Anderson was awarded the Nobel Prize in Physics for his discovery in 1936.

In more recent work, further interpretations of particles and antiparticles have emerged as the field of quantum mechanics evolves. Through CPT symmetry the positron is equivalently an electron moving backwards through time [9, 10].

2.1.1 Positron Annihilation

One of the most significant events in antimatter-matter interaction is annihilation. When annihilation occurs, the rest mass energy of the interacting particle pair is released as various products, with total energy related through Einstein's famous equation:

$$E^2 = m_0^2 c^4 + p^2 c^2 \tag{2.1}$$

where m_0 is the rest mass of the particle, c is the speed of light, and p is the particle momentum.

In general, the products from annihilation can vary, depending on the rest mass energy of the annihilating particle-antiparticle pair and the specific interaction that takes place. In the case of positron annihilation, the total rest mass energy is approximately 1022eV ($2 \times m_e$), and the annihilation products are photons. For other antimatter species, the annihilation products are dependent on the energy released in the annihilation event and the products can be much more complex. In the case of proton-antiproton annihilation, for instance, the initial products are pions which then decay in a particle cascade [11, 12].

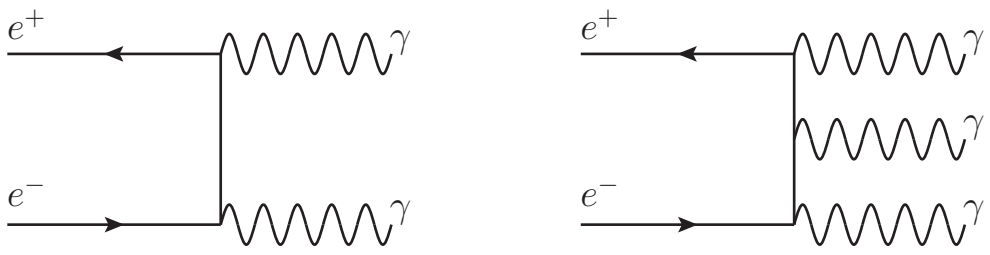

(a) Two gamma annihilation (b) Three gamma annihilation

Figure 2.1: Feynman diagrams of positron-electron annihilation

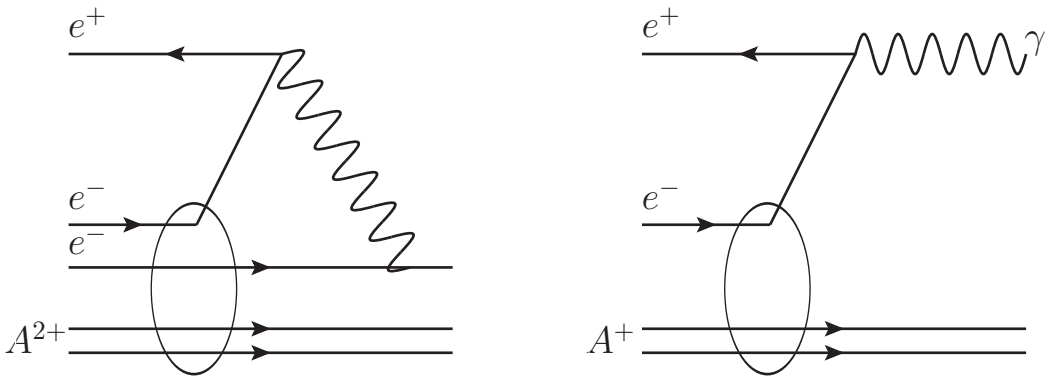

(a) Radiationless annihilation (b) One gamma annihilation

Figure 2.2: Feynman diagrams of less probable positron-electron annihilation

Two photon annihilation events in electron-positron annihilation are the most common products, each photon taking half the total energy and angular momentum of the system. higher numbers of photon products are also possible, but the probability decreases as the number of photons increases. Three photon annihilation is the next most probable after two photon annihilation, but still occurs frequently enough to provide an experimentally significant background signal. The probability of three photon annihilation compared to two photon was first calculated by Ore and Powell in 1949 [13] to be approximately 1/370, and figure 2.1 details the Feynman diagrams of these annihilation cases.

The two photon annihilation case is most useful for experimental physics, as at low energy the two photons are emitted almost co-linearly, with their energy approximately half the total energy from annihilation, or $m_e c^2 = 511\text{keV}$. This characteristic annihilation signal fingerprints positron-electron annihilation and exploiting this allows experiments to be conducted.

Three photon annihilation products cannot easily be used effectively for gathering information from positron-electron annihilation, and these photons will typically make up the low energy background of the 511keV photopeak. Removing the three photon background can often improve experimental resolution in positron experiments that make use of two photon events, and this is frequently done using detectors arranged in coincidence arrangements.

Radiationless, or one gamma, decays can take place, but have a very low probability of occurring, requiring the positron-electron pair to interact with an atom or ion. Figure

2.2 illustrates these rarer processes, showing the required atomic interaction.

2.1.2 Positronium

Positronium (chemical symbol Ps) is a quasi-stable hydrogenic bound state of a positron and electron and the system is electrically neutral. The idea was conceived somewhat jointly between 1937 and 1945 by Ruark [14] and Wheeler [15]. Wheeler's paper investigated the "...structure, means of formation, and modes of decay ..." of "polyelectrons", a term Wheeler used to describe positronium and further combinations of bound electrons and positrons [15]. Experimental evidence of the existence of positronium was found by Martin Deutsch working at Massachusetts Institute of Technology [16].

Although a hydrogen-like atom, positronium differs from normal matter atoms in many significant ways. The bound Ps atom is unstable as the positron-electron pair will eventually decay through annihilation, a decay channel not accessible to normal atomic structures. The ground state lifetime of the positronium atom is determined by the spin alignment of the electron and positron, and excited state lifetimes can be significantly different.

Rather than a very light electron bound to a much more massive single proton nucleus, both particles in positronium have the same mass: that of an electron. The significant mass difference gives positronium an inter-particle distance of four times that of hydrogen, and the energy levels of the Ps system are half those of hydrogen, and results in the binding energy of $\simeq 6.8$eV.

In the general case of positrons in materials, the electron density inside most metals is too high for positronium formation to occur (as annihilation processes will dominate), so this predominantly occurs in non-metallic solid materials. Positronium formation can be induced in a material by creating large enough regions of low electron density, such as pores and large defects.

Positronium formation in gas phase targets is dependent on the gas species, and often positronium formation cross sections are quantities of interest in positron-gas scattering experiments.

Spin states of Positronium

When positronium forms in the ground state, two different states are possible depending on the alignment of the spin of the positron and electron. The annihilation rates of these spin states was calculated first by Ore and Powell in 1949 [13].

In the singlet spin state ($S = 0$), the electron and positron spins are anti-parallel $\langle\uparrow\downarrow\rangle$. This state is known as para-positronium, and has a 125 picosecond lifetime before annihilation (annihilation rate $\simeq$ 8GHz).

The triplet state ($S = 1$), the positron spins are parallel $\langle\uparrow\uparrow\rangle$. This state is known as ortho-positronium, and has a 142 nanosecond lifetime before annihilation (annihilation rate $\simeq$ 7MHz).

The annihilation rates of positronium are important to material science. The 125 picosecond lifetime from para-positronium self-annihilation is often too short to resolve with most experiments, however the 142 nanosecond lifetime from ortho-positronium self-annihilation is quite easily observed and fingerprints the formation of positronium within a material. The ortho-positronium lifetime also marks an upper limit for positron lifetimes inside a material, however lifetimes close to this limit are very rarely observed.

Exotic states of Positronium

Although there is some difficulty in creating and using positronium due to scarcity of antimatter and the short lifetime of Ps, excited states of Ps can be created and used for experiments. For instance, there are a series of experiments being conducted to examine the effects of gravity on antimatter, using Rydberg states of positronium, since they have lifetimes of 100s of microseconds [17].

As positronium is a neutral particle, forming a focused Ps beam for experiments is harder than for charged particle beams and often comes with much lower count rates than positron beam experiments. One method for forming Ps beams is to form Ps^-, the positronium negative ion, and use electrostatic and magnetic techniques to focus the beam, like any other charged particle experiment. The additional electron is removed at the last possible stage before it meets the target through photo-ionisation with a tuned laser pulse, forming a focused Ps beam [18].

2.2 Positron Sources for Experiments

Positrons are most frequently found as the product of radioactive decay, known as the β^+ particle. Pair production can also be use to generate positrons, either in electron accelerators or nuclear reactors. In either case, creating a positron source suitable for precision experiments in physics can be a demanding task alone.

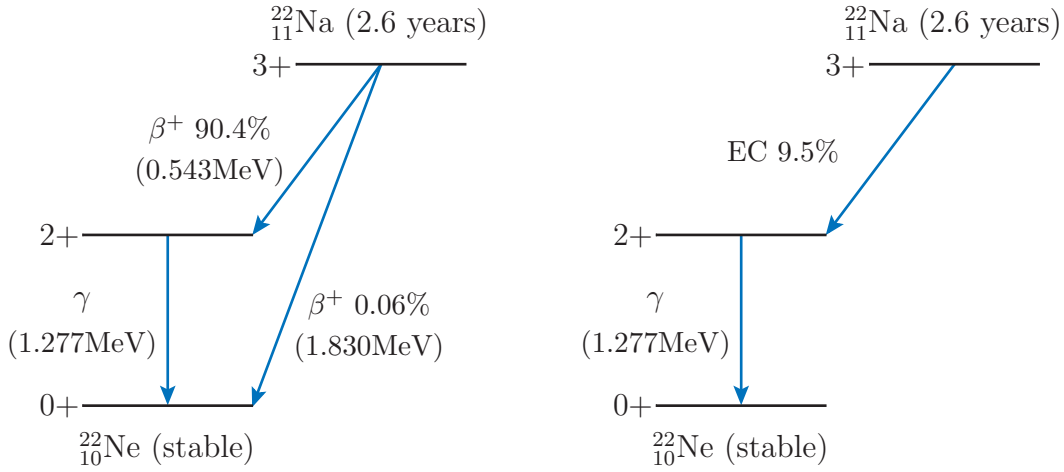

(a) Decay of ^{22}Na through positron emission (b) Decay of ^{22}Na through electron capture

Figure 2.3: ^{22}Na decay to ^{22}Ne through either positron emission ($\simeq 90.4\%$) and electron capture ($\simeq 9.5\%$). The 1.277MeV gamma is released approximately 3.7 picoseconds after the positron is emitted, as the ^{22}Ne decays to the ground state [19].

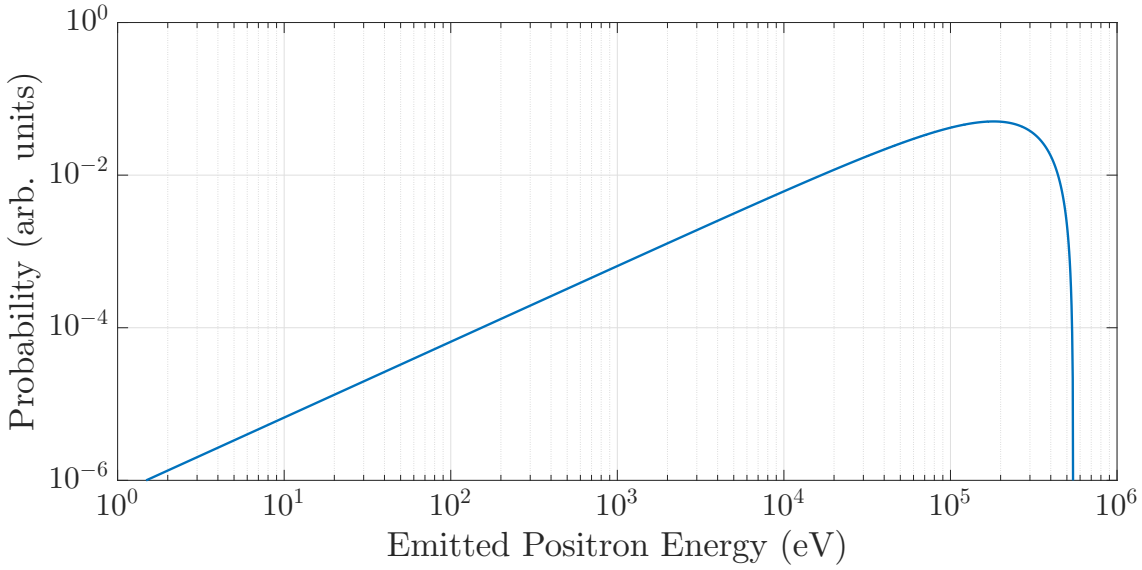

Figure 2.4: Distribution of emitted positron energy from ^{22}Na , calculated using the Fermi equation for beta emission

The difficulty in creating experiments from positron emitters is the energy of the

positrons emitted from the source. A method is required to reduce the positron energy to a range suitable for controlled beam formation and to perform the intended experimental measurements. One way to reduce this energy is through the use of positron moderators. There are various moderators used in positron experiments, including solid neon, nickel, and tungsten, which are discussed in more detail in later in section 2.2.1.

Since we live in a matter dominated universe, a source of positrons is a rarity, and one suitable for experimental purposes is harder still to obtain. Radioactive decay is one source of positrons, and many isotopes emit this as one of their decay channels. Some of these isotopes are naturally occurring, but ones used in laboratories are artificially produced so that they are active enough for the count rates required for experiments. Artificial production often means creating isotopes through enrichment at large scale facilities such as cyclotrons, which can mean per gram antimatter is one of the most expensive items on Earth. Table 2.1 lists some of the more commonly used sources of positrons for experiments around the world.

Isotope	β^+ branching ratio	Energy (MeV)	Half-life
^{22}Na	0.91	0.54	2.6 yr
^{58}Co	0.15	0.47	70.8 d
^{18}F	0.97	0.63	109 min
^{44}Ti (^{44}Sc)	1.0(0.94)	(1.474)	60 yr (4 hr)

Table 2.1: Various atomic isotopes which produce positrons when they decay.

Positron tomography in medicine is a relatively common diagnostic tool. Cobalt-58 is used in medicine to test intestinal absorption of vitamin B-12 and is a tool which can diagnose pernicious anaemia. Fluorine-18 is used in positron emission tomography (PET) to locate cancerous growth in the body. The ^{18}F is used to "label" sugars, which will gather in areas of high metabolic rate, namely cancers or tumours. The 511keV photons from positrons emitted by the ^{18}F decay are picked up by position sensitive detectors, allowing cancer sites to be located within the body [20].

Sodium-22 is a commonly used positron source for atomic and molecular physics experiments, as well as materials science. The emitted positron energy and half-life make this best suited for experiments. This isotope is produced in a cyclotron through the nuclear

reaction:

$$\mathrm{Mg}^{24}(\mathrm{d},\alpha)\mathrm{Na}^{22} \tag{2.2}$$

^{22}Na is expensive to purchase, but with a ~ 2.6 year half-life a high activity quantity enough to form an experimental source of positrons can last an experiment several years.

Titanium-44 has relevance for astrophysics as a potential candidate to account for the abundance of galactic positrons, as titanium-44 is formed in particular supernovae events [21]. It is also used by some groups for experimental physics with antimatter in replacement of ^{22}Na due to lack of access to a production facility [22]. ^{44}Ti itself does not emit positrons, however its daughter nuclei ^{44}Sc does. ^{44}Ti decays at 100% branching ratio to ^{44}Sc through electron capture, which then decays emitting a positron.

In addition to radioactive sources, pair production is used in some facilities as a method to generate positrons. When high energy electrons in a cyclotron, linear accelerator, or products from a nuclear reactor emit bremsstrahlung, pair production of positrons and electrons will occur. The positrons can be used as a source for experiments when properly collected and confined, however they typically have very high energy ($\simeq 30$MeV). Several stages of energy reduction and confinement (beam bunching and chopping) are required to bring the positrons down to low enough energy for experimental use, but source brightness will typically remain very high.

2.2.1 Reducing Positron Energy

Slow and pulsed beam positron experiments make use of the positron sources mentioned in the section above, however the initial energies and energy spread of the positrons are not always suitable for experiments. To reduce the positron energy, interaction with materials are used and these materials are known as "positron moderators". There are two commonly used types of of positron moderator: thin metal films, or rare gas solid (RGS) based.

Metal foil moderators are thin foils of metals, typically tungsten or nickel. The efficiency for these materials as moderators varies between 0.1% to 0.001% depending on the chosen metal [23, 24]. They are relatively easy to build and maintain, but can require in-situ annealing to remain at peak efficiency. Thin metal meshes or grids can out perform

metal films of the same material in moderation efficiency [25].

RGS moderators are harder to build but can provide higher efficiency. Neon is often used, but argon and krypton can also be used. Neon has a lower freezing point than argon, but has the highest efficiency spread of currently known moderators. The ability to create RGS moderators in an experiment requires a cryogenic stage to cool your positron emitter and grow a layer of solid gas close to it. Efficiency is approximately 0.7% for neon RGS moderators and lower for argon and krypton [26]. The emitted positron energy spread from RGS moderators is relatively high at around 1.5eV compared to approximately 0.5eV for tungsten.

The trade off between RGS and metal foil moderators are effectively between efficiency and energy spread. RGS moderators are more efficient with a larger energy spread, and metal foil moderators are less efficient but have a smaller energy spread.

2.3 Positron Interactions with Matter

In this section an overview of the interactions between positrons and solid matter is presented in the context of a beam based PAS experiment [27].

Positrons can interact with solid in all of the various ways that matter particles do, however as detailed previously positrons can also annihilate or form bound state positronium.

From the incoming positron beam, the majority of positrons will be implanted within the material, but a small fraction can be reflected from the surface **(1)**.

The implanted positron will interact with the material in ways which cause the positron to lose energy, enabling other processes to occur. The positron loses energy through interactions with the the constituent electrons and nuclei, for example ionisation, electronic excitation, and nuclear scattering. These energy loss processes occur in the same manner as ion implantation in general, and occur until the positron reaches the same temperature as the material, $\simeq 3/2k_bT$. The distance implanted positrons reach within a material is important for PAS and explored in detail in section 2.3.1.

The processes by which implanted positrons scatter is dominated by Coulomb interactions. For this reason it is convenient to think of materials in terms of charge density. Vacancy or defect sites will be regions of different effective charge than the bulk, which

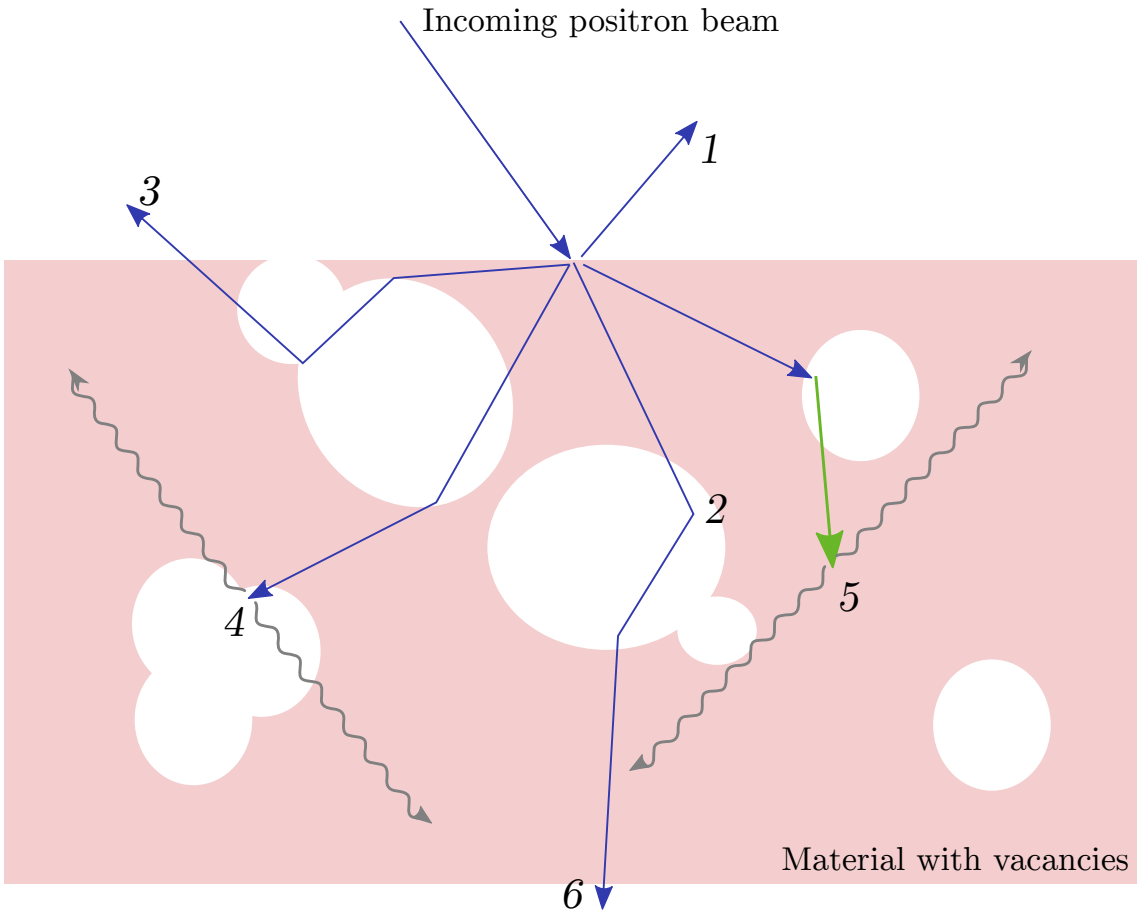

Figure 2.5: Cartoon of the interactions of positrons from an incoming beam source. Numbers reference processes detailed in the text.

become attractive or repulsive to the implanted positrons. Positron diffusion **(2)** is influenced by the regions of effective charge and if defects are negatively charged (or neutral) positrons will preferentially locate there. In a material with a large defect network, a positron can move through the network and travel much larger distances than would be possible without the presence of large electron-free volumes. In some cases, positrons that enter a material like this can diffuse out of the material again, annihilating elsewhere **(3)**. Knowing the diffusion length of positrons in a material being studied can aid in the interpretation of results for PAS experiments.

Thermalised positrons that diffuse through the material can annihilate **(4)**, form positronium **(5)**, or escape the material through transmission **(6)**.

In annihilation **(4)** the positron will annihilate with an electron from one of the atoms that make up the solid. Generally this will be a valence electron - one furthest from the nucleus, but occasionally the positron will annihilate with a core-shell electron with

significant momentum. Annihilation with electrons in the bulk (rather than at a defect site) will give the intrinsic lifetime of a material - how long the positron exists for within the material before annihilating.

The formation of positronium **(5)** is possible in some materials, as long as the positron-electron pair's energy is above the 6.8eV binding energy. Following formation, the Ps can further interact with the material before annihilation occurs.

2.3.1 Implantation of Positrons into Solid Materials

When positrons are implanted into a material, the depth z to which the positrons will penetrate is dependent on the energy, E, of the incident positron and is modified by the density, ρ, of the target. The formulation of the distribution of implanted positrons is based on work by Makhov in 1961 on electron implantation [28, 29].

The implantation profile is given by:

$$P(z,E) = \frac{mz^{m-1}}{z_0^m} \exp\left[-\left(\frac{z}{z_0}\right)^m\right] \tag{2.3}$$

$$z_0 = \frac{AE^r}{\rho\Gamma\left(1+\frac{1}{m}\right)} \tag{2.4}$$

The parameters A, m, and r are empirically determined, and the parameter values of $A = 4.0\mu\text{gcm}^{-2}\text{keV}^{-r}$, $m = 2$, $r = 1.6$ are widely used based on the work of Vehanen *et al.* [30].

The average distance an implanted positron travels through the material is given by $\bar{z}$, the mean implantation depth. The calculation of $\bar{z}$ uses the same constants as above:

$$\bar{z} = \frac{AE^r}{\rho} \tag{2.5}$$

Theoretical work through Monte-Carlo simulation was performed by Valkealahti and Nieminen to corroborate the work by Makhov resulted in the same profile and experimental constants [31,32], however further simulation work was carried out by Ghosh showing that the parameters for the profile vary with material [33].

Figure 2.6 shows how the Makhov distribution changes with incident positron energy

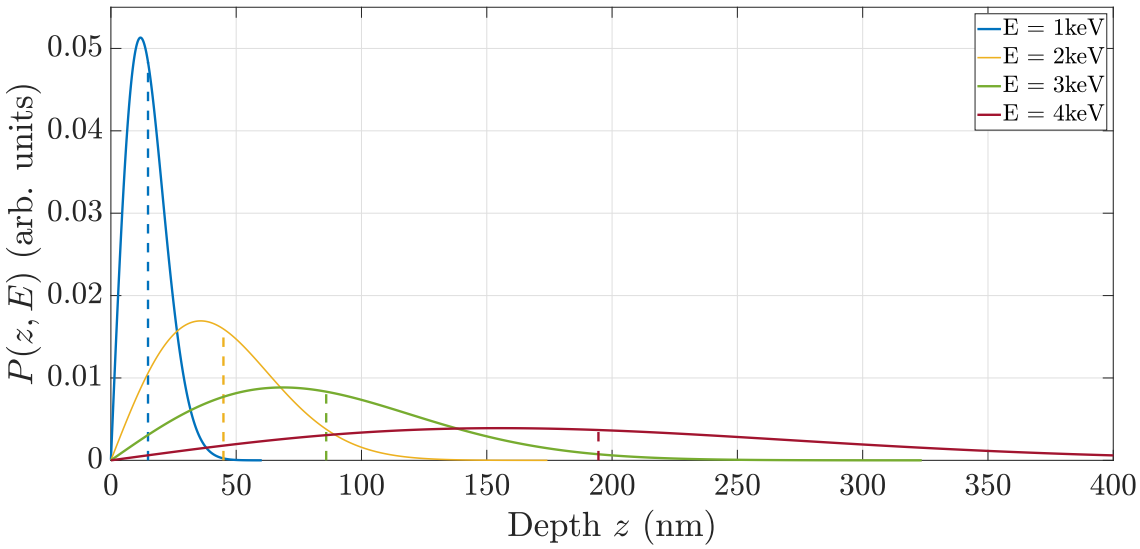

Figure 2.6: Makhov implantation profiles of various energy for aluminium ($\rho = 2.70\text{g/cm}^3$). The mean implantation depth $\bar{z}$ is shown by the dashed line of the same colour for each energy plot.

for the same material sample, in this case aluminium. What is important to note is that the distribution "smears out" as energy increases. The depth at which positrons are implanted to doesn't stay as tightly bunched at 2keV as for 1keV, and at 4keV the positrons are sampling a range of depths in the aluminium sample over more than 400nm. This can be a challenge for positron annihilation techniques as positrons implanted at higher energies will also annihilate at the preceding depths in the sample. The mean implantation depth is larger, but the relative percentage of positrons annihilating there decreases, illustrated clearly with the values of $\bar{z}$ shown on figure 2.6.

2.4 Positron Annihilation Lifetime Spectroscopy

Positron annihilation lifetime spectroscopy (PALS) is used to study the defect structure (namely open volume defects) of materials, and the technique has been used and refined for many years [34,35]. The lifetime of a positron is measured from a known starting time, until a characteristic 511keV photon from positron-electron annihilation is detected, repeated over many measurements. Analysis of these lifetimes gives insight into the physical properties exhibited by the material and in some cases the defect size can related to the positron lifetime, for instance using the Tau-Eldrup model [36–41].

Different features that can be present in a PALS spectrum are the intrinsic positron life-

time within the material, ortho- and para- positronium characteristic lifetimes if positronium formation is possible within the the material, and a number of further lifetimes which come from defects. The lifetimes from defects inside a material can range from specific lifetimes, for example the di-vacancy in silicon has a positron lifetime of 320ps [42, 43], or a range of lifetimes for materials with a distribution of different sized defects. Comparison of the presence of these lifetime characteristics in a material can reveal information on the internal structure of the material sample.

Typically there are two types of PALS measurement, bulk PALS [44] and pulsed beam PALS [45]. The two measurements differ in experimental set-up and the information gained from the results, however the *form* of the results is the same. Bulk PALS systems are much simpler than pulsed beam PALS and use as-emitted positrons from radioactive decay. The positrons are therefore high energy with a large distribution of energies, meaning that they will annihilate throughout the entire target and the bulk - hence the name, "bulk PALS". Pulsed beam PALS systems control the implantation energy of the positrons and therefore probe only a selected region of the target, using a pulse of positrons which gives a specific start point for the lifetime measurement.

2.4.1 PALS Data

A PALS spectrum is a histogram of positron lifetimes as observed from positrons implanted into a particular material of interest. A typical histogram often contains $1 - 3.5 \times 10^6$ counts. The spectrum typically shows a Gaussian resolution function convoluted with a series of exponential decays for each present feature as mentioned previously.

The Gaussian resolution function is formed by the resolution in the detection system in the experiment convoluted with the temporal width of the positron pulse.

To extract information from a PALS spectra, curve fitting programs are used to fit the convolution of the resolution function and the positron lifetimes. The fitted exponential decays give the lifetimes of positrons inside the material. The intensity is the amplitude of the exponential decay. The generalised form of this is:

$$I_0 \mathrm{e}^{-t^2/2\sigma^2} * \left(I_1 \mathrm{e}^{-\tau_1 t} + I_2 \mathrm{e}^{-\tau_2 t} + ...I_n \mathrm{e}^{-\tau_n t}\right) \tag{2.6}$$

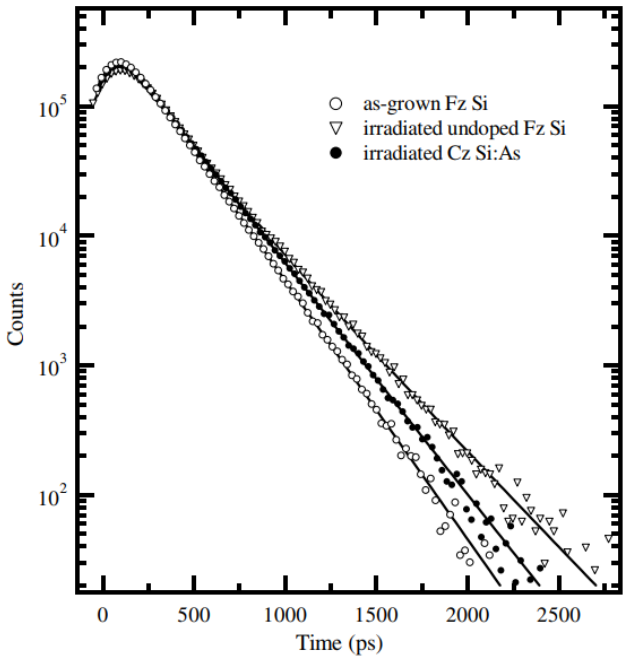

Figure 2.7: An example PALS spectra, reproduced from the work by Saarinen and Ranki [46]. Here the PALS spectra of float-zone (Fz) refined silicon and Czochralski (Cz) grown silicon are compared after irradiation with 2MeV electrons. From the original work: "Positrons annihilate in the as-grown sample with a single lifetime of 220 ps corresponding to delocalized positrons in the lattice. In the irradiated samples the experiments reveal vacancies with positron lifetimes of 250 ps (V–As pair in Cz Si:As sample doped with [As] = 10^{20} cm^{-3}) and 300 ps (divacancy in undoped FZ Si sample)"

where $*$ denotes the convolution. The coefficients are determined by fitting the spectrum, where $I_0 \mathrm{e}^{-t^2/2\sigma^2}$ is the instrument function, and the $I_i \mathrm{e}^{-\tau_i t}$ terms are the lifetimes (τ_i) and corresponding intensities (λ_i). An example of this data and fitting process is shown in figure 2.7.

The intensity correlates to the relative presence of that lifetime, and in the case of lifetimes arising from vacancies, correlates to the density of vacancies with that particular positron lifetime. It can be thought of as the relative concentration of defects, although a direct relationship between I and defect concentration is difficult to quantify.

2.4.2 Bulk PALS Systems

In a bulk PALS experiment, the material sample to be analysed is sandwiched between ^{22}Na deposited on Kapton foil, and measurements are made using fast scintillation detectors configured to collect the start and stop signals. The 'start' signal for the positron lifetime is given by the 1.27keV photon which accompanies the birth of the positron from

the radioactive disintegration of a ^{22}Na atom into ^{22}Ne. The positron is emitted 3.7 picoseconds before the 1.27keV photon, see figure 2.3. These systems have good resolution and can usually determine the intrinsic positron lifetimes of materials, even for metals, which can be 100ps or less.

Since the positrons emitted in the decay of ^{22}Na have a large energy distribution and are also of high energy, positrons that annihilate in the material will do so throughout the whole sample without the possibility for singling out a particular depth or region of interest within the sample. Additionally, since the ^{22}Na is deposited in some foil or other layer outside of the sample, the material of the foil itself will interact in some way with the emitted positrons, as radioactive decay is isotropic in emission direction. Positrons may annihilate within the foil that they are prepared on, which can add complications to analysing to the collected PALS spectra. The method also requires a lot of preparation since a new radioactive source needs to be deposited on a foil for each sample measured.

2.4.3 Pulsed Beam PALS

Pulsed beam PALS forms positrons from a source into a controllable beam, and implants the positrons into the target material in pulses at a well defined energy. The pulsing of the beam gives the start signal for the lifetime measurement, and the annihilation photon is again used as the stop signal. The pulsed beam system allows for depth profiling targets with PALS since the energy of the positron pulse is defined by the experimental apparatus. The simple model for the implantation depth of the positron beam is discussed in section 2.3.1.

The implantation distribution of the positrons is determined by the interaction energy and so the energy of the positron pulse can be tailored such that annihilating positrons sample regions of interest within the material being investigated. Preparation of samples by irradiation can be systematically investigated from surface through to bulk.

Difficulties in these systems typically occur in the timing resolution of the experiment, as this is determined by the temporal pulse width of the positrons. Trapping, bunching, and accelerating positrons to form a pulsed beam is difficult task and many solutions have been developed for this [47–50].

2.4.4 Resolution of Lifetimes

The ability to resolve different lifetimes in a PALS spectrum depends on the full-width at half-maximum (FWHM) of the resolution function in the experiment, as well as the number of counts in the spectra. It is important to note that the FWHM does not limit the experiment to only resolving lifetimes the same as or longer than the temporal width of the FWHM. Collecting more data can allow you to resolve lifetimes shorter than the inherent pulse width. However, in Poissonian statistics, the uncertainty scales as $\sqrt{n}$ (the number of counts in the spectra), so diminishing returns will limit the practical benefit to collecting more data for higher resolution. The impact of resolution and spectra total counts was investigated by Yamawaki *et al.* [51].

2.4.5 The Tao-Eldrup Model

The relationship between positron lifetime and vacancy size was determined intially in a semi-empirical model, the Tao-Eldrup model, and later reconciled in a more theoretical framework relating to the quantum-mechanical size of the Ps wavefunction and in-material cavity where it annihilates [38, 39]. This work has more recently been reconsidered and a fully quantum mechanical model was developed which agreed extremely well with the previous Tao-Eldrup model [34, 52]. Figure 2.8 illustrates the relationship between pore dimension and positron lifetime for spherical or rectangular pores.

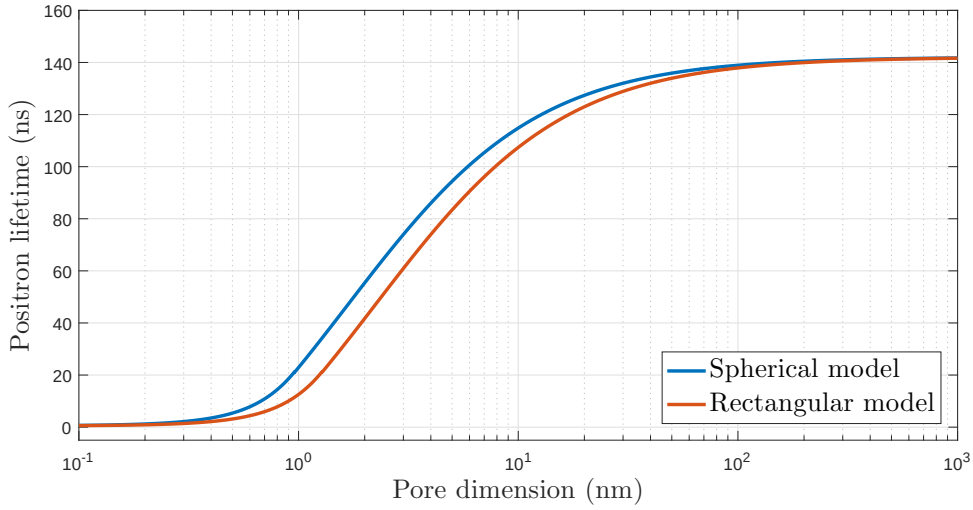

Figure 2.8: TheTao-Eldrup model, reproduced by the work by Wada and Hyodo in [41]. Here the comparison between rectangular and spherical pores made, and shows the difference in the two assumptions.

It can be seen that the Tao-Eldrup model is not applicable to all systems with positron lifetimes, and is un-physical for positron lifetimes below 400ps. For this reason it is reliably used to relate positron lifetimes in molecular or organic materials, but not metallic materials. The Tao-Eldrup model asymptotes to a lifetime of $\simeq$142ns, which is the lifetime of ortho-positronium in vacuum.

2.5 Doppler Broadening of Annihilation Radiation

Doppler broadening of annihilation radiation (DBAR) is a positron technique which obtains information about the internal structure of a material by measuring the momentum distribution of annihilation photons. DBAR is a comparative technique and the results are unique to the particulars of the experimental apparatus used, however it is a powerful technique in determining the differences in internal structure of samples through the changes in fractions of positrons that annihilate with electrons of different momentum.

DBAR can extract information on vacancies in materials and the chemical nature of defects, and characterise changes in these properties as a function of depth through S and W parameters respectively [53–55].

2.5.1 Doppler Broadening in Positron Spectroscopy

Generally speaking, when positron-electron annihilation takes place, the positron has thermalised within a material ($E_{e^+} \simeq 3/2k_bT$, 40 milli-electron Volts at room temperature) and hence has a low momentum. The other partner in the annihilation, the electron, does not necessarily have a low momentum. Electrons in the outer shells or valence bands of a material have low momentum, but the electrons which are much closer to the nucleus can have very large momentum. In a case where a positron annihilates with a core shell electron, the annihilation quanta undergo large Doppler shift due to the high momentum of the core electron. Typically the Doppler broadening from positron annihilation with valence shell electrons is $\simeq$ 1keV, whereas positron annihilation with core shell electrons can result in broadening of $\geq$ 4keV.

In the frame of reference in which the centre of mass is at rest, the annihilation photons are emitted $\simeq 180^\circ$ from each other, i.e. back-to-back. However in the laboratory frame,

the centre of mass is in motion from the momentum of the system, thus producing a Doppler shift in the energy of the emitted gammas. The Doppler shift is give by:

$$\Delta E = 2m_e c v_{cm} \cos\phi \tag{2.7}$$

where ϕ is the angle between the motion of the centre of mass and one of the emitted photons, and v_{cm} is the speed of the centre of mass.

By analysing the annihilation photon energy from a particular target of interest, the distribution of annihilation photon energies can be found. This allows a relative measurement to be made, comparing the distributions of a damaged material with a pristine or reference sample, which then gives information about the internal structure of the damaged sample. Initial reporting of this phenomena was by DeBenetti in 1949 [56, 57].

In an undamaged material, the distribution of photon energies is representative of the physical structure of the material. In the case of a single crystal metal, the probability of positron annihilation with valence or core electrons is the same throughout the whole material sample. However, through damage a material may contain voids, dislocations, or other defect types, and thus areas of effective negative charge are introduced. Positrons implanted into a material like this will preferentially locate to these areas, and thus have a higher probability of annihilating with a valence electron due to the lack of a neighbouring atomic nuclei. This changes the annihilation photon energy distribution, and this can be seen when comparing the damaged and pristine distributions [58, 59].

In the comparison of positron annihilation distributions, two measurements are made: the shape (S) parameter, and the wing (W) parameter measurements. These two parameters are comparisons of the area under a select region of the curve, in ratio to the total area under the curve. The S and W parameter measurements each give information on different aspects of the material being investigated.

2.5.2 The S Parameter Measurement

The S parameter measurement is the ratio of the central peak in the spectra to the whole area under the curve, as shown in figure 2.9. The measurement region of the S parameter is taken from the centre of the 511 peak to up to a few keV outwards. In figure 2.9, the example region shown is 511 ± 0.8keV.

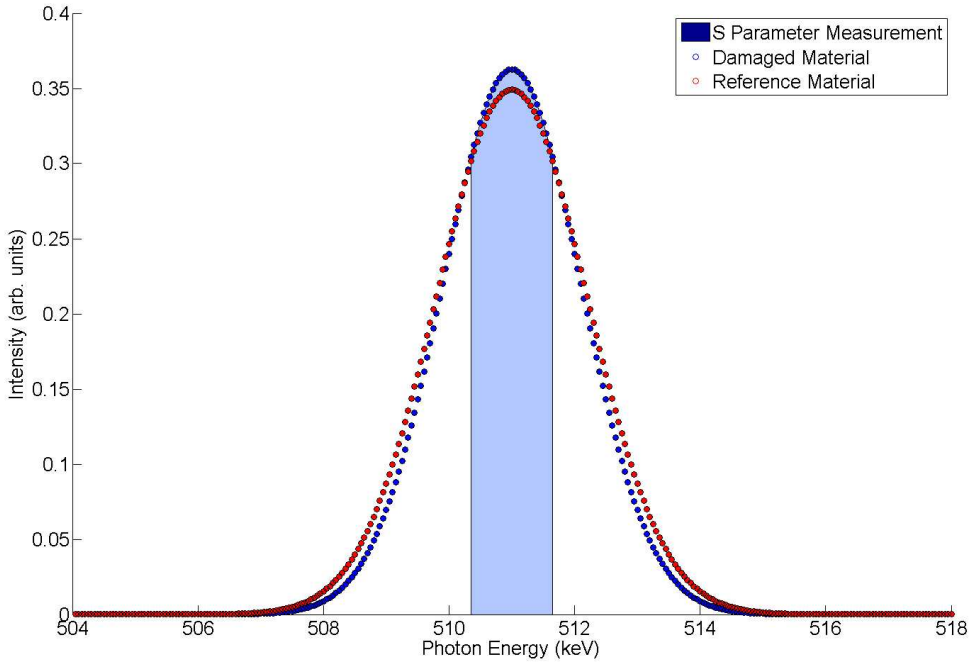

Figure 2.9: S parameter measurement region

An increase in S parameter signals an increase in the number of positrons annihilating with low momentum electrons, and therefore an increase in the quantity of voids present in the material. In a damaged sample there will be more 511keV photons from annihilation from valence electrons in defect sites have the highest probability for annihilation.

$$S = \frac{\int_{511-s}^{511+s} n \, \mathrm{d}E}{\int_{511-b}^{511+b} n \, \mathrm{d}E} = \frac{N_s}{N_b} \tag{2.8}$$

For the work presented in this thesis in chapter 7 and 8, s is 1.2keV and defines the central peak region, and b is 10keV, and defines the "whole area" of the peak.

The calculation of the uncertainty in the S parameter is based on Gaussian counting statistics and given by:

$$\sigma_S = \frac{1}{\sqrt{N_b}} \sqrt{S(S+1)} \tag{2.9}$$

Depth profiling a sample with positrons and plotting the S parameter as a function of depths is often a good way to find interesting features in a damaged sample, as the S parameter can vary dramatically between areas of high and low damage.

2.5.3 The W Parameter Measurement

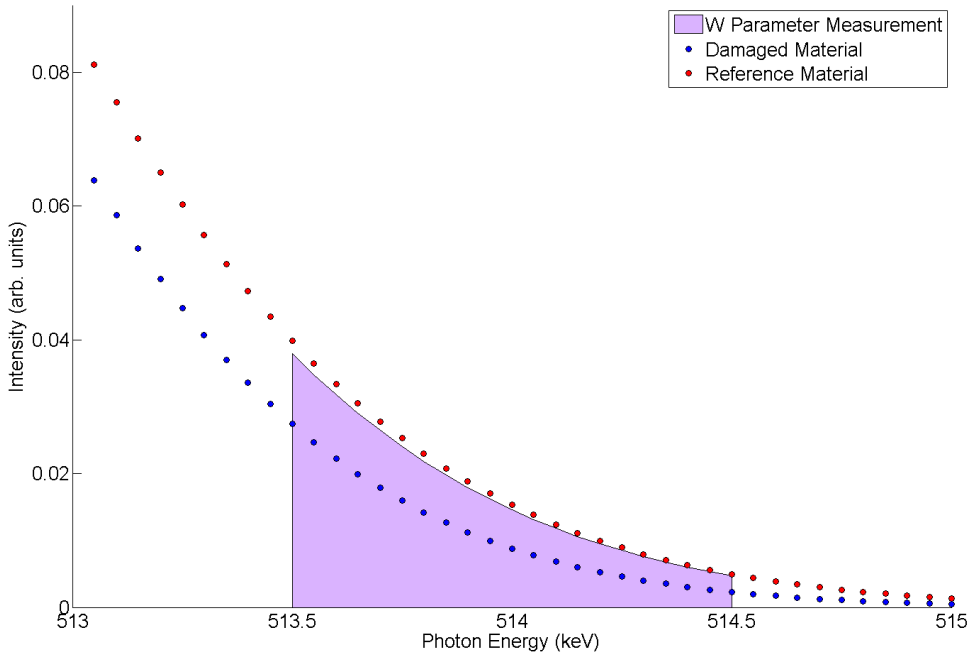

Figure 2.10: W parameter measurement region

The W parameter measurement is the ratio of the high energy component of the spectra to the whole area under the curve, as shown in figure 2.10.

The W parameter measurement is generally taken in the region of 514 keV, so that it does not interfere with the S Parameter measurement. The ratio is made using the same limits for the whole peak area as the S parameter, which in the case of the work presented in this thesis is 511 ± 10keV. The W parameter gives information about the broadening due to high momentum electrons present in the material, which is determined by the elemental species present.

Measurement of the high momentum region is harder to make than the S parameter since the counts are fewer in this region than the centre of the 511keV photopeak and can be swamped by background. This is particularly noticeable on the lower energy side of the spectra, which has a higher background due to experimental effects (incomplete charge collection, natural laboratory background radiation levels) and 3-photon annihilation events from positrons.

The 3-photon background from positron annihilation is the dominating source of back-

ground on the low energy side of the 511keV photopeak, but can be almost entirely removed through two detector coincidence measurements of two-photons annihilation events. Without the 3-photon annihilation background both sides of the photopeak can be used to make W parameter measurements [60].

Recently, mathematical processing of single detector DBAR measurements have been developed to allow similar quality to coincidence experimental results [61].

To define the double sided W parameter measurement mathematically:

$$W = \frac{\left(\int_{514+w_r}^{514+w_l} n \, \mathrm{d}E + \int_{508-w_l}^{508-w_r} n \, \mathrm{d}E \right)}{\int_{511-b}^{511+b} n \, \mathrm{d}E} = \frac{N_w}{N_b} \tag{2.10}$$

The two integrals that make up the numerator of this ratio are the low energy (left) and high energy (right) regions of the 511keV photopeak. The work presented in this thesis makes use of a single detector system, so the W parameter measurements are defined using the high energy side of the 511keV photopeak only, and the integrated region was from 514 ± 1keV.

Since the W parameter is calculated in the same way as the S parameter, with similar form but with different limits for integration, the expression for the uncertainty is the similar:

$$\sigma_W = \frac{1}{\sqrt{N_b}} \sqrt{W(W+1)} \tag{2.11}$$

This applies equally for single sided or double sided W parameter, as the uncertainty in the numerator of equation 2.10 is still remains the square root of the sum of the counts.

2.5.4 Information From DBAR Measurements

Since DBAR makes relative measurements, it lends itself best to series measurements across a sample set, which vary in preparation in a methodical manner. Each measured sample will have S and W parameter measurements made in comparison to the same pristine reference material.

Plotting the S and W parameter as a function of depth, preparation temperature, ion implantation dose, or other controllable parameter will then provide information on the

evolution of the sample under these conditions.

Looking for significant changes in the S and W parameter trends indicates regions at which the internal structure of a material is significantly changing. To fully characterise the material, additional experimental measurements using absolute analysis techniques (as opposed to relative analysis techniques, such as S and W parameter measurements) should be carried out at these critical regions.

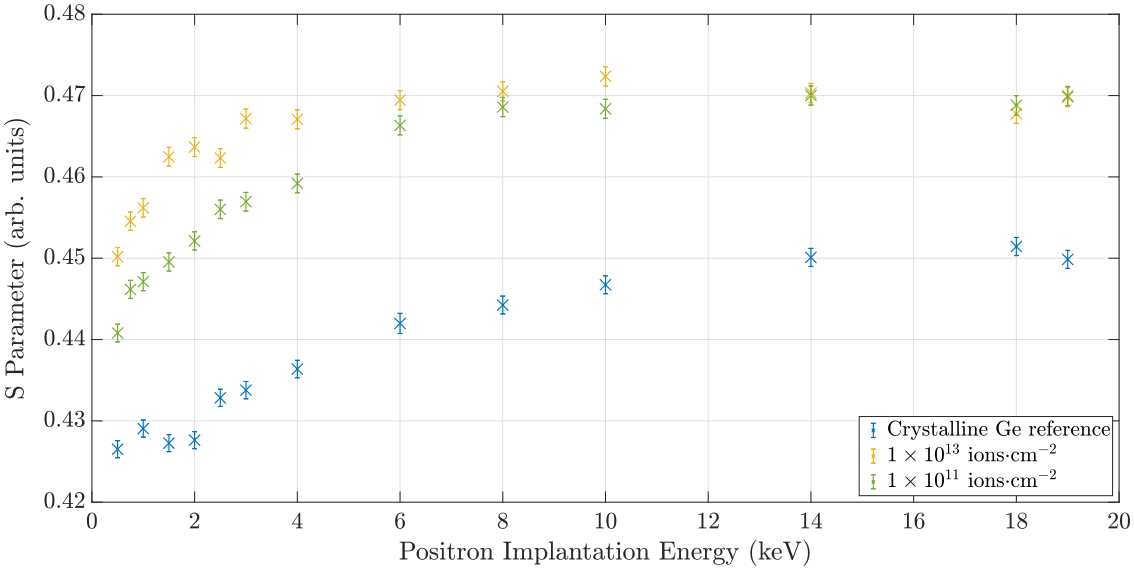

Figure 2.11: S parameter as a function of positron implantation energy for as-grown crystalline germanium implanted with 1.5MeV germanium at 1×10^{11} and 1×10^{13} ions·cm^{-2}. These measurements were made using the DBAR experiment developed as part of this work.

Figure 2.11 shows an example damage experiment which examines the effects of implanting as-grown crystalline germanium with germanium ions. The S parameter is presented as a function of positron implantation energy, which directly relates to mean positron implantation depth. In this example, the S parameter is significantly larger for the damaged samples of germanium substrate in comparison to the reference sample. Additionally, the S parameter is larger for the sample implanted with a higher fluence of germanium (1×10^{13} ions·cm^{-2}) as compared to the sample implanted with the lower fluence (1×10^{11} ions·cm^{-2}). The graph shows that the implantation has changed the base material in a significant way, and the number of positrons annihilating with valence electrons increases in the implanted samples.

2.6 Other Positron Techniques

There are other techniques to extract information from positron annihilation, in addition to PALS and DBAR. Some examples are briefly described in the following sections.

2.6.1 Reflection High-Energy Positron Diffraction

Reflection high-energy positron diffraction (RHEPD) or total reflection high-energy positron diffraction (TRHEPD) examines crystalline material surfaces, using glancing angles of reflection, or total reflection. Analysis of the diffraction patters gives information on the surface formation, crystallographic orientation, and layering. The technique gives more accurate results than similar techniques using electrons due to the differences between positrons and electrons interacting with the crystal structure and diffraction laws as well as very low levels of experimental background counts. RHEPD requires high intensity positron beams to be effective and so is performed at bright positron sources, for example KEK in Japan [62].

2.6.2 Angular Correlation of Annihilation Radiation

ACAR examines the deviation from co-linearity in the two-photon product in positron-electron annihilation [56, 57]. This examines the momentum of the annihilating pair through position rather than direct measurement of photon energy. For this technique to work properly it must be a coincidence measurement as the angle between the annihilation photons must be determined relative to one another, requiring both photons to be properly detected. The experimental set-up for an ACAR measurement tends to be a large apparatus as increasing the distance between the detector and the sample increases the angular resolution of the measurement. Ensuring the incident positron beam has a small spot size at the target sample reduces the experimental uncertainty by reducing size of the positron-electron annihilation region [63].

2.6.3 Age-Momentum Correlation

Age-MOmentum Correlation (AMOC) measurements combine PALS and DBAR techniques which can reveal additional information by examining where the positron annihilates in relation to its lifetime. An AMOC measurement requires three components: a

start signal, a fast stop signal to obtain an accurate lifetime measurement, and an energy measurement of the annihilation products for the annihilation photon momentum. An AMOC measurement reveals patterns of movement of implanted positrons and positron transport in the material (e.g. positrons could travel towards the bulk or become trapped in defects) and gives information about the effective charge of present defects [64].

Chapter 3

Positron Annihilation Lifetime Spectroscopy at ANU

The positron annihilation lifetime spectroscopy (PALS) experiment has been established for many years at the Australian National University [47], and like most physics experiments it is a constantly evolving and improving apparatus with each new researcher optimising and refining at least one facet of the experiment.

This chapter explores in detail the PALS experiment at ANU, including the experimental apparatus, typical operating parameters, and physical systems behind the inner workings of the beamline, as well as data collection and analysis.

3.1 Overview of the PALS Experiment

The positron annihilation lifetime spectroscopy experiment on the positron materials beam line at the Australian National University is a pulsed beam experiment utilising a buffer gas trap. The positron pulse is formed in two stages by a neon moderated radioactive ^{22}Na source for the primary beam, with further cooling and bunching performed in a Surko type buffer gas trap. The release of positrons from the trap forms the start signal for the PALS experiment, and the annihilation photons are collected at the sample stage to signal the end of the positron lifetime. The interaction energy of the experiment is set by biasing the sample stage with variable voltage level allowing for depth profiling of target materials.

The experiment specialises in measuring the relative changes in material samples with incrementally adjusted material preparation. To do this, a bespoke analysis package has been written which allows use of an arbitrary temporal pulse shape distribution. The arbitrary instrument function means that the use of a carefully chosen PALS spectra of

a reference sample as an instrument function removes any intrinsic lifetimes, only giving results of positron lifetimes that are not present in the reference spectra (thus due to the material preparation). This relative measurement technique not only mitigates experimental uncertainties related to positron implantation (as mentioned in section 2.3.1), but also mitigates some of the experimental complications with this buffer gas trap implementation of pulsed beam PALS.

3.2 Experimental Set-up

A full and detailed description of the experimental apparatus is described in reference [47], however key details will be covered in this section.

The PALS beamline is a linear beam experiment composed of 3 main stages: the source stage, trap stage, and sample stage. These main sections are contained within a common vacuum system and each stage can be isolated by gate valves. The entire experiment is kept under vacuum at an operating pressure of approximately 1×10^{-8} torr by turbomolecular pumps backed by rotary roughing pumps.

The vacuum system structure is surrounded by solenoids which provide a strong magnetic field for radial confinement of the positron beam, with magnetic field strengths of at 530 Gauss at the trap stage. This strong magnetic field is important for confinement of the positrons in the radial direction and allows the electrostatic confinement and cooling of the positrons to take place.

3.2.1 Source Stage and Primary Beam

The source stage of the experiment safely confines a radioactive ^{22}Na source so that it is suitable for laboratory use, and forms the emitted positrons from the radioactive decay into the primary beam. For the experiments presented in this thesis, the source strength was approximately 11 mCi.

The radioactive decay of ^{22}Na (as described in Figure 2.3) not only produces useful positrons, but also high energy gamma rays which are potentially harmful to the human body. In order to make the source safe enough to use within a laboratory setting without restrictive use of personal protective equipment, the ^{22}Na source is stored inside an elkonite block within the vaccuum system, which is itself store in a shielding tank filled with lead

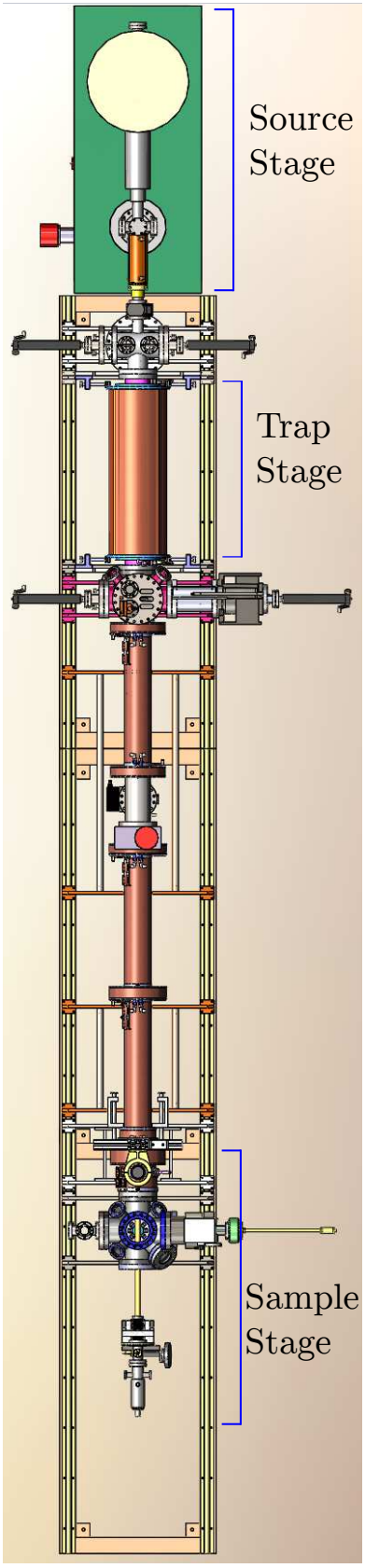

Figure 3.1: Schematic of the entire positron materials beamline from above.

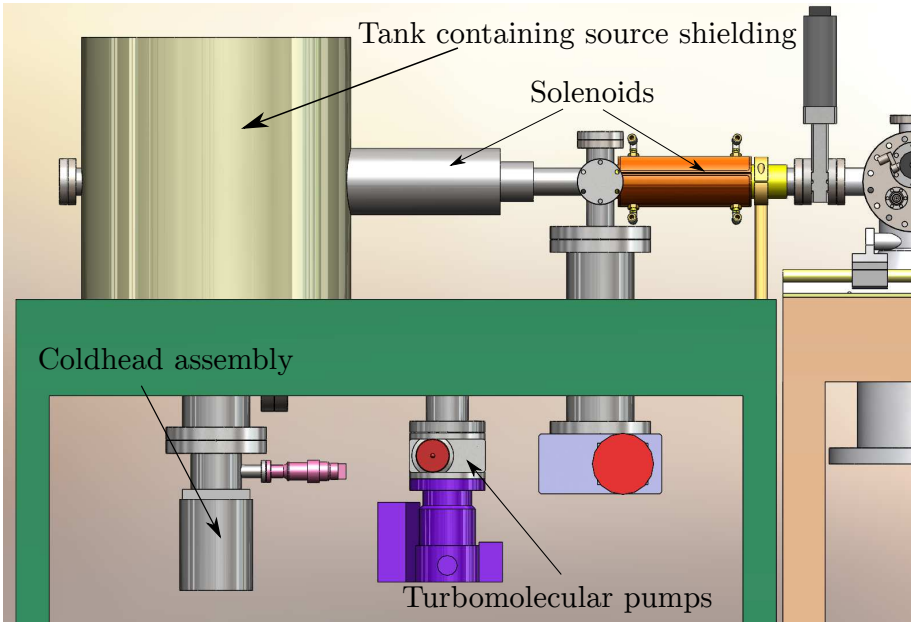

Figure 3.2: Schematic of source stage

shot. The shielding is sufficient to reduce the emitted radiation to a near background level and allow for safe work within the laboratory around the experiment.

Since radioactive decay products are emitted isotropically, Helmholtz coils placed within the lead shielding are used to preferentially confine moderated positrons from the source on the axis of beam formation.

The radio active decay of ^{22}Na produces positrons which have a large energy distribution, up to 546.44keV [19] as shown in figure 2.4. To reduce the positron energy enough to form a beam, a rare gas solid (RGS) moderator of neon is used. The RGS moderator is grown directly in front of the ^{22}Na source on a conical geometry cold finger, pointed in the direction of beam formation and axial with the Helmholtz coils. The temperature of the cold finger and ^{22}Na source is controlled by a helium compressor-expander system, and generally kept between $6 - 8$K. The neon moderator functions in the manner previously described in section 2.2.1.

Low energy positrons leaving the moderator region are confined radially by a strong magnetic field, then proceed through a saddle coil field which vertically steps the positrons upwards and back down again through tungsten cylinders with off-axis central apertures, setting the geometric position of the primary beam. The saddle coil stage is important as it removes line of sight from the sample stage to the source, providing radiation shielding

in the beam formation direction, and additionally moves the primary beam out of the same plane as the source to minimise the impact of any high energy un-moderated positrons that are emitted. Without the saddle coil these high energy positrons will lead to elevated background detection events in the experiment.

To monitor the quality of the primary beam, a simple CsI detector is set up to monitor positron annihilation at the gate valve between the source stage and trap stage, which isolates the sample stage from the rest of the beamline. The count rate of positrons annihilating on the closed gate valve gives a representative measure of the primary beam strength. From a source strength of 11mCi, a typical primary beam strength is approximately 2×10^6 counts per second after moderation. The moderator is biased to approximately 30V, which sets the energy of the primary beam. The energy spread of the positrons in the primary beam is 1-2eV, which is determined by the moderating interaction with the RGS neon [26].

Growing moderators

The process of depositing neon onto the cold finger to form a RGS moderator is generally referred to as "growing a moderator", in reference to the incremental layering of neon gas to form a solid thick enough to moderate positrons, and the relatively large amount of time over which this process is carried out.

The generalised procedure for growing a moderator is as follows:

1. Sublimate previous moderator by warming the system, while pumping the chamber.
2. Change temperature to the grow temperature, and allow to stabilise.
3. Stop vacuum pumping on the moderator stage. Neon is emitted from a gas jet directed at the cold cone directly in front of the radioactive source for enough time to grow a sufficiently thick layer of neon on the cold finger.
4. Store the moderator at a suitable temperature.

Growing a good quality moderator is determined by the specifics of the cryogenic stage, and moderator quality can be influenced by many different parameters and even consecutively grown moderators can vary considerably between grows on the same system. This, in part, depends of the cleanliness of the vacuum system, but it will also depend on the input parameters for the grow, such as how long neon is emitted for, and the temperatures at which the cold finger is kept. Contaminants in the vacuum system, such

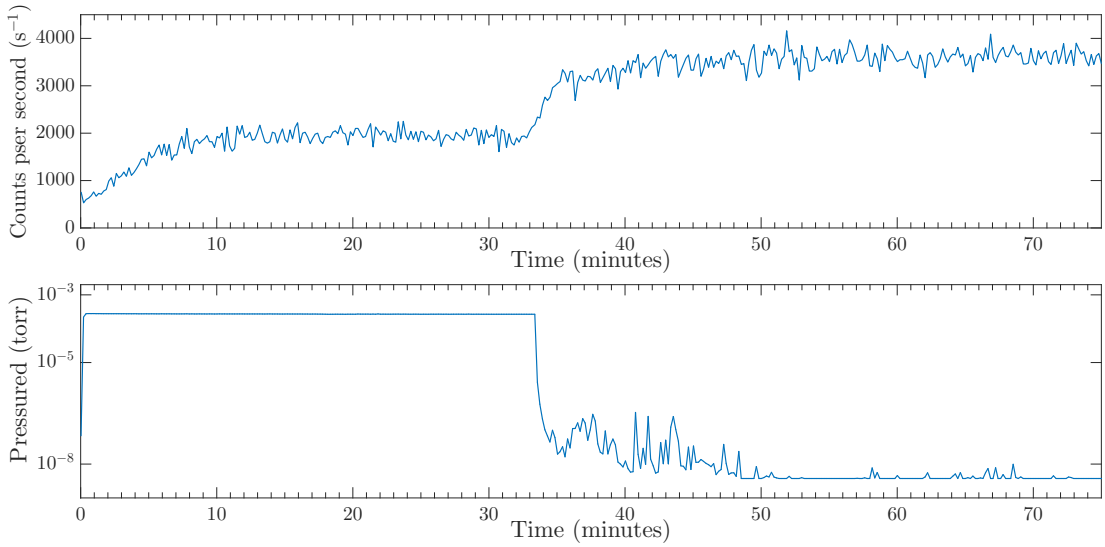

Figure 3.3: Typical grow curve for a solid neon RGS moderator. The particular grow parameters for this curve were a grow temperature of 8K and neon was emitted for 2000 seconds. The counts are measured by the CsI detector which monitors positrons annihilating from the primary beam on the closed gate valve between the sample and trap stages of the experiment.

as N_2 and O_2 from air, can condense and become solidified as part of the moderator during the moderator grow, which will change the interaction with positrons and generally reduce moderation efficiency.

The moderator stage on the materials beam line at the Australian National University can be isolated from the rest of the experiment's vacuum system with a gate valve. During a grow, this gate valve is kept shut to isolate the system, however during operation of the buffer gas trap it is impossible to keep the moderator and trap gases completely separate with any feasible amount of pumping and source-trap separation. For this reason, the trap gases interact with the moderator and typically contribute to much faster decay through surface contamination of the solid neon as well as slow sputtering of neon from the moderator surface by the trap gases. Due to this effect, a typical moderator for the PALS beam will last between 2 and 4 days before needing to be regrown.

Figure 3.3 shows a typical count rate curve during a moderator grow. The positron annihilations per second are measured at the gate valve isolating the moderator stage by a CsI detector. In the curve, from time $t = 0$ seconds, neon is emitted until about time $t = 2000$ seconds ($\simeq 33$ minutes). At that time, the neon flow is stopped and any remaining unfrozen gas is pumped out of the chamber. The count rate increases at this

point as positrons are no longer being lost from interaction with the remaining neon gas, which can be seen through the decreasing pressure, until the gauge reaches its lower limit, when the positron count rate reaches maximum.

3.2.2 Trap Stage

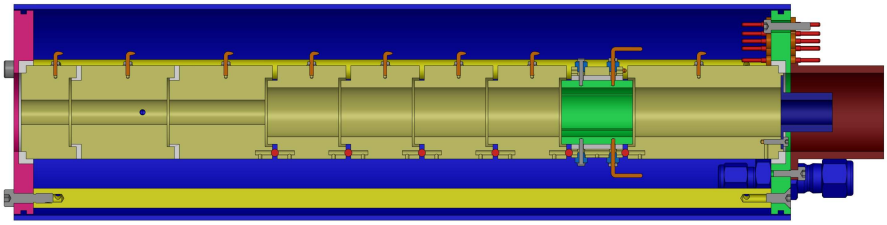

Figure 3.4: Schematic of the Surko buffer gas trap. Positrons enter the trap from the left at electrode 1. N_2 is introduced to the trap through a small hole in electrode 2. Electrodes 7, 8, and 9 form the final potential well.

The trap stage of the positron materials beamline further reduces the energy of positrons from the primary beam and forms the pulsed beam used for PALS measurements. The trap itself traps and thermalises the positrons to the temperature of the buffer gases in the trap, which is room temperature. The trapped thermalised cloud of positrons is used to form the final pulsed beam which has a narrow temporal spread, making it possible to carry out timing experiments.

The positron trap is a based on a Surko trap design, with the original concept developed by the Surko group at the University of California, San Diego [65]. The design combines a strong axial magnetic field and cylindrical electrodes to radially and longitudinally confine positrons. Additionally, the trap is filled with buffer gases to provide an energy loss mechanism for the positrons through collision dynamics.

The trap is constructed of gold-plated oxygen-free copper electrodes and bulkheads, and the individual electrodes are separated by insulators. The entire trap is sealed in a grounded aluminium cylinder to contain the buffer gases, which are nitrogen (N_2) and tetrafluoromethane (CF_4). The buffer gases are added to the trap in two stages to control the interaction with the positrons.

In the first stage, N_2 is directly introduced into the trap through an aperture in the second electrode, shown in figure 3.4 as a black circle. The electrodes in this region form a sealed system using tight fitting PEEK insulators, to minimise the escape of the N_2,

and allowing for a pressure difference between this first and second stages. The pressure difference allows positrons to be efficiently trapped while still giving a reasonable positron lifetime in the second stage where the pressure is lower.

In the second stage, CF_4 is added to the trap in the cavity between the grounded cylinder and the electrodes and is allowed to flow into the internal area through gaps between the electrodes towards the final electrode of the trap. To allow for the gaps which the gas can move through, these electrodes are separated by insulators of ruby balls.

The magnetic fields is kept constant throughout the trapping region at 530 Gauss, however the potentials applied to the electrodes are varied depending on the aim of each particular cycle in the full trapping sequence.

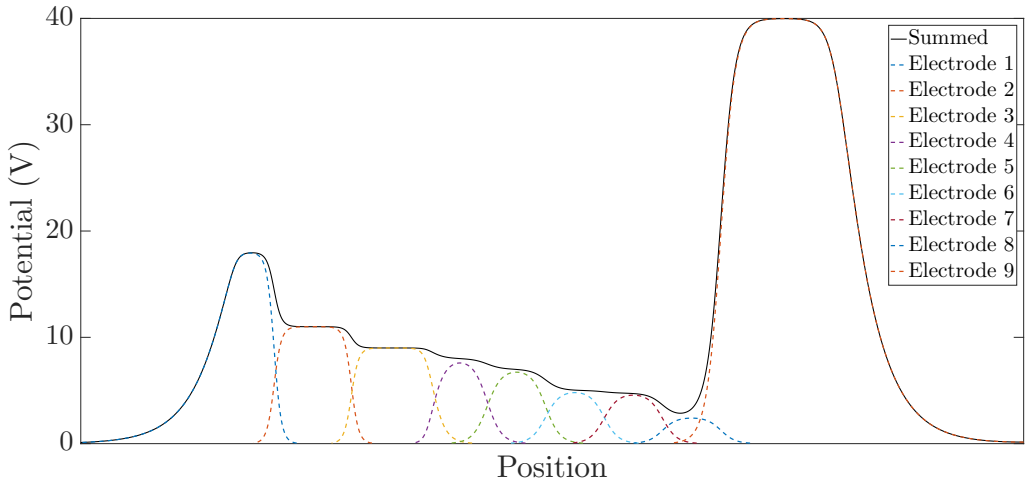

Figure 3.5: The potentials applied to each electrode in the positron trap and the resulting cumulative potential. Positrons enter the trap from the left, with an energy of $\simeq$ 30eV

The trap cycle proceeds in three stages in which different potentials are applied to the electrodes to control the positrons. The potentials applied to each electrode are illustrated in figure 3.6. Each trap stage in the trap cycle performs a different function:

1. **Load Cycle:** Positrons are loaded into the trap from the primary beam, with an energy of 30eV. Positrons lose energy through excitation of a $a^1\Pi$ electronic state of the N_2 and become trapped in the potential well formed by the electrodes.
2. **Cool Cycle:** A blocking potential is applied to electrode 7, confining positrons in a potential well at electrode 8. The positrons lose remaining energy through interaction with CF_4, cooling a final energy of approximately 40meV (from a classical distribution of particle energy $\frac{3}{2}k_bT$, in the laboratory at a temperature of 23°C).

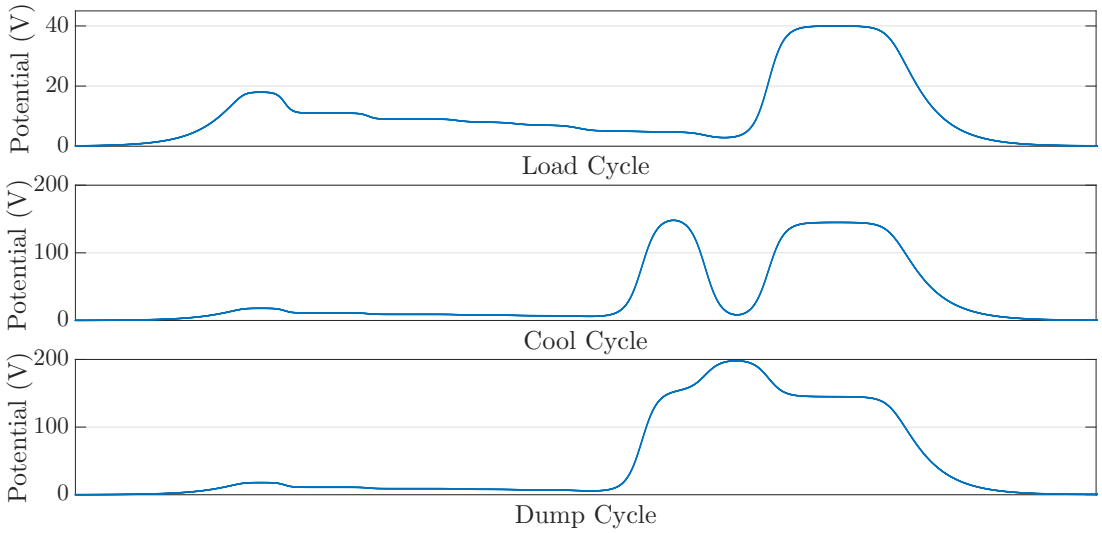

Figure 3.6: Electrode potentials in the load, cool, and dump cycles in the full trap sequence. Positrons enter the trap from the left, with an energy of $\simeq$ 30eV

Separating the two regions of the trap in this manner allows for positrons to be continually trapped in the first stage of the trap while cooling takes place.

3. **Dump Cycle:** Trapped, cooled positrons are ejected from the trap, forming a pulse with a narrow temporal spread by rapidly raising the potential applied to the penultimate electrode (electrode 7). The final electrode sets the transport energy of the pulsed beam.

The potentials applied to each electrode are computer controlled and amplified to the correct levels through high slew rate amplifiers. The potential applied to the penultimate electrode, which ejects the positrons from the trap, requires more finely time resolved control on the applied potential and so is controlled by a separate arbitrary waveform generator (AWG).

The potential applied to the AWG is modulated in such a way that any positrons leaving the trap later in time are accelerated more, such that they catch up to the main pulse [66]. The form of this potential is given by equation 3.1 and the directly applied potential illustrated in figure 3.8. The bunching dump is preceded by a linear rise to a value just below that of the final electrode, after which the bunching potential is applied. The maximum value of the potential is here capped at 200V, the maximum output of the

amplifiers.

$$V = \frac{mL^2}{2e\left(\sqrt{\frac{mL^2}{2eV_0}} - t\right)^2} \tag{3.1}$$

Equation 3.1 is derived through equations of motion for the positron. The potential V is required for the positron of mass m to travel a distance L such that it catches up with positrons with initial energy V_0. The trap-to-sample distance in the experiment is approximately 1.5m, which gives the estimate for the best value for L. Figure 3.7 shows that the best FWHM in the tuning is found at the value $L = 1.5 - 1.75$m.

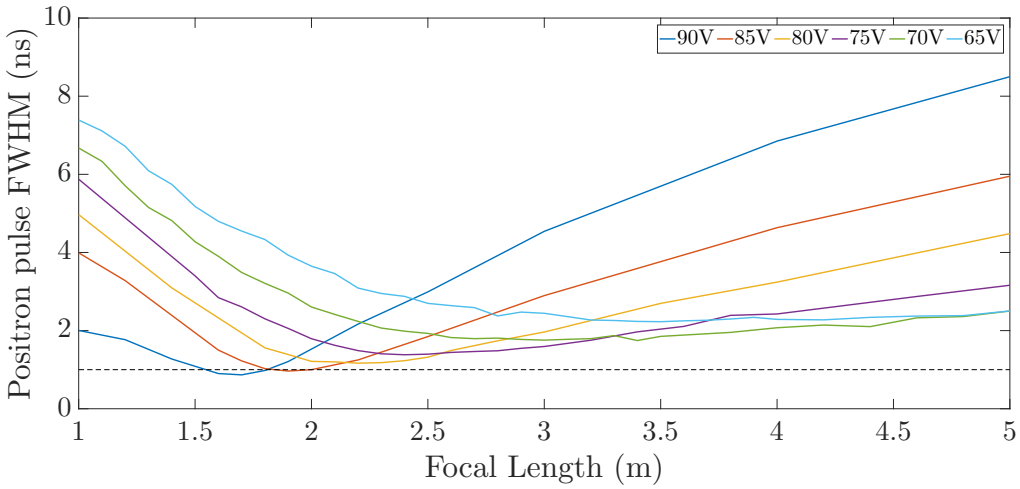

Figure 3.7: Tuning the positron pulse full-width at half-maximum as a function of the focal length (parameter L in equation 3.1) of the time varying potential applied to the well electrode (electrode 8) and the transport energy of the beam set by the potential applied to the final electrode (electrode 9). By tuning this potential alone three parameters are varied: the effective well depth trapping the positrons (at electrode 8); the harmonicity of the trapping well; the beam energy as set by the potential applied to electrode 9.

Figure 3.5 shows the contributions of each electrode in the trap and the applied potentials during the load cycle. Finding the optimal potentials to operate the trap can be calculated however, in practice, empirical tuning is necessary due to factors such as contact potential offsets on the electrode voltages. The tuning is achieved by adjusting the voltages applied to the electrodes of the trap and the buffer gas pressures, which influences the temporal with of the dumped positrons and the count rate of the PALS measurement. An example of tuning the potential of the final electrode against the positron pulse full-width at half-maximum is shown in figure 3.7, which illustrates the empirical process closing in on the optimal parameters to operate the trap.

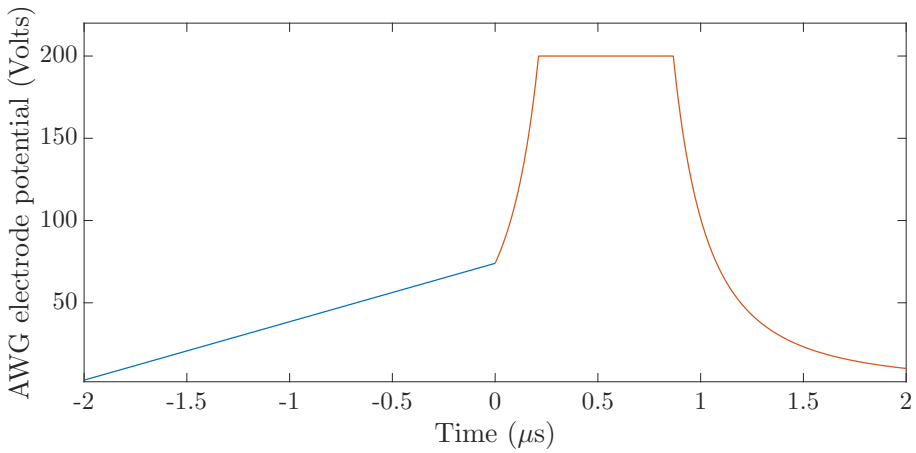

Figure 3.8: The time varying potential applied to the electrode 8. The linear ramp is show in blue, and the time varying potential in orange. For this example, the final electrode is set at 75V, and the potential rises to 74V before applying the time varying potential.

The gas pressures are also tuned empirically, as measuring the pressure directly in the trap is not possible with this experimental design. Gas pressures for both N_2 and CF_4 are tuned through the pressure measured at the exit of ballast tanks, before the gas enters the capillaries leading to the trap. In general the amount of gas required scales with the repetition rate of the trap; the faster the trap is operated, the more gas is required to ensure positrons interact with the buffer gases and cool sufficiently.

Factors in determining good operating pressures for the N_2 and CF_4 are evident in the PALS spectra collected. Insufficient gas pressures (of either N_2 or CF_4) will result in uncooled positrons, or conversely insufficient cooling time in the trap cycle, which manifest as pre-pulse counts on the measured PALS spectra. This will also result in poor count rates and a wide temporal spread. Too much gas in the trap will result in excessive positron loss through annihilation with the buffer gases, as well as unwanted positron scattering from the buffer gases as the bunched pulse leaves the trap. Positrons that scatter on exiting the trap reach the sample stage much later than the bunched positrons and create a large, approximately exponential, decaying tail in the collected PALS spectra. Tuning the trap potentials and gas pressures to achieve a bunched positron beam that is suitable for experimental use can be challenging due to the large parameter space of interacting variables to tune.

After the trap, the pulsed beam passes through a moveable aperture plate, which is used to define the beam diameter used for experiments. This gives the option to reduce the

beam spot size on the target at the sample stage in the case of particularly small samples. Reducing the beam diameter in this way comes at the cost of experimental count rate.

3.2.3 Sample Stage

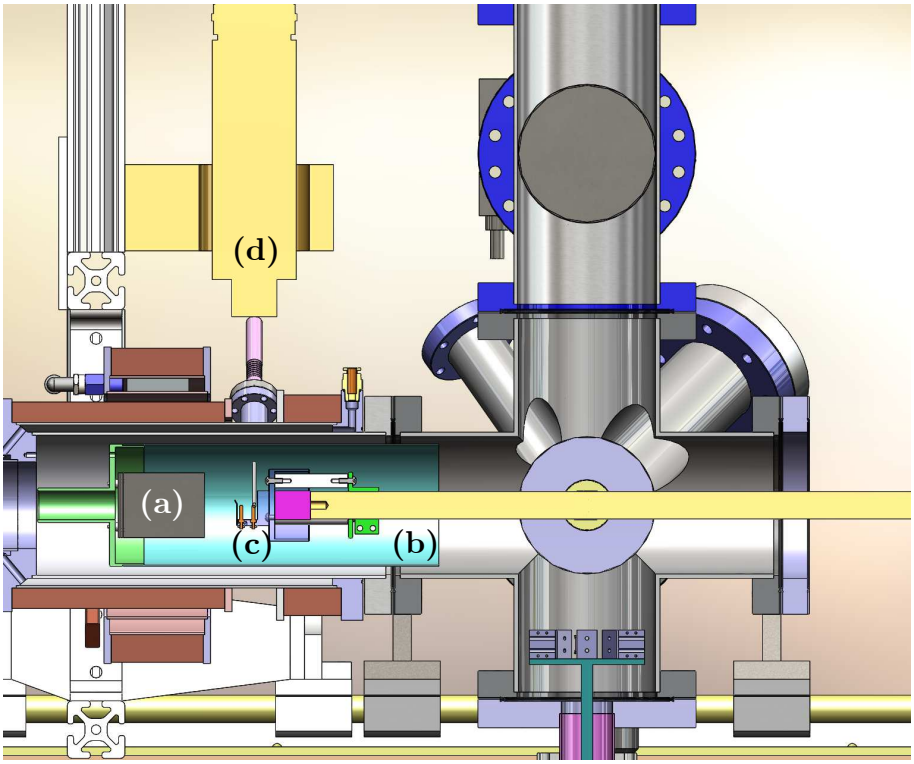

Figure 3.9: Schematic of the sample stage. (a) the $\vec{E} \times \vec{B}$ region, in dark grey. (b) the high voltage can for sample bias, background in turquoise. (c) sample holder on adjustable $x - y$ arm. (d) Photomultiplier tube and BaF_2 detector assembly

The final stage of the experiment is the section where the positron beam and target interact, and includes the detector for the PALS measurement, shown in figure 3.9.

To set the interaction energy between the beam and sample, the sample is located within a high voltage can which can be biased between 0 - 20kV. Depth profiling of samples can be performed by measuring the same sample with increasing bias, to probe deeper into the sample.

The start signal for the positron lifetime measurement is triggered by the dump cycle of the trap. Annihilation photons are collected by a fast BaF_2 scintillator model 1M1BAF2/2-X and an XP2020Q photomultiplier tube (PMT) from Saint–Gobain Crystals, which gives the stop signal for the lifetime measurement. The lifetime measurement is made using a ComTec P7889 fast timing card and associated computer software, which

takes in the start signal from the trap stage and the stop signal from the BaF_2 and PMT.

The data collected is a histogram with a bin width of 100ps, and to ensure high quality data the spectra collected are allowed to accumulate for several million counts, as detailed in section 2.4. For a typical sample measurement 1.5×10^6 counts are collected and for higher quality measurements or instrument function measurements greater than 3.5×10^6 counts are collected. With count rates of approximately $200 - 300$ counts per second, shorter measurements take between $1.5 - 2.5$ hours, and instrument functions take between $3 - 5$ hours. The instrument function use is discussed in greater detail in section 3.5.

Reduction of Reflected Positrons

At all implantation energies and for all materials there is some fraction of the positron beam which is reflected backwards from the surface. In the experiment the reflected positrons can annihilate away from the target but close enough to the PMT that the annihilation photons are detected, or be reflect again from the potential surface at the entrance to the high voltage can back onto the target. Collecting data from these unwanted reflected positrons can generate a secondary peak in the PALS spectra, away from the main peak and later in time, due to the time taken for these positrons to reflect then annihilate.

To reduce the impact of counts collected from positrons annihilating away from the sample due to reflection, the BaF_2 crystal is jacketed with a lead collimator, and the incoming positron beam travels through an $\vec{E} \times \vec{B}$ field before interacting with the target, as shown by figure 3.9. This field moves the positrons in the same direction regardless of incident direction, thus reflected positrons can be moved in way which significantly reduces the solid angle acceptance of annihilation photons from reflected positrons. In the current experimental configuration the $\vec{E} \times \vec{B}$ field moves the positrons downwards, away from the BaF_2 scintillator, which is located above the target. Therefore reflected positrons are stepped downwards twice, once on the first pass through the $\vec{E} \times \vec{B}$ field and a second time when reflected. Reflected positrons annihilate on the wall of the vacuum chamber far away from the sample with a greatly reduced solid angle to the BaF_2 scintillator, significantly reducing the number of counts from reflected positrons in the PALS spectra.

The $\vec{E} \times \vec{B}$ drift velocity is given by:

$$\vec{v}_E = \frac{\vec{E} \times \vec{B}}{B^2} \tag{3.2}$$

and to achieve consistent deflection the potential applied to the $\vec{E} \times \vec{B}$ system scales proportionally with the interaction energy of the positron beam and target.

Since the value applied to the $\vec{E} \times \vec{B}$ system varies with the implantation energy of the positron beam, the position of the positron beam at the sample stage changes with the $\vec{E} \times \vec{B}$ field. For this reason the ability to manipulate the position of the sample in the $x-y$ plane is particularly important so alignment measurements can be made directly. To enable control of the sample position, the arm holding the sample is mounted on a manipulator stage, which allows movement in the $x - y$ plane, and calibration measurements for beam position can be made for each experimental session.

3.3 Typical Operating Parameters

The trap operates at approximately 3000Hz, with ballast pressures of N_2 at 100mTorr and CF_4 at 230mTorr. The pulsed positron beam is ejected at $\simeq$ 140eV. This results in a typical positron pulse of $\simeq$ 900ps (FWHM), with 300 counts per second at the detector.

Spectra are typically 1.5×10^6 counts and instrument functions are typically 3.5×10^6 counts to ensure statistical significance and precision, which brings measurement times to between $3 - 5$ hours.

3.4 Preliminary Estimation and Simulation

The information from positron annihilation is dependent on the region in which the positron annihilates, and so selecting the correct positron implantation energy is fundamental to investigating specific regions of the sample. As previously described in section 2.3.1, the implantation of positrons follows a Makhov distribution dependent on the material and implantation energy.

For more straight forward PALS measurements, in a sample of uniform density, a Makhov distribution can easily be generated for incident positron energy and sample density, providing mean and maximum positron penetration depth. This distribution can

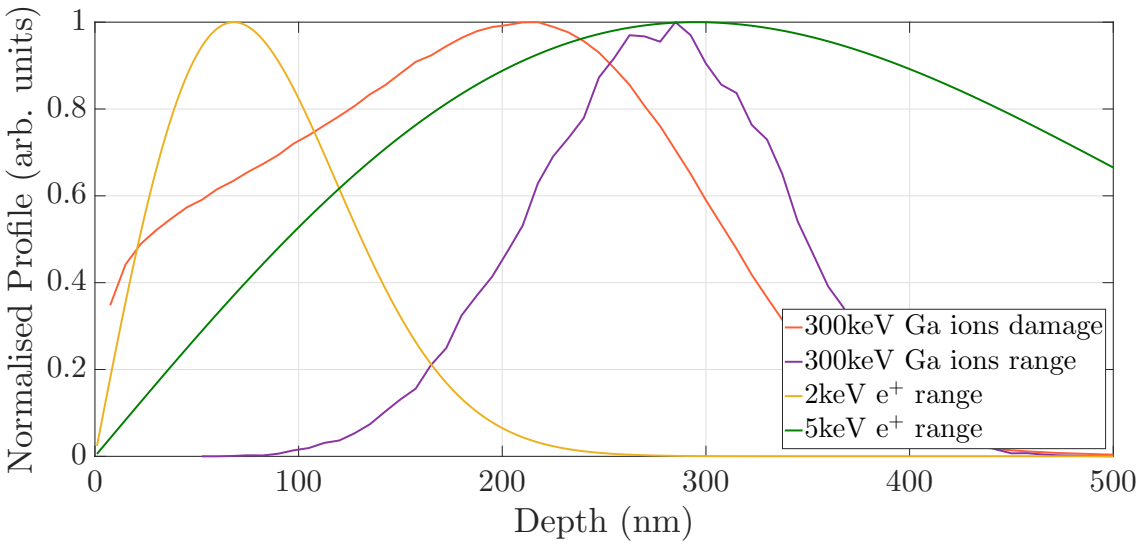

Figure 3.10: Simulated implantation of 300keV gallium ions into a substrate of Kapton polyimide film. The positrons implanted at 2keV investigate damage at the near surface region and the positrons implanted at 5keV investigate the region of maximum damage caused by the gallium ions.

be compared to information about sample preparation, and thus tuned to overlap any regions of interest as best possible. Commonly there will be different regions within a sample that are of interest, and so multiple measurements will be made. In the case of Gallium implanted Kapton, figure 3.10 shows the SRIM/TRIM calculated damage profile [67,68], with overlaid positron implantation distributions. This particular study examined two regions; one near surface and another overlapping the highest damaged region from the implanted Gallium ions.

In the case of a layered sample, getting an estimate of the positron implantation depths can be more difficult, due to the differences in each layer. More careful simulation is required than a simple Makhov profile to select appropriate positron implantation energies. To do this pyPenelope is used [69]. The pyPenelope code will simulate positron implantation into layered materials taking into acount the material composition and density, and an example of this type of simulation on a organic LED with several layers of different density is shown in figure 3.11. Difficulties arise when extracting information from multi-layered samples due to higher energy positrons sampling and annihilating at preceding depths, as the implantation distribution “smears out” as mentioned in section 2.3.1 and illustrated by figure 2.6.

The results of the various simulation techniques are compared to the damage profiles

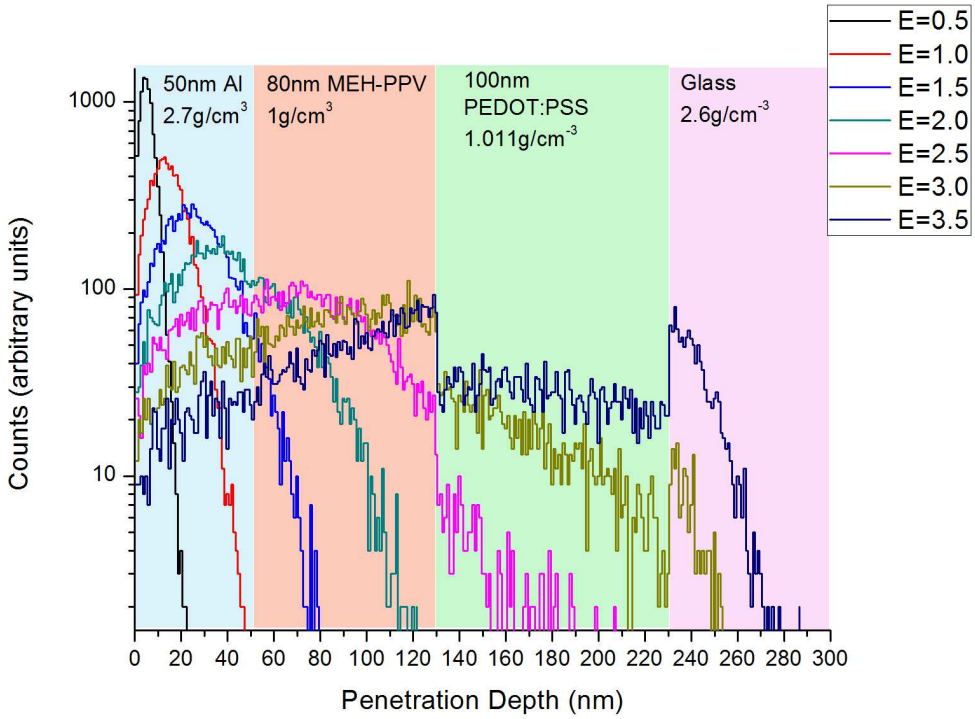

Figure 3.11: pyPenelope simulation of 0.5 - 3.5keV positrons implanted in to a layered OLED. This figure demonstrates the clear density dependence in positron implantation depth.

of the sample materials, so that the positrons can be implanted into regions of interest. If there are multiple regions of interest, a series of measurements of different energies of positrons can be made to investigate the sample fully.

3.5 Data Analysis

Analysis is conducted with a bespoke analysis package, CAMSfit, which was custom built for data analysis in this experiment [70]. A PALS spectrum of a pristine sample relevant to the material under investigation is used as an instrument function, which allows relative measurements to be made. This gives focus to the analysis and allows for evolutionary measurements of sample series, which can reveal more than an absolute measurement in typical bench top type PALS measurements. To ensure reliability in the analysis, the same PALS spectra is used as an instrument function across measurements of the same series. New instrument function measurements are made when changing positron implantation energy, or a new series of measurements is began.

The use of an instrument function of a related material to the one being studied for PALS lifetimes makes the PALS measurement insensitive to the intrinsic positron lifetimes that are present in the reference material. This can benefit the PALS analysis as the experiment becomes more sensitive to any changes between the reference spectra and the sample being investigated. For example, in the characterisation of defects induced by ion implantation into a substrate, the material used as the instrument function should be a pristine sample of the substrate, therefore any observed positron lifetimes would be due only to the ion implantation performed on the sample being investigated.

As described in section 2.4, the analysis of a PALS measurement is done by examining the histogram of positron lifetimes inside a particular material sample. In the generic case, the line shape can be described by equation (2.6), and data could be extracted by fitting an equation in this form. An additional benefit to using an arbitrary instrument function is that systematic features present in experimental results will be present in all collected spectra and thus excluded from analysis. One effect that is present in the measurements presented here is a long lifetime tail which is caused by positron scattering from buffer gasses as the positrons are ejected from the trap. Although this is a small overall contribution to the spectra is it significant enough that using the instrument function for analysis is preferred over a pure Gaussian curve or direct fitting using (2.6).

Although the PALS analysis can efficiently find differences between instrument function and measured PALS spectra, it does remove the ability to make absolute measurements of the intensity of the observed lifetimes (parameter I_n in equation (2.6)) and no bulk lifetimes can be measured. As such, the intensities associated with the observed lifetimes are relative to the programme of measurements across similar samples and are not absolute measurements.

Chapter 4

Development of a Doppler Broadening Spectroscopy Experiment

This chapter details the development of an extension to the positrons materials beamline at ANU to study the Doppler broadening of annihilation radiation (DBAR) from positrons annihilating with electrons in solid targets. Several experimental designs were tested thoroughly until a final design was selected and fully characterised.

4.1 Motivation

PALS and DBAR are complementary techniques and measurements made with one technique can be utilised to inform the other. As previously explored in chapter 2, the DBAR measurement examines the electron momentum at the positron annihilation site inside the material being studied. This not only gives information on concentration of defects through the S parameter, but gives further information about the chemical environment of the annihilation site through the W parameter and high momentum fraction studies of the DBAR spectra.

The DBAR experiment uses the existing positron materials beamline, however the trap stage and PALS measurement apparatus are not used; the trap is turned off (with the electrodes grounded) and buffer gases removed to allow the continuous primary moderated beam to propagate through the entire beamline. Data collection of photon energies to measure the Doppler broadening is conducted using a new detector and associated equipment. The addition of the DBAR experiment does not interfere with the ability to

perform PALS measurements and the measurement techniques can be readily alternated.

Using only the primary beam for DBAR measurements significantly increases the at-sample count rate (typically $\simeq$ 2000 counts per second) and results in a much shorter measurement duration compared to making measurements with the PALS technique. With a much shorter measurement duration, full depth profiling of a target sample becomes feasible, therefore a much more complete positron characterisation can be performed.

The faster DBAR measurement can inform the programme of PALS measurements that are conducted. A full depth profiling of a sample using the DBAR technique will yield results that can be analysed to find interesting features to be further investigated by other measurements, such as PALS. By combining relatively quick depth profiling to aid in the choice of positron implantation energy for PALS measurements, a more thorough characterisation of targets can be performed.

4.2 Positron Materials Beamline for DBAR Experiments

As briefly mentioned, the positron beam for DBAR measurements is formed using the primary beam alone, the trap is not used, to provide a constant beam of positrons propagating through the experiment. The electrodes that make up the trap, shown in figure 3.4, are all grounded and the buffer gases removed from the trap. The energy of the beam is therefore set by the bias applied to the moderator, and was 30eV in this case.

At the exit of the trap, an aperture plate was used to limit the spot size of the positron beam so that it could be reduced in size and properly aligned on the target at the sample stage. The width of the aperture used was 11.4mm in diameter, corresponding to an on-target spot size of approximately 5mm due to the difference in magnetic fields in the different stages of the positron materials beamline. [47].

At the sample stage, the interaction energy between the positron beam and the target sample was set by the high voltage, as described in section 3.2.3. The $\vec{E} \times \vec{B}$ assembly for reducing reflected positrons was not used for DBAR measurements.

A high purity germanium (HPGe) detector, cooling system, and pre-amplifier apparatus (described in detail in the following section) was placed adjacent to the vacuum system surrounding the sample stage at the location of the sample holder, perpendicular to the beamline. Due to the thickness of the vacuum chamber and the surrounding solenoids that

generate the confining magnetic fields, the detector endcap was 15cm from the geometric centre of the vacuum chamber.

All magnetic fields remained as described in section 3.2 in order to radially confine the continuous positron beam.

4.3 High Purity Germanium Detectors

A high purity germanium (HPGe) semiconductor detector is very sensitive to ionising radiation, in particular the detector response is proportional to the energy that is deposited from the incident radiation.

The HPGe detector is constructed of a germanium crystal diode, with a positive-intrinsic-negative (P-I-N) configuration which, under reverse bias, is sensitive to incident photons. With a suitably large bias applied to the semiconductor there is a large electric field between the P- and N- contacts. When a photon passes through the intrinsic region of the semiconductor, charge carriers in the form of electron-hole pairs are produced and swept towards the P- and N- electrodes due to the electric field generated by the bias. The amount of charge carriers created is dependent on the the energy deposited into the I- region by the incident photon [71].

The charge generated by photon absorption events is collected by an integrating amplifier which forms this charge into a voltage pulse which can be measured, building up a spectrum of measured photon energies.

4.3.1 Coaxial Standard Electrode HPGe Detector

There are several different geometries of HPGe crystal design which are suited for different applications. In the case of this experiment, the energy region of interest is roughly between $450-550$keV as the energy of a single annihilation photon is 511keV, which makes a coaxial standard detector configuration suitable. The other more esoteric configurations provide sensitivity at different energy regimes as well as other characteristics unnecessary for this experimental configuration.

In this HPGe crystal the detector P- and N- regions are made by diffused lithium (N-) and implanted boron (P-) regions in the germanium crystal itself. The N- contact is not stable at room temperature and so the HPGe crystal must be stored at low temperatures

for long term detector stability. Storage at room temperature results in a thickening of the lithium layer and a reduction in detector efficiency, so the detector crystal is usually cooled by liquid nitrogen.

In operation, the detector needs to be cooled to prevent excessive thermally generated leakage currents in the I- region. Running the system at temperatures above that of liquid nitrogen results in almost total loss of information from incident photons.

4.3.2 Detector Pre-Amplifier

Built into the HPGe system is a pre-amplifier which is housed within the cooling system for improved performance, significantly reducing noise. The pre-amplifier is a Canberra 2002c model which integrates the charge deposited in the HPGe crystal and convolutes it with an exponential decay of 50μs.

On the exterior of the HPGe detector and coolant system there is access to the available output terminals, as well as a bias voltage input, which allows the connection of the pre-amplifier into the detector chain of the experiment.

4.3.3 Detector Cooling System

As noted previously, HPGe detector systems require cooling to liquid nitrogen temperatures for operation, and housing the detector pre-amplifier in the coolant system also aids performance.

Traditionally, dewars of liquid nitrogen are used to cool HPGe systems. Depending on the size of the dewar, keeping the system at the correct temperature can result in frequent refilling of the dewar.

Since the positron research laboratory at ANU does not already make use of liquid nitrogen cooling in other experiments, adding a liquid nitrogen cooling system would be expensive and refilling a single dewar was deemed an unproductive use of time. For these reasons an electronically cooled cryostat system has been used to refrigerate the HPGe system.

The Cryo-pulse 5 Plus (CP5+) system from Canberra utilises a pulse-tube gas cooler which is hermetically sealed, requiring no gas refill or maintenance by the user. The system consists of a coldhead assembly attached to the HPGe detector crystal and a bench top

power controller. The power controller regulates the voltages required to run the CP5+ and maintain a temperature of −185°C and also maintains fail-safe logic to manage the detector bias supply in case the detector is above temperature, preventing damage from occurring.

4.4 Initial Resolution Benchmark

To confirm that the HPGe crystal detector, coolant system, and pre-amplifier was working as expected and to the manufacturer's calibration, a series of tests were conducted. The baseline confirmation tests were conducted using spectroscopic equipment used by the Department of Nuclear Physics at ANU that are frequently used for similar measurements and are well characterised.

The intent of the DBAR experiment is to measure the Doppler broadening of the positron annihilation photopeak, the effective measure of detector performance is the resolution at the 511keV region. The resolution can be determined by characterising the detector using well know emissions from radioactive isotopes and plotting the full-width at half-maximum as a function of photon emission energy — a standard method of detector characterisation used in spectroscopy.

The radioactive isotopes used to generate calibration spectra have energy variations which are vanishingly small in comparison to the resolution of the detector and therefore any broadening of emission lines can be attributed to the detector resolution alone.

4.4.1 Manufacturer's Calibration

The cGe crystal has been calibrated by the manufacturer with radioisotopes ^{57}Co and ^{60}Co, giving full-width at half-maximum (effective resolution) value. The measurements of the emission lines of these isotopes was performed using a spectroscopic amplifier with a shaping time of 4μs.

Isotope	Energy (keV)	FWHM (keV)
^{57}Co	122	0.976
^{60}Co	1332	1.794
Calculated	511	1.24

Table 4.1: Manufacturer's measured efficiency and calculated efficiency at 511keV

Using a simple linear interpolation between the two stated resolutions from the manufacturer (shown in table 4.1), the estimated FWHM at 511keV is 1.24keV. This calibration is the reference with which to compare the various experimental methods outlined in this chapter.

The estimated efficiency for the Ge detector has been interpreted from the literature provided with the experimental equipment when purchased from Canberra, which has been reproduced and shown in figure 4.1.

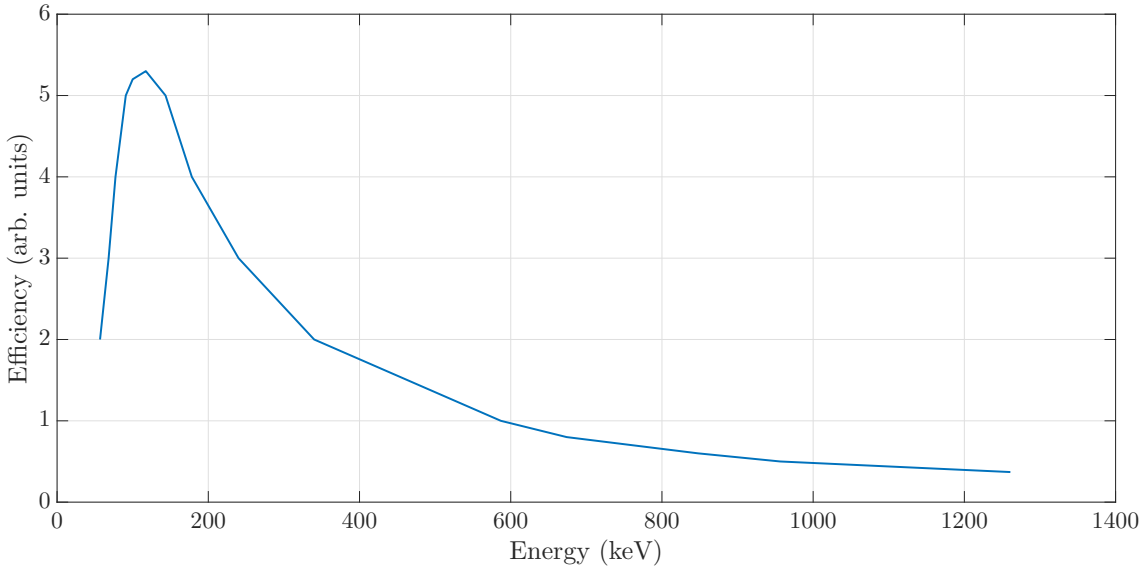

Figure 4.1: Typical absolute efficiency curve for coaxial Ge detector, with 10% relative efficiency and a 2.5cm source to end-cap spacing. Data estimated and interpreted from printed material "Germanium Detectors: User's Manual", provided by Canberra with detector purchase.

4.4.2 Experimental Set-up

The initial resolution benchmark experiment was set up using the following equipment, borrowed from the Department of Nuclear Physics. The equipment has previously been verified in similar applications, providing a consistent experimental set-up with which to benchmark the HPGe crystal.

The experimental configuration was the HPGe detector with CP5+ cooling system and built in Canberra 2002C pre-amplifier connected by shielded BNC cable to an Ortec 855 Dual Channel Spectroscopic Amplifier. The ouput of the amplifier was directed to a Pocket MCA 8000A multi-channel analyser [72] and the associated ADMCA software

was used for spectra collection [73]. The HPGe detector was cooled down over a 12 hour period before the high voltage bias supply connected to the pre-amplifier and any bias applied. The pre-amplifier was configured at a pre-set output gain of 100mV per MeV, and the output pulses were shaped and amplified by the Ortec 855 spectroscopic amplifier with a shaping time of 3μs. The bias on the high voltage supply at the pre-amplifier was set to the manufacturer recommended value of 4.2kV.

The radioactive source used for calibration was a "check source" of ^{152}Eu, with well known spectra detailed in reference [74]. The source was placed approximately 10cm away from the detector end cap. Figure 4.2 shows the resulting spectrum of ^{152}Eu that was collected under the specified conditions.

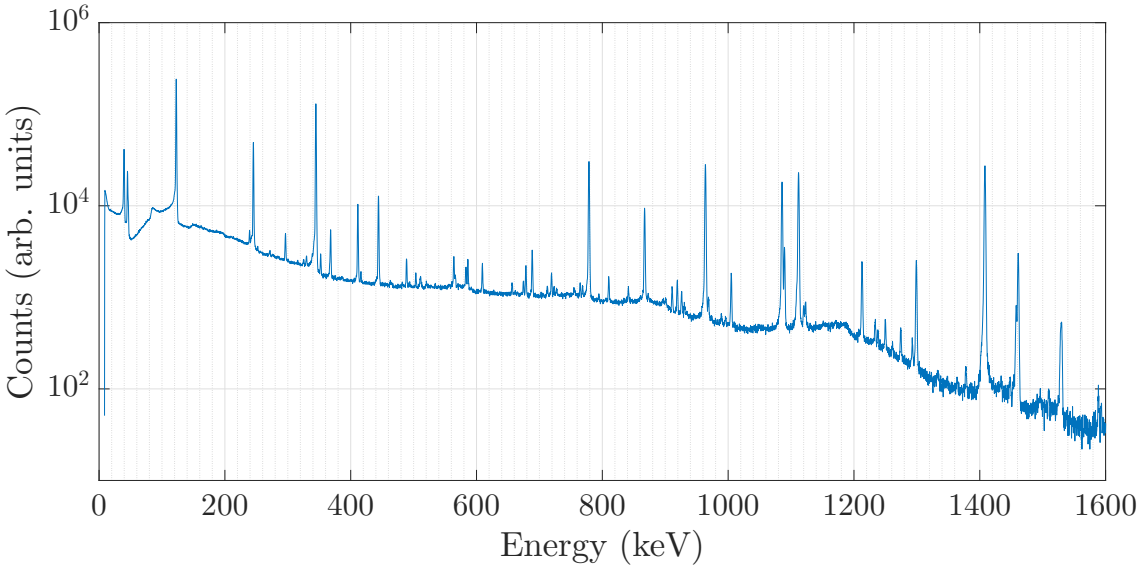

Figure 4.2: Results of the calibration; the spectrum of ^{152}Eu

4.4.3 Calibrated results

The spectrum of ^{152}Eu as shown in figure 4.2 was accumulated for approximately 14×10^6 counts in total. The x-scale was calibrated using the well known peak positions for the most probable photon emissions in ^{152}Eu [74]. The x-scale was then fit with a quadratic function to calibrate from bins to energy, in the form of equation (4.1):

$$A + Bx + Cx^2 \tag{4.1}$$

The results of the fitting of the quadratic function (4.1) resulted in the following

parameters for the calibration, shown in equation (4.2).

$$A = 4.77758, \quad B = 0.260488, \quad C = 1.07727 \times 10^{-7} \tag{4.2}$$

Following the x-scale calibration, to measure the resolution of the system, the full-width at half-maximum of the calibration peaks was measured, with the results presented in table 4.2:

Peak Position	FWHM (keV)	Uncertainty (keV)
121.88	1.1504	0.15
244.86	1.1643	0.44
344.72	1.2431	0.17
778.16	1.5582	0.32
963.90	1.6657	0.3
1111.62	1.7379	0.33
1408.013	1.9185	0.23

Table 4.2: Calibration results

4.4.4 Conclusion

The calculated resolution at 511keV for this experimental benchmark is 1.37keV, interpolated from the results in table 4.2. Compared to the manufacturer's supplied calibration and calculated resolution at 511keV of 1.24keV, the HPGe detector system is functioning as expected with the apparatus used in the benchmark measurement. The difference in resolution between this measurement and the manufacturer's calibration is expected as the manufacturer's calibration was performed using a spectroscopic amplifier shaping time of 4μs, which will result in a higher resolution.

The benchmark measurement performed confirms that the detector is performing as expected and will suitable to be used as part of the DBAR measurement.

4.5 Full Digital DBAR System

In this section, a digital data acquisition system is characterised as the method for collecting data in DBAR measurements.

4.5.1 Motivation for a fully digital DBAR system

Implementing a digital data acquisition and analysis system for DBAR spectroscopy is not the most common configuration in spectroscopy, but with the availability and quality of modern digitizers as well as the amount of computation power available in desktop PCs it is becoming more widely used. This digital technique has been implemented successfully by several groups [60, 75, 76].

A benefit of using a digital spectroscopy system is that measurement data is collected at the lowest level possible in the system — the full information from the pre-amplifier is recorded. Analogue systems process the signal output from the pre-amplifier using analogue circuitry for pulse shaping, which means that the original signal is not recoverable. Measurement at the low level of pre-amplifier output enables analysis to be repeated on the same data sets if better analysis tools are made available or the analysis method is improved, and in principle any analogue pulse shaping through circuitry is reproducible through digital signal processing. Different analysis techniques can be attempted on the same data sets to corroborate results or tests for different information within the results without the need to repeat lengthy experiments.

Making use of the data directly from the pre-amplifier also allows for analysis and inclusion of signals that would not be usable in a traditional analogue configuration. For example, pile-up events can be made usable in a digital system by extracting the superimposed waveforms using the mathematical analysis, resulting in higher throughput and count rates in the same amount of experimental run time as an analogue system.

4.5.2 Experimental Set-up

The experimental apparatus is set up in a similar arrangement to analogue spectroscopy experiments, however there is less equipment in the detection chain. Figure 4.3 is a schematic of the set-up, which shows there are only 3 main components: The HPGe and coolant system, the digitizer, and a computer for storing data and later analysis.

Figure 4.4 shows a example of a pulse from the pre-amplifier attached to the HPGe system. The pulse is the integrated charge from the photon interacting with the depleted region in the semiconductor, which has been convoluted with an exponential decay by the pre-amplifier, and the natural Gaussian response of the detector.

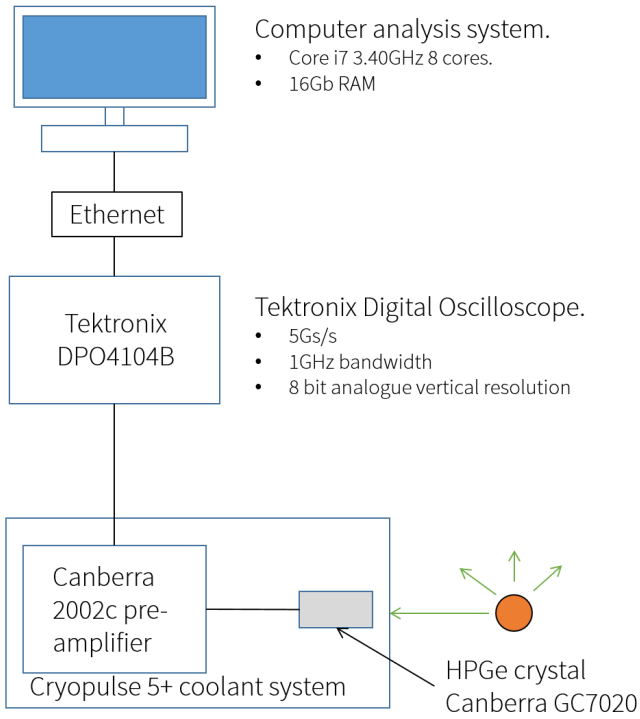

Figure 4.3: Block diagram for the digital setup

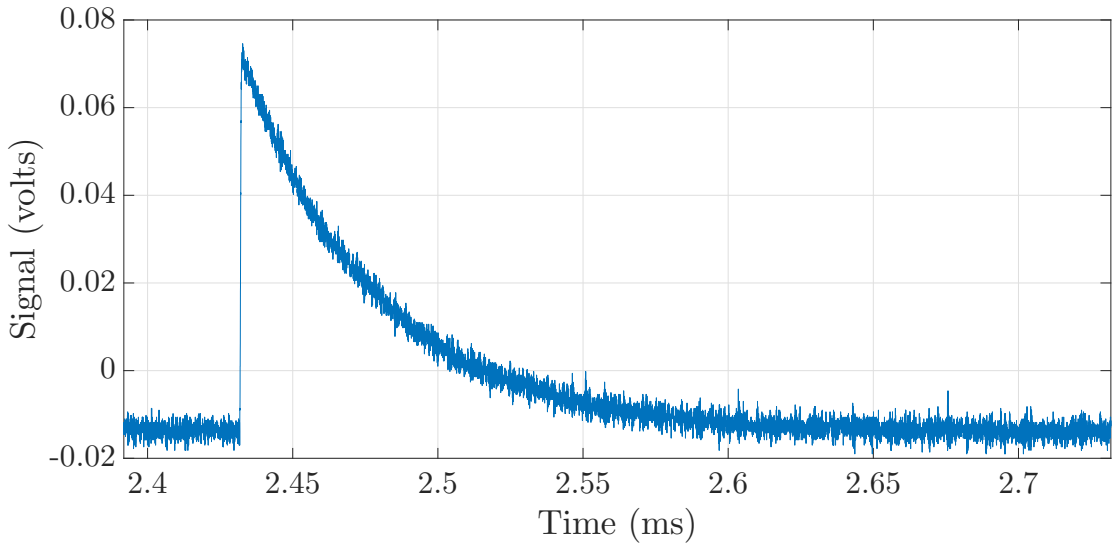

Figure 4.4: Example of one waveform from the pre-amplifier as digitized by a Tektronics DPO4140B oscilloscope.

4.5.3 Digitiser Resolution

The digitizer y axis, or vertical, resolution is the primary source of uncertainty in this experimental design, as it determines the ability to accurately sample the incoming analogue waveform. As the pulse height of the waveform is directly proportional to the energy from in the incident photon that has been absorbed by the HPGe crystal, it is important to be able to accurately recover the pulse height.

In conducting experiments using digitizers, we choose an incoming signal range over which the digitizer will sample the signal in discrete steps. The precision in the digitizer is determined by the number of bits, which are the number of discrete values a signal is digitized to for a given input signal range. There will always be loss of information when digitizing an analogue signal as the value will be "rounded" up or down to the closest digitizer level. Determining the vertical resolution of the digitizer is the digital uncertainty — the difference between digitizing levels. For example, if a digital signal between 0–5V is being digitized by an 8 bit digitizer, the resolution is given by (4.3).

$$\sigma_{digital} = \frac{5V}{2^8} = \frac{5V}{256} \simeq 0.0195V \tag{4.3}$$

The oscilloscope being used as the digitizer in this experiment a Tektronics DPO4140B. This oscilloscope has an 8 bit vertical resolution in standard operation mode and effective 11 bit vertical resolution in high resolution mode [77]. As the output gain of the pre-amplifier is 100mV/MeV the oscilloscope will operate at 10mV per division, with 10 divisions in total vertical range to give a photon energy measurement range of 0–1MeV which puts the region of interest, 511keV photopeak, in the middle of this range.

$$\sigma_{V11bit} = \frac{0.1V}{2^{11}} = 4.8828 \times 10^{-5}V \simeq 0.5\text{keV} \tag{4.4}$$

Using the high resolution mode available on the oscilloscope gives effective 11 bit vertical resolution so the resolution can be calculated in similar way to equation (4.3). This calculation, shown in (4.4), results in an oscilloscope vertical resolution of approximately 0.5keV, which is approximately 0.01% of 511keV, significantly smaller than the inherent resolution of the HPGe detector itself.

4.5.4 Data Analysis

The energy deposited in the Ge crystal is converted to an output pulse which is convoluted with an exponential decay in the pre-amplifier circuitry. The height of the signal pulse is directly proportional to the absorbed photon energy. In analogue systems, this signal is converted into a semi-gaussian pulse shape using capacitors in parallel and series. In the case of this digital signal processing method of data analysis, the signal from the pre-amplifier will be measured directly. This is achieved by using curve fitting techniques to determine the pulse height and therefore the photon energy that was deposited into the detector crystal.

As described by Cizek *et al.* [60], the digitizer waveform is the convolution of the heaviside step function, the exponential, decay from the pre-amplifier, and a Gaussian resolution function, superimposed on a linear background:

$$\left[\frac{1}{\sigma\sqrt{2\pi}}\exp\left(\frac{-t^2}{2\sigma^2}\right)\right] * \left[A\Theta(t-t_0)\exp\left(-\lambda(t-t_0)\right)\right] + b \tag{4.5}$$

where $*$ denotes the convolution. This has an analytic solution which is:

$$\frac{1}{2}A\exp\left(\frac{1}{2}\lambda(\lambda\sigma^2 - 2(t-t_0))\right)\cdot \operatorname{erfc}\left(\frac{\lambda\sigma^2 + (t_0 - t)}{\sqrt{2}\sigma}\right) + b \tag{4.6}$$

Where the parameters in both equation (4.5) and (4.6) are as follows: A is the pulse amplitude, $\Theta(t-t_0)$ is the Heaviside step function with t_0 as the time at which the pulse occurs, σ is the Gaussian standard deviation, λ is the exponential decay constant from the pre-amplifier circuitry ($\frac{1}{50\mu s} = 20000$), and b is a linear background. The independent variable is t, time.

4.5.5 Waveform Fitting

Fitting the waveforms collected from the pre-amplifier using equation (4.6) is a standard fitting problem – there is the underlying signal in the form of voltage pulse from the pre-amplifier and modelled by the equation (4.6). In addition to the signal there will be random noise, as well as potential systematic uncertainty from the electronics or signal contamination from any pick-up on the cables used to connect the detector chain. Therefore the quality test for fitting results is based on the scatter in the data around the fit, and

the residuals. The fitting routine used is a Levenberg-Marquardt non-linear least squares fitting routine, which makes use of the residual between the fit and the observed values to determine the completion of the fitting algorithm.

There are many software packages that offer Levenberg-Marquardt fitting routines and several packages were used in the implementation of the code used to process the collected pre-amplifier waveforms. The code for fitting the waveforms was initially prototyped using MATLAB [78] and Python [79] to take advantage of the easily viewable output of results to rapidly iterate and improve. Once a full program was developed to properly process the pre-amplifier waveforms, the code base was migrated to C++, a compiled language, for faster execution times.

In C++ different Levenberg-Marquardt fitting libraries are available, and initially the library used was GSL [80]. GSL struggled in some aspects of this fitting problem due to the difference in order of magnitude in some of the fitted parameters in equation (4.6), which are detailed in table 4.3. A different library, ALGLIB [81], was adopted to implement the fitting algorithm in order to address this problem, as ALGLIB allows for explicit declaration of the scale of the fitted parameters which are taken into account by the algorithm during the fitting process, producing higher quality results.

Parameter	Magnitude
A	10^{-2}
λ	10^{+4}
σ	10^{-7}
t_0	10^{-3}
b	10^{-2}

Table 4.3: Order of magnitude for each fitted parameter

Table 4.3 shows that the difference in order of magnitude between the fitted parameters is at most 10^{11}, which is significant. If the implementation of the fitting routing does not properly respect these order of magnitude differences the change in residual base on change in parameter value for iteration of the fitting routine will cause large differences in tolerance parameters and parameters monitored to identify routing completion. The step size in varying the fitted parameters themselves must be scaled so that they are appropriate to the order of magnitude. For this reason, in C++ better fits were found by using ALGLIB as the code allows for explicit declaration of the scale of the fitted

parameters at run time.

The form of the analytic solution, shown in equation (4.6), has an exponential component and the decay constant λ can dramatically effect the fitting solutions such that the parameter A is given comparatively "less weight". Varying λ gives a large contribution to changing the residual as the exponential decay component acts over a large portion of the entire waveform. Therefore the fitting algorithm can prioritise λ at the expense of accuracy in the other parameters, which are of greater significance in this experiment.

To attempt to limit the domination of the parameter λ over the entire fit of the waveform, constraints were applied. While the constraints improved the fit quality, there is observed natural variation in λ from the pre-amplifier circuitry and therefore too strict constraints caused fitting to fail. If λ was not permitted to vary at all the fitting results were extremely poor.

Since the exponential decay component of the waveform acts over a comparatively large time scale, the portion of the collected pre-amplifier waveform supplied to the fitting algorithm was varied to find improvements in the fit quality. The waveform data from the pre-amplifier was manipulated to supply varying amounts of data points before and after an estimated t_0, which is the onset point of the waveform pulse. This resulted in changing the quality of fit due to the amount that the exponential decay parameter, λ, influenced the residual. The more data points that were included after t_0 increases the effective weight that the parameter λ has on the entire fit, while the inclusion of more data points before t_0 has a minimal impact on the effective quality of the fit, since the signal is effectively constant before $t = t_0$.

To quantify the location at which t_0 occurs in the data of the waveform passed to the fitting routine, the quantity *skew* was defined, shown in equation (4.7).

$$\text{skew} \equiv \frac{\text{no. data points before } t_0}{\text{total number of data points}} \tag{4.7}$$

For example, if there are 400 data points which describe the pre-amplifier waveform, t_0 occurring at data point 100 gives a skew of 0.25.

The graph figure 4.8 illustrates an example of the optimisation of the fitting routine, by changing the skew and fitting window size. The measure of success in this optimisation is minimisation of the peak width, on the z axis. As expected from this experiment, increas-

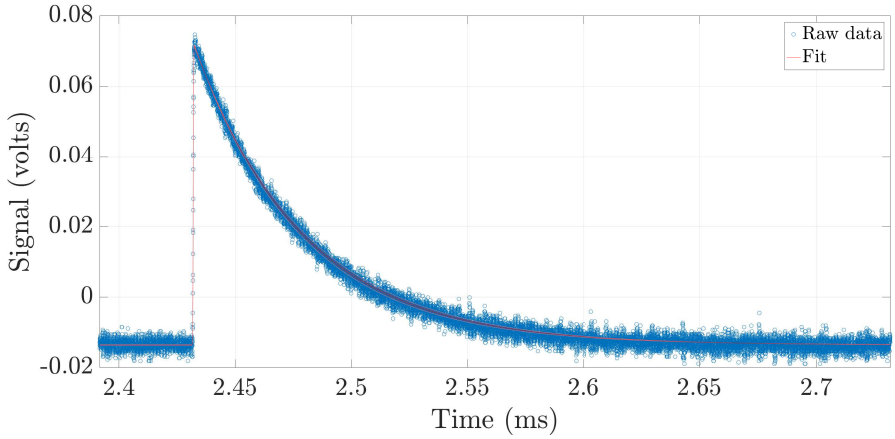

Figure 4.5: Example of digital data and fit of the entire waveform collected by the oscilloscope. The fitted parameters are detailed in table 4.3.

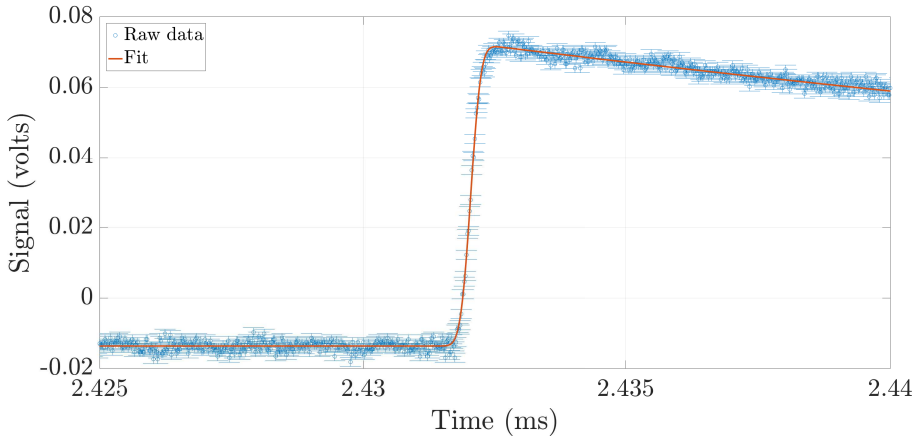

Figure 4.6: Full fitting of the rising edge of the pre-amplifier waveform, which shows the rounded onset and roll-off of the impulse from Gaussian resolution function resulting in a rounded. The region in $t < t_0$ is effectively constant. The fitted parameters are detailed in table 4.3.

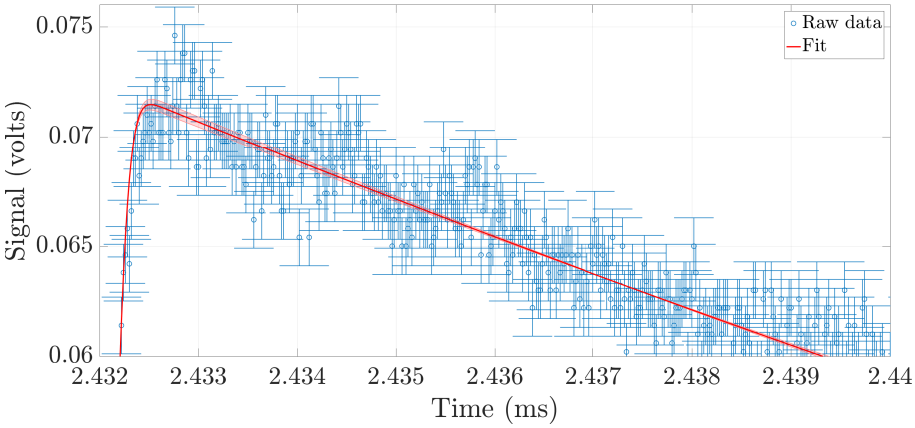

Figure 4.7: Detailed view of the waveform rising edge and waveform amplitude. The error bar (shaded region) is largest at the peak maxima. The fitted parameters are detailed in table 4.3.

Parameter	Value	Standard Error
A	8.61×10^{-2}	2.08×10^{-4}
λ	2.14×10^{4}	6.7×10^{2}
σ	1.52×10^{-7}	2.5×10^{-9}
t_0	2.432042×10^{-3}	1.8×10^{-9}
b	-1.368×10^{-2}	8.2×10^{-5}

Table 4.4: Fitted parameters with associated standard error from the example waveform shown in figures 4.5, 4.6, and 4.7.

ing the number of data points in the fitting window improves the fit quality. Changing the skew has a relatively small impact than changing the total proportion of the waveform supplied to the fitting algorithm, but a skew of 0.7 consistently gives a better fit.

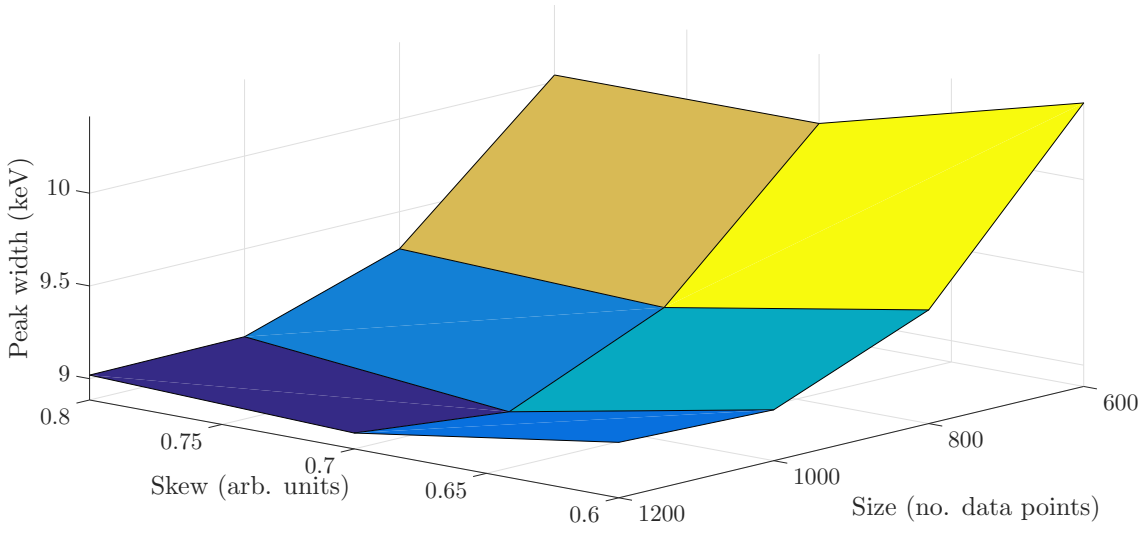

Figure 4.8: Example parameter search to improve the resolution of the 662keV photopeak in ^{137}Cs. The results show dependence on the skew and number of data points sent to the fitting routine.

Similar optimisation experiments were performed on other parameters supplied to the fitting routine in order to obtain the most accurate results from the fitting program.

The fitting of a single output waveform from the pre-amplifier is show in three views, in figures 4.5, 4.6, and 4.7. Figure 4.7 highlights the scatter in the data, and the effective fit's error bars at the peak region.

4.5.6 Digital Results

The spectrum of ^{152}Eu and ^{137}Cs as processed by the digital fitting method are shown in figures 4.9 and 4.10, respectively.

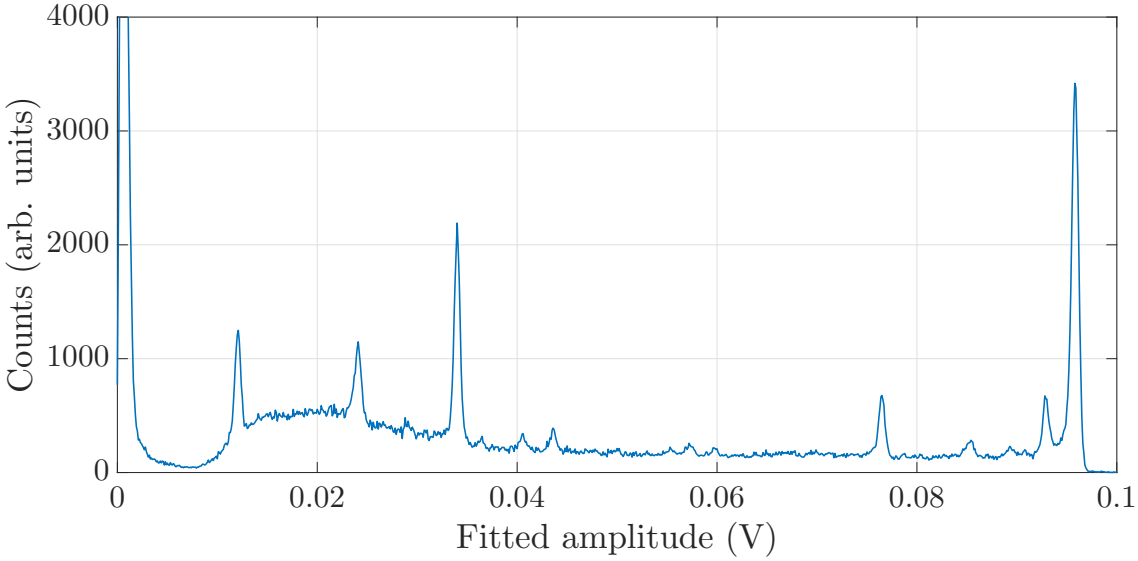

Figure 4.9: Spectrum of ^{152}Eu collected with the full digital experimental configuration for resolution calibration.

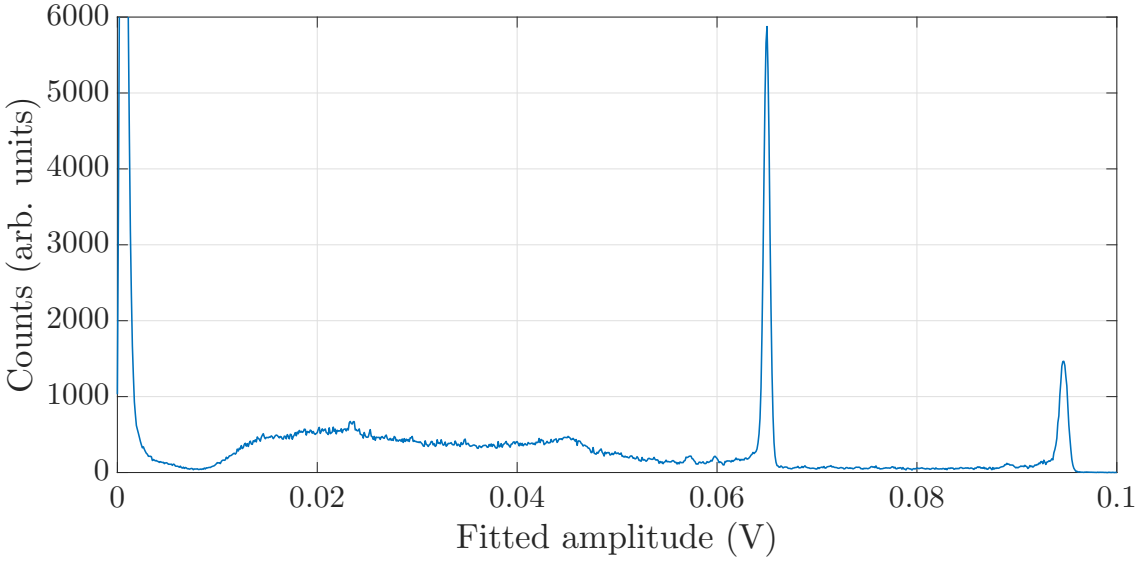

Figure 4.10: Spectrum of ^{137}Cs collected with the full digital experimental configuration for resolution calibration.

In the two spectra of ^{152}Eu and ^{137}Cs, the photo peaks appear in position as expected, however they seem to have very large FWHM. In the spectra of ^{137}Cs, the Compton features also appear as expected at the appropriate energies.

There are several features in the plots which are artefacts from the fitting process and are generated by poor quality fitting of bad waveforms. At the lowest amplitudes close to zero, there are a large amount of fitted amplitudes which correspond to bad quality waveforms or failed fits. At the high energy end there are a large amount of fitted amplitudes at approximately 0.095V. This corresponds to poor fits of detected photons which are outside the digitizer range — waveforms that clip.

To investigate how and why these artefacts arise, two measures of fit quality for the waveforms are used; χ^2 and adjusted R^2_{adj} values.

4.5.7 Investigating R^2_{adj}

The R^2 value is one of the outputs of the fitting routine in ALGLIB, and can be modified into R^2_{adj} which is more easily interpreted. R^2_{adj} is computed using R^2 and shown in equation (4.8).

$$R^2_{adj} = \frac{(1 - R^2)(N - 1)}{N - p - 1} \tag{4.8}$$

where N is the sample size and p is the number of predictor variables. In this case N is the number of points in the waveform being fitted, and p is the number of fitted parameters in equation (4.6), which is 6.

Figure 4.11 shows the distribution of R^2_{adj} values in the fitted spectrum of ^{152}Eu as shown in figure 4.9, showing a large number of R^2_{adj} between 0–0.05 and between 0.9–1.0.

If the waveform amplitudes are selected by the fitting quality based on the R^2_{adj} the features in the spectra change considerably, dependent on which threshold of R^2_{adj} value is allowed. The results of this process are shown in figure 4.12.

All spectra with fitted waveforms removed which do not meet the R^2_{adj} threshold criteria reduce the extremely high amount of fits with low amplitude however this process does not significantly change the amount of amplitudes fitted in the high voltage clipping region at approximately 0.095V.

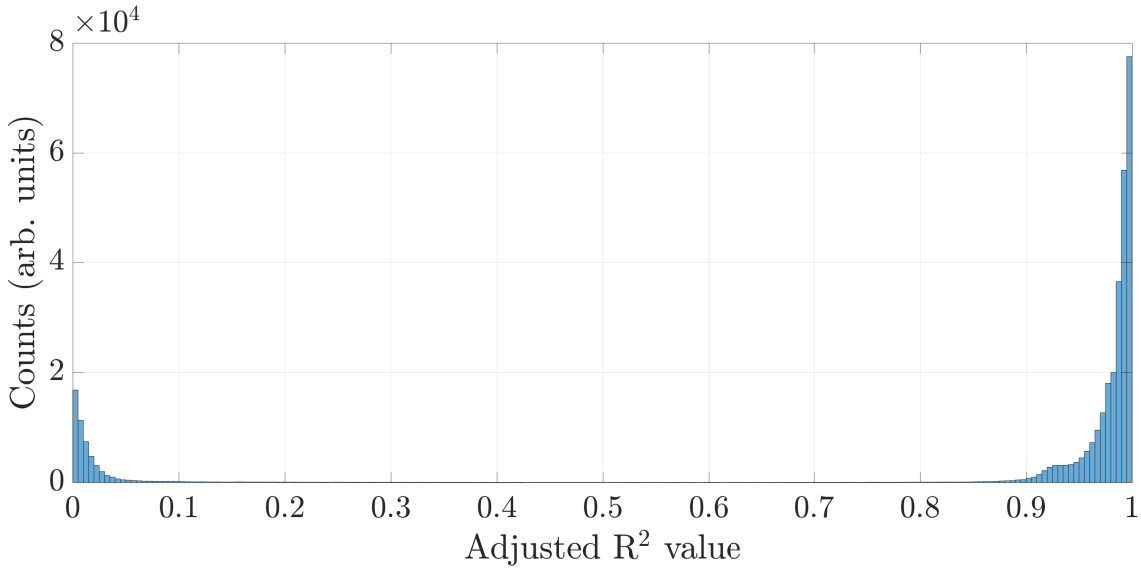

Figure 4.11: Histogram of R^2_{adj} values from fitting the digitizer waveforms collected from radioactive emissions of ^{152}Eu.

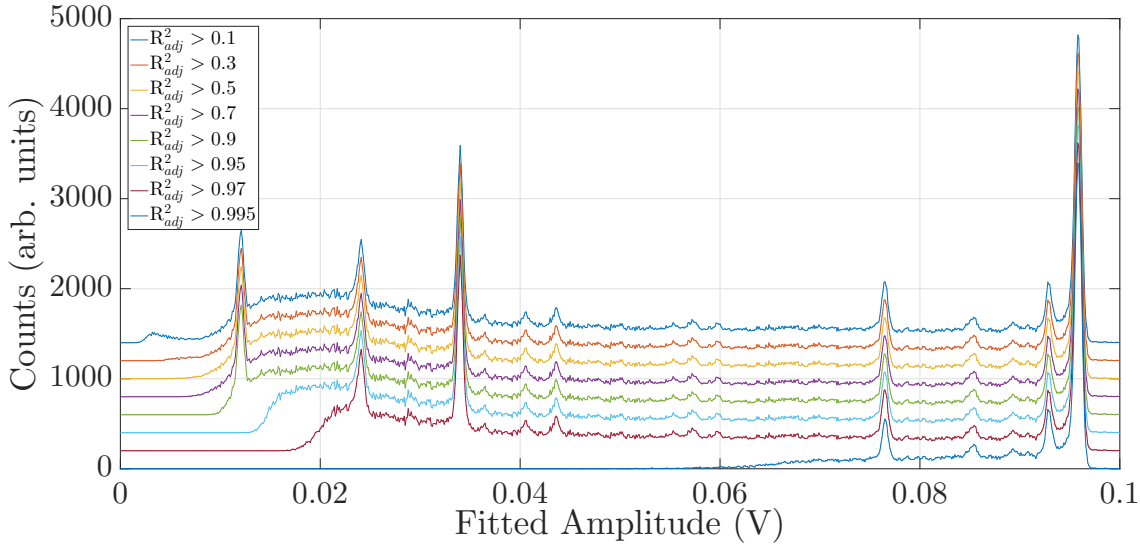

Figure 4.12: Spectrum of ^{152}Eu with only certain waveforms accepted for fitting quality, based on R^2_{adj}.

4.5.8 Investigating χ^2

The χ^2 value can be computed using the residual from the fit and should be close to 1 if the fit is perfect, although this depends on the number of data points being fitted and the number of fitted parameters [82].

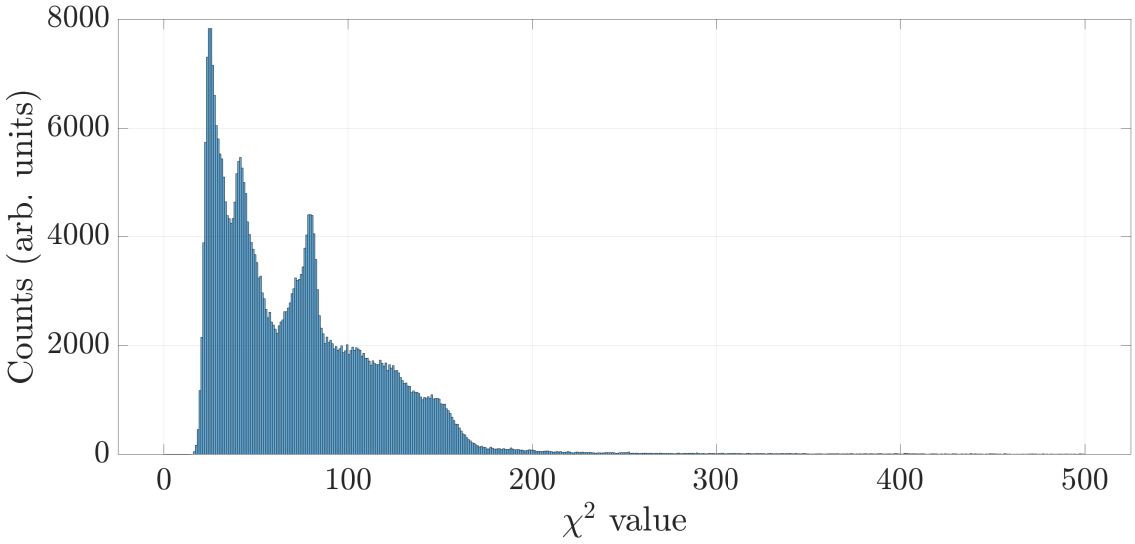

Figure 4.13: Histogram of χ^2 value from the spectrum of ^{152}Eu

Consulting the probability tables for the confidence interval for χ^2, figure 4.13 shows that all of the χ^2 values are in the 0.995 confidence interval due to the large number of degrees of freedom (1000 data points are used in the fitting routine) [82]. In the histogram of the χ^2 values for the spectrum of ^{152}Eu there are several peaks, which make for good threshold values to examine the effect of filtering the amplitudes based on the χ^2 value.

Figure 4.14 details the effects on the spectrum of ^{152}Eu by selecting allowed amplitudes based on the corresponding fit quality, as measured by χ^2. The effect of filtering the spectrum based on the χ^2 does not reduce the FWHM of the emission peaks from the radioactive sample, nor seem to remove the spurious data in the high and low amplitude regions. In fact, the restriction based on χ^2 appears to effect the whole spectra almost equally, which implies that there is some source of contamination in the waveforms which is influencing the fit quality.

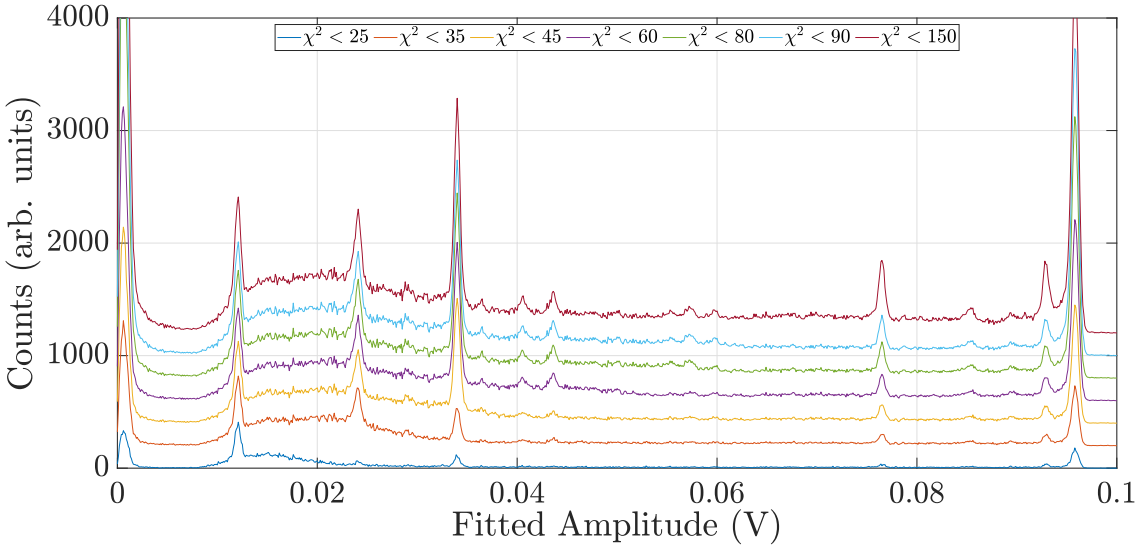

Figure 4.14: Spectrum of ^{152}Eu with only certain waveforms accepted for fitting quality, based on χ^2

4.5.9 Digital Fitting Resolution

The final results for the resolution measurement from digital fitting is shown are figure 4.15. The FWHM of the peaks of ^{152}Eu are considerably larger than the benchmark measurement in section 4.4.

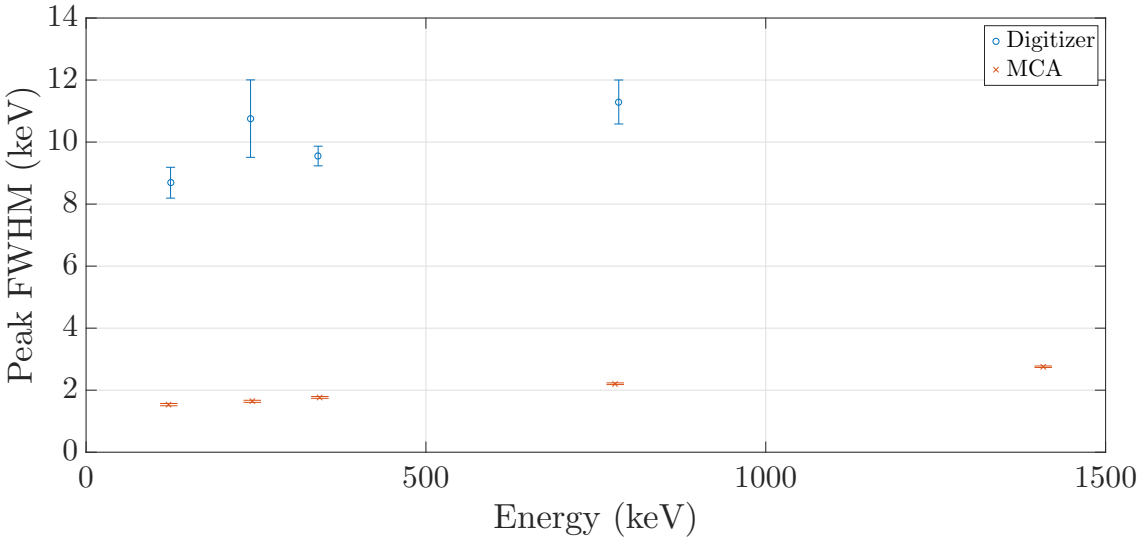

Figure 4.15: Resolution test using the FWHM of calibration peaks from ^{152}Eu with the full digital method, compared to initial testing using the analogue system and MCA.

4.5.10 Conclusion

The results of attempting to directly fit the pulse shapes from the pre-amplifier have produced results of insufficient quality for the purposes of a DBAR experiment. Despite being able to successfully reproduce the spectra of the test isotope, the resolution of the system is much worse than the initial benchmark made using analogue equipment in section 4.4.

The fitting problem was examined thoroughly and an appropriate library was found to implement the data analysis in C++, which was ALGLIB [81]. The pre-amplifier data was directly digitized using an oscilloscope and was processed by the fitting program. Investigations were made into the optimisation of the fitting routine to provide as accurate results as possible.

Although the optimisation of the digital fitting routine resulted in improved fit quality through explicit scaling of the fitting variables and parameter optimisation, this did not improve the results to a point of results usable for DBAR analysis.

4.6 Digital Filtering

Directly fitting the waveforms from the pre-amplifier produced poor resolution spectra, however there are further steps that can be taken to improve the pre-amplifier signal and the waveform quality before it is passed to the fitting routine.

4.6.1 Experimental Set-up

To iterate on the design used in section 4.5, a post-processing digital filter was implemented to reduce the noise in the waveforms collected from the pre-amplifier. The experimental configuration was kept the same as for the full digital DBAR experiment test, however the digital filtering step was put in place before the results were analysed by the curve fitting program. Design, prototyping, and testing of the digital filter was done in MATLAB using the Signal Processing Toolbox with the filter design tool [83].

The design of the digital filter was tailored to reduce the effects of noise in the signals collected from the HPGe detector system, based on analysis of as-collected waveforms and the analytic form of the HPGe detector pulses, described by equation (4.6).

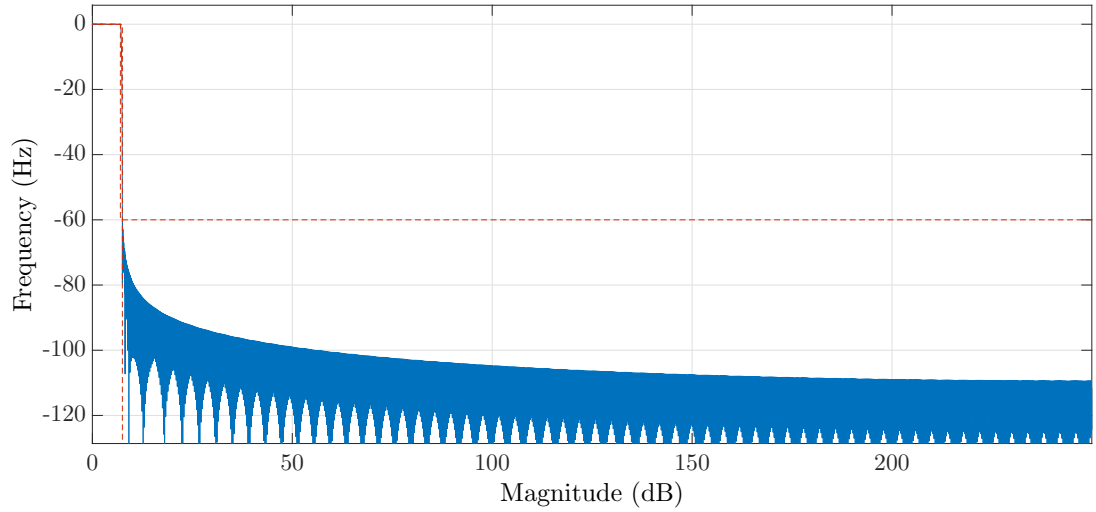

Figure 4.16: The frequency response of the digital filter, designed in MATLAB using the Signal Processing Toolbox with the filter design tool [83]. The filter was designed using the Kaiser window method [84], using a passband frequency of $7 \times 10^6 \pi \text{rad} \cdot s^{-1}$, stopband frequency of $7.5 \times 10^6 \pi \text{rad} \cdot s^{-1}$, stopband attenuation of 60dB, and passband ripple of 0.1dB.

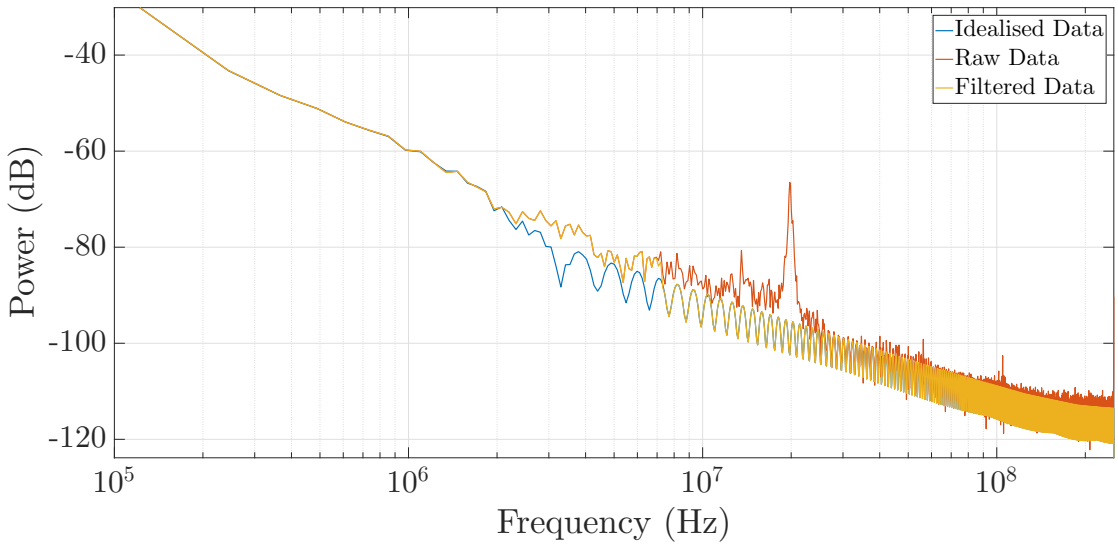

Figure 4.17: Power-frequency spectrum comparison of the raw data collected from the pre-amplifier, an idealised waveform calculated using equation (4.6), and the same raw data that has been digitally filtered.

The power-frequency spectrum was calculated for an idealised waveform and a real digitized waveform, taken from the data collected directly by the oscilloscope. The results calculated using Welch's Method [85] for both is shown in figure 4.17, which shows that there is a large frequency peak at approximately 2×10^7Hz.

A low pass filter was then designed in an attempt to reconcile the difference between the idealised and noisy real data. The frequency response of the low pass filter is shown in figure 4.16, and the resulting power-frequency spectrum of the filtered real data is shown in figure 4.17, calculated again by Welch's Method. After applying the filter, the power-frequency spectrum of the waveform is much closer to that of the idealised waveform and the large frequency peak has been suppressed. Figure 4.18 plots the analysed waveform with and without the application of digital filter which illustrates the noise suppressing effect that the filter has.

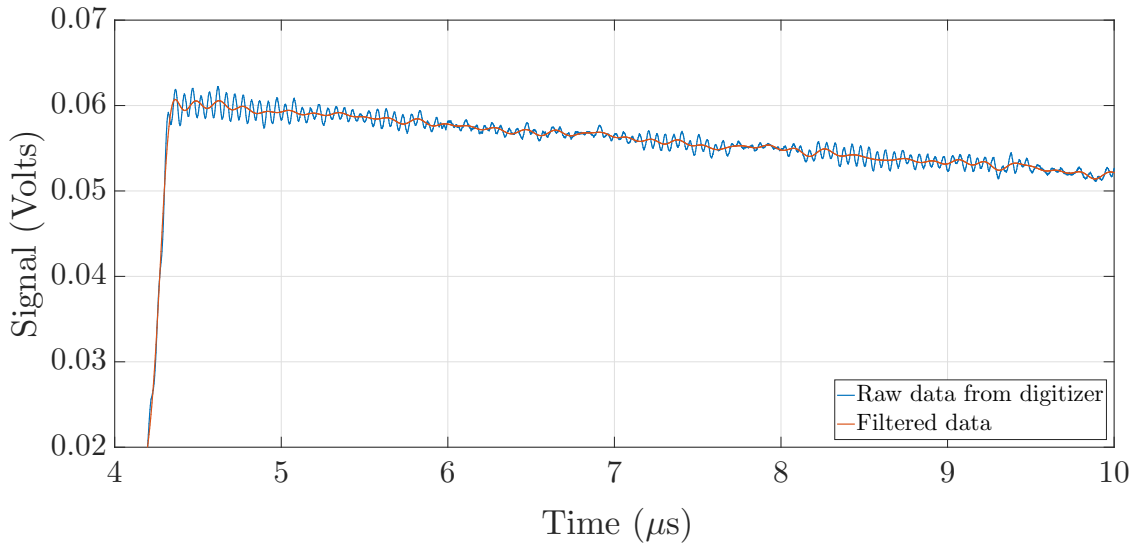

Figure 4.18: Direct comparison of the raw and digitally filtered pre-amplifier waveforms.

4.6.2 Digital Filtering Results

The digital filtering step was implemented as part of the data analysis programme and the curve fitting method was performed to the resulting digitally filtered waveforms. The results of typical fitting results are shown in figure 4.19, with coefficients and standard errors detailed in table 4.5, as reported by the fitting routine, ALGLIB.

The standard errors reported for each fitted parameter in table 4.5 are all lower than the typical standard errors reported from ALGLIB when fitting the raw waveform data di-

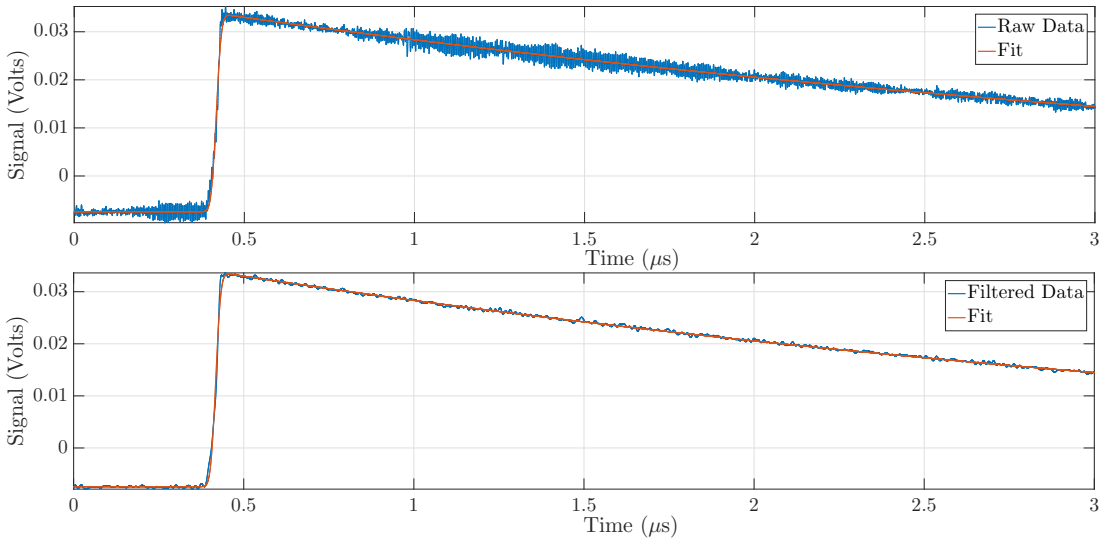

Figure 4.19: Comparison of the results of fitting the noisy raw data and the same data once the digital filter has been applied.

Parameter	Raw Data		Filtered Data	
	Value	Standard Error	Value	Standard Error
A	8.61×10^{-2}	2.08×10^{-4}	4.123×10^{-2}	1.01×10^{-5}
λ	$2.14 \times 10^{+4}$	$6.7 \times 10^{+2}$	$2.452827 \times 10^{+4}$	8.5×10^{-13}
σ	1.52×10^{-7}	2.5×10^{-9}	1.180×10^{-7}	3.5×10^{-10}
t_0	2.432042×10^{-3}	1.8×10^{-9}	4.1773×10^{-6}	2.4×10^{-10}
b	-1.368×10^{-2}	8.2×10^{-5}	-7.419×10^{-3}	6.9×10^{-6}

Table 4.5: Comparison of the typical results and standard error between fitting the raw pre-amplifier data and the digitally filtered data.

rectly, shown in table 4.4. The parameter λ, the exponential decay constant, is significantly more accurate after the digital filtering; the standard error in the digitally filtered data (8.5×10^{-13}) is 1×10^{15} times smaller than that of the raw data fitted directly (6.7×10^{2}). All the other parameters have improved in accuracy by one order of magnitude.

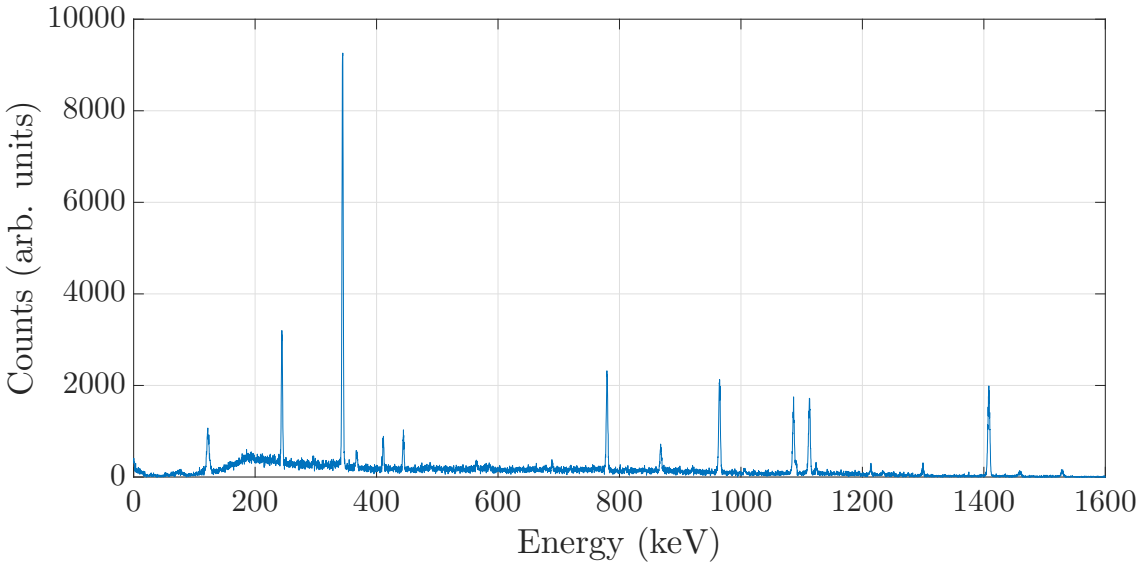

Figure 4.20: Spectrum of ^{152}Eu collected using the digitally filtered waveforms using the full digital experimental set-up.

A spectrum of ^{152}Eu was collected using the digital filtering method and the same radioactive check source used previously. The peak positions were calibrated to estimate the system resolution using the full-width at half-maximum for the chosen calibration peaks, as previously performed for the initial test and full digital method. The spectra is shown in figure 4.20 with the resolution of the peaks shown in comparison with the initial analogue resolution test in figure 4.21.

From the results of this testing, the resolution is still not as good as the initial analogue system, but the use of the digital filter has improved the resolution of the system compared to just directly fitting the pre-amplifier waveforms.

Of particular interest in the spectrum of ^{152}Eu from the digitally filtered data, the lowest energy peak (121.88keV) has a much larger FWHM than the other peaks, and does not follow the general trend of increasing FWHM with peak energy as shown in figure 4.21. This is attributed an experimental misconfiguration in the triggering of the oscilloscope for the data collected for this spectra. The 121.88keV peak is expected to have a much larger relative maximum as approximately 28 photons per 100 nuclear disintegrations will

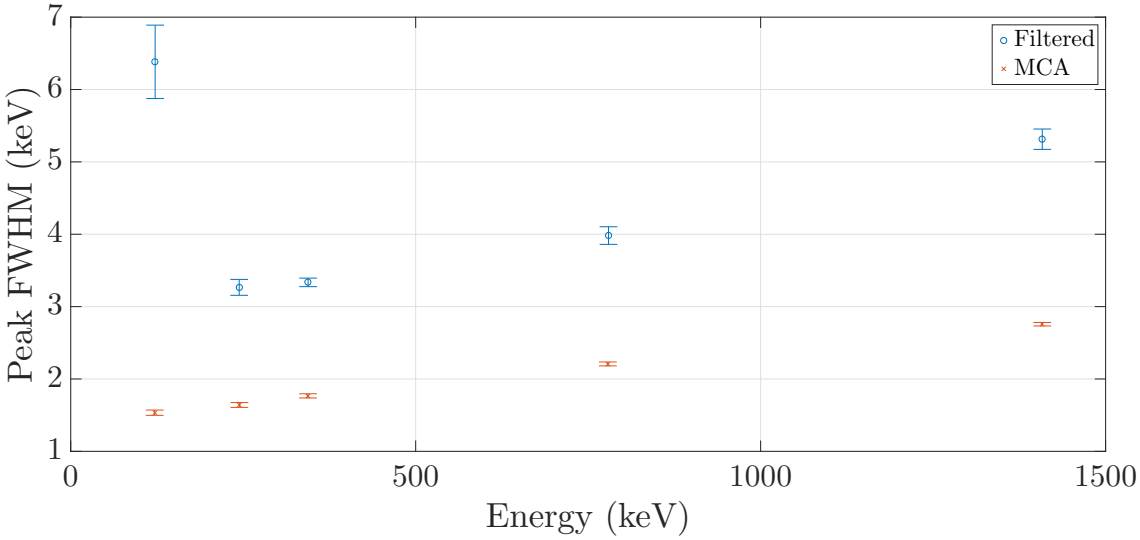

Figure 4.21: Effective resolution of digital filter compared to MCA data

result in a photon of this energy [74].

4.6.3 Conclusion

The digital filtering of the waveforms before the fitting routine is used has resulted in a large improvement in accuracy of the parameter λ and improved the fit quality for all the other fitted parameters. As previously mentioned in the conclusions of section 4.5, the variability in the parameter λ has large impact on the quality of fit in the other parameters. Using the digital filtering step before fitting the waveforms has resulted in this system giving a better energy resolution than the initial attempt in section 4.5.

Comparison between the spectrum of ^{152}Eu collected using the digital filtering step (shown in figure 4.20) and the spectrum ^{152}Eu collected without digital filtering (shown in figure 4.9) shows a much higher level of accuracy in the data that has been digitally filtered. There are more peaks visible, which should be present in the spectrum of of ^{152}Eu and the peak to noise ratio is much higher. Additionally, the discrimination of the fits based on R^2_{adj} and χ^2, detailed in sections 4.5.7 and 4.5.8 respectively, is not necessary as the artefacts from bad quality fitting are not present.

Figure 4.21 shows the difference in the effective resolution measured by the FWHM of the emission peaks of ^{152}Eu. Although the system does not have a comparable level of resolution to the initial benchmark measurement, therefore making the method unusable, one promising aspect of the digital filtering and digital data collection methods are the fact

that applying post processing does drastically improve the system quality. The resolution of the 244.86 keV peak in the spectrum of ^{152}Eu had a FWHM of approximately 11keV in the fully digital system (shown in figure 4.15), which was improved to 3.3keV by use of the digital filter applied before curve fitting.

4.7 Analogue DBAR System

Due to the poor resolution of the digital measurement, and despite the gains made using digital filtering, an analogue system was chosen as the experimental configuration to continue making DBAR measurements as it has the highest resolution.

4.7.1 Experimental Set-up

The analogue DBAR experiment was set up in a different configuration than the full digital configurations, due to the additional analogue components needed. The system was configured with the components illustrated in the block diagram in figure 4.22.

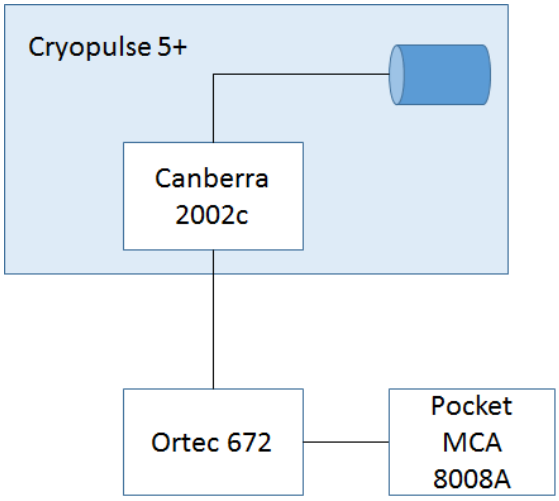

Figure 4.22: Block diagram of the analogue data collection stage of the DBAR experiment.

The equipment used in this analogue configuration are the HPGe detector crystal with built in cooling system and pre-amplifier, spectroscopic shaping amplifier, and multichannel analyser with associated computer software for data collection. The spectroscopic amplifier used was an Ortec model 672 NIM module, with shaping time set at 6μs. The multichannel analyser was a Pocket MCA model 8008A [72] which is connected to a computer and controlled using the ADMCA software [73].

The configuration of the experiment in this manner is similar to that of the initial measurement made to confirm the manufacturers calibration in section 4.4, therefore the initial calibration had already been completed. To further improve on the initial benchmark measurements additional radioactive sources of ^{60}Co and ^{133}Ba were used in addition to the ^{137}Cs and ^{152}Eu isotopes to more accurately calibrate the detector system. The measurements were made with a larger number of total counts using a longer shaping time on the spectroscopic amplifier for higher accuracy.

4.7.2 Detector Efficiency

To perform analysis on the data collected from experiments using the HPGe crystal detector system, it is important to understand the response of the crystal to different energy photons. Due to the energy dependence in efficiency, characterisation *in situ* must be performed as the response of the experiment will be unique to each HPGe crystal and the source-to-detector spacing.

Within the HPGe manual is a general efficiency curve for coaxial standard HPGe crytals as a function of energy, which has been reproduced in figure 4.1. This is a general case representation for an experimental source to detector distance of 2.5cm.

The 2.5cm efficiency curve is relatively impractical for this experiment (and perhaps many experimental set-ups) since there will be significantly more than 2.5cm spacing between the detector and source, due to the experimental equipment which is between the detector crystal and the location at which positrons will annihilate, including a vacuum chamber and solenoids. Therefore an efficiency calibration must be performed for this experiment.

To calibrate the detector efficiency the sources used were, as mentioned previously: ^{60}Co [86], ^{152}Eu [74], ^{133}Ba [87], and ^{137}Cs [86]. The absolute strength of the radioactive check sources were calibrated by the Department of Nuclear Physics at the Australian National University in 2011, and are detailed in table 4.6.

Using the known activity, relative probability for photon emission of a particular energy, and a spectrum collected using the experimental apparatus, the efficiency for a particular detector-source distance can be calculated. This follows the method outline by the work of Varnel *et al.* [88]. The results of this data can be found in tables A.1 and

Source Element	Half life (years)	Calibrated strength (μC)	Current strength (μC)	Reference
^{137}Cs	30.07	1.08	0.951(07)	[86]
^{60}Co	5.2714	1.03	0.498(7)	[86]
^{133}Ba	10.51	1.01	0.702(03)	[87]
^{152}Eu	13.537	0.829	0.625(04)	[74]

Table 4.6: Source information for performing detector efficiency calibration. Absolute strength calibration was performed at the Department of Nuclear Physics at the Australian National University in 2011.

A.2. The resulting data can then be manipulated into the form of a relative efficiency from the lowest efficiency energy, and the data fit with an exponential decay. Using this information, any data collected with the emission source at the corresponding distance allows recalibration of the spectra collected to get the true counts by combining the data with the calibration source data gives a function to calibrate spectra taken based on the efficiency of the crystal.

The form of the equation fitted to the normalised peak area as a function of photon emission energy and distance from detector endcap is given by equation (4.9), where ϵ is the efficiency, E is the independent variable, and A, B, and C are constants to be determined by fitting the data.

$$\epsilon(E, d) = A + B\exp(-CE) \tag{4.9}$$

The efficiency calibration was performed for the detector calibration at 15cm, which is the distance from the geometric centre of the sample chamber to the outside of the magnetic field coils, and therefore a more relevant efficiency calibration for the DBAR experiment.

Figure 4.23 shows the normalised peak areas as a function of photon emission energy for radioactive sources placed at 15cm from the detector endcap, and the fitted form of equation (4.9). The results of the fitting are detailed in equation (4.10).

$$\epsilon(E, d = 15\text{cm}) = 0.89537 + 4.26\exp\left(-\frac{E}{408.4147}\right) \tag{4.10}$$

Source Element	γ Energy (keV)	Photons per 100 disintegrations	Reference
^{60}Co	347.14	0.0075	[86]
	826.1	0.0076	
	1173.228	99.85	
	1332.492	99.9826	
^{152}Eu	121.7817	28.41	[74]
	244.6974	7.55	
	344.2785	26.59	
	367.7891	0.862	
	411.1165	2.238	
	443.965	2.8	
	778.9045	12.97	
	867.38	4.243	
	964.079	14.5	
	1112.076	13.41	
	1212.948	1.416	
	1299.142	1.633	
	1408.013	20.85	
^{133}Ba	53.1622	2.14	[87]
	79.6142	2.65	
	80.9979	32.9	
	276.3989	7.16	
	302.8508	18.34	
	356.0129	62.05	
	383.8485	8.94	
^{137}Cs	661.657	84.99	[86]

Table 4.7: Photon energies and decay probabilities per disintegration used for detector efficiency calibration.

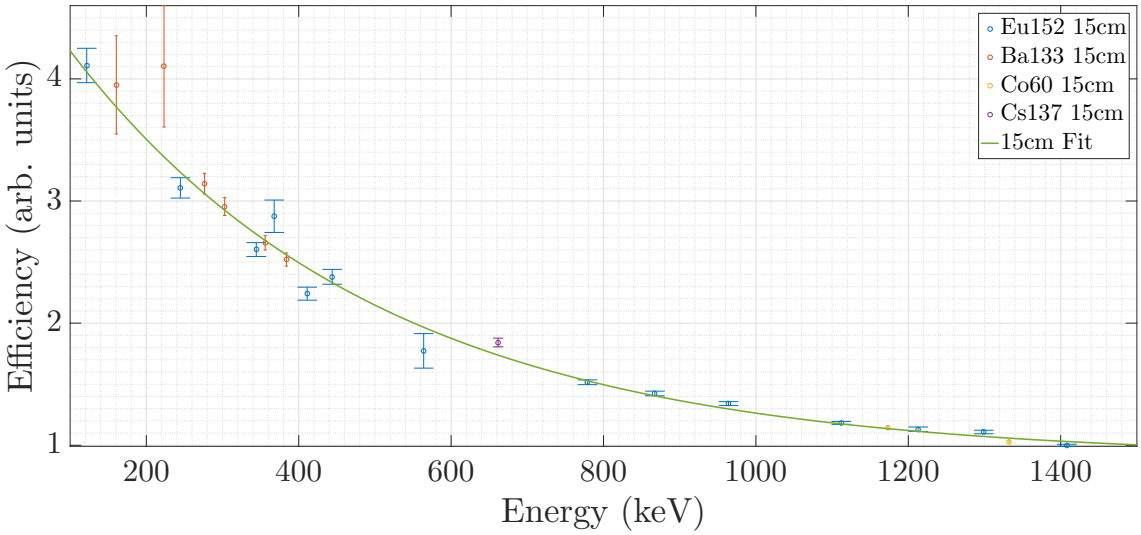

Figure 4.23: Peak area normalised to the last peak energy from radioactive sources placed 15cm from the detector endcap. The fitted equation is $\epsilon(E, d = 7\text{cm}) = 0.89537 + 4.26 \exp(-E/408.4147)$.

4.7.3 Analogue Resolution Measurement

The four calibration sources (^{60}Co, ^{152}Eu, ^{133}Ba, and ^{137}Cs) were used for the energy calibration of the detector, with the sources set at 7 and 15cm away from the detector endcap.

Again, as in section 4.4, the x-scale was calibrated using a quadratic polynomial function as described in equation 4.1, with the coefficients determined using the well-known energies of emission from the four radioactive isotopes.

The energy calibration was performed for the HPGe detector system with the radioactive sources placed at 15cm from the detector endcap. The results of the data collection are shown in figure 4.24.

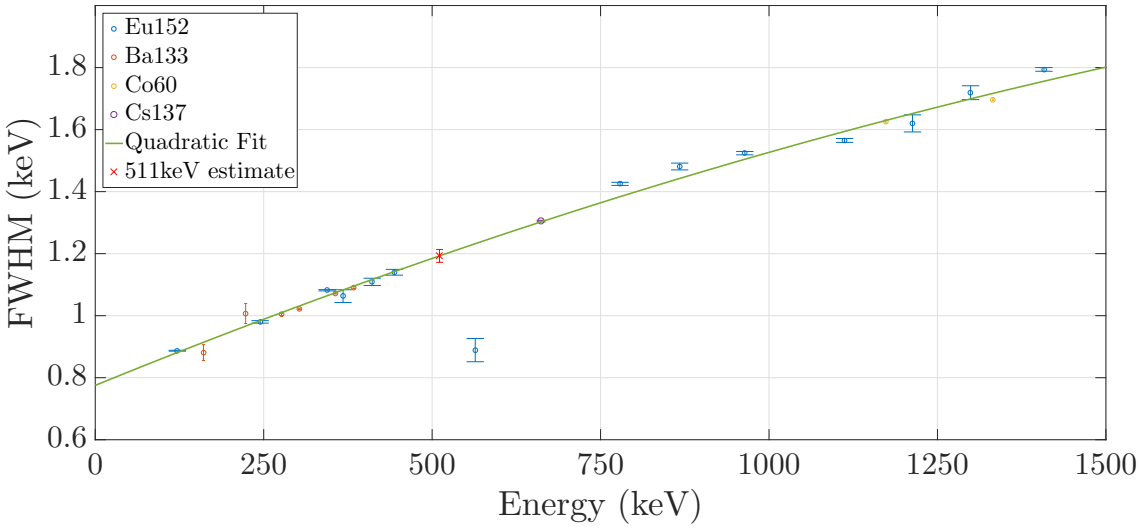

Figure 4.24: Detector resolution with the calibration sources placed 15cm from the detector endcap

The resulting fitting parameters for the radioactive sources placed at 15cm from the detector endcap are detailed in equation (4.11).

$$\mathrm{FWHM}(E, d = 15\mathrm{cm}) = 0.76977 + 8.8568 \times 10^{-4}x - 1.3441 \times 10^{-7}x^2 \qquad (4.11)$$

Using the energy calibration for the radioactive sources placed at 15cm from the detector endcap gives an estimated resolution at 511keV, the positron annihilation photopeak,

detailed in equation (4.12).

$$\mathrm{FWHM}(511keV, d = 15\mathrm{cm}) = 1.19 \pm 0.02\mathrm{keV} \tag{4.12}$$

4.7.4 Calibration Results

After fully calibrating the HPGe detector system, the efficiency adjustment can be re-applied to the spectra collected of the radioactive check sources.

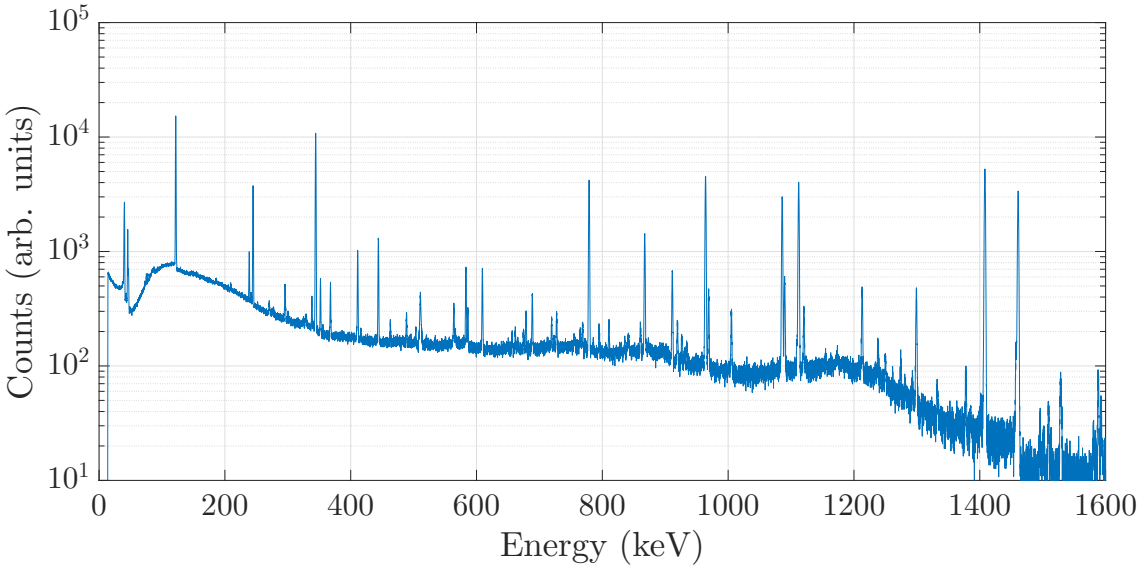

Figure 4.25: Final fully energy and efficiency adjusted spectrum of ^{152}Eu.

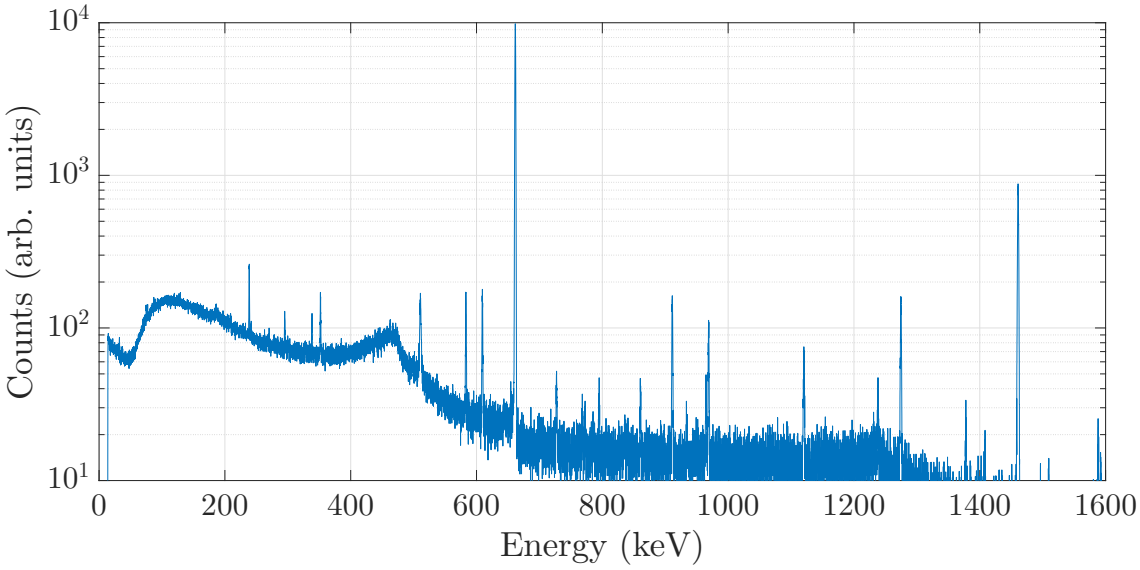

Figure 4.26: Final fully energy and efficiency adjusted spectrum of ^{137}Cs.

The spectrum from ^{137}Cs has many additional peaks than expected from the literature

[86] due to the natural abundance of radioisotopes present in the laboratory background. A measurement of the laboratory background was taken to investigate this and shows the daughter nuclei from decay chains from naturally abundant radioisotopes such as ^{235}U, and ^{238}U. Figure 4.27 shows the laboratory background radiation spectra with a few emission lines from particular isotopes peaks picked out and the emission energy. The relative intensity of the emission lines varies, with some such as ^{208}Tl producing a strong signal and others such as the ^{235}U 185.722keV peak are just visible above the background.

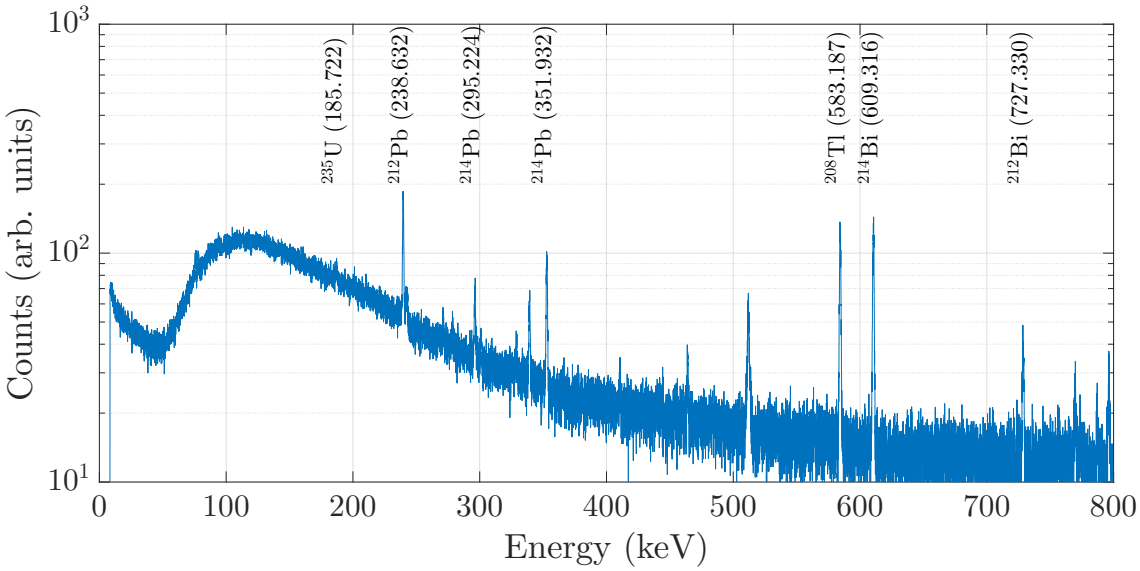

Figure 4.27: Investigation of laboratory background radiation environment. Interesting emission peaks are detailed with the isotope and the emission energy.

4.8 Spectrum Post-Processing

Fully calibrating the HPGe detector system results in true count spectrum which can be manipulated mathematically to aid in the analysis of DBAR measurements. The efficiency adjustment is necessary to obtain the true counts before any mathematical processing can be performed [61].

This section examines the mathematical post-processing of a DBAR spectra collected using the analogue detector set-up described and characterised in the previous section.

4.8.1 Experimental Set-up

To collect the DBAR data for this section, a substrate of crystalline aluminium was used as the target for the positron beam. The energy of the positron-target interaction was set to 15keV to maximise the number of positrons that annihilate in the bulk of the target, far from the surface.

The positron beam was configured for DBAR measurements as described in section 4.2, with the target sample in the middle of the vacuum chamber approximately 15cm from the HPGe detector endcap.

The DBAR spectrum was allowed to accumulate to 16×10^6 counts in the 511keV photopeak.

4.8.2 Post-Processing Method

As there is only one HPGe crystal, the apparatus is set-up in a single detector configuration and therefore the advantages of conservation of energy cannot be used to minimise the background as in coincidence detection systems. In DBAR measurements using a single detector configuration there is a background on both sides of the 511keV peak, both high and low energy. The high energy background comes from the natural radioactivity in the laboratory environment. The low energy background comes from 3-photon annihilation events from the positron beam, and incomplete charge collection in the detector. To mitigate these effects, work has been done by Haaks *et al.* to mathematically correct these effects in DBAR spectra [61].

To reduce the background in the DBAR measurements, the 511keV photopeak from positron annihilation was fitted in incremental stages based on the work in reference [61]. Several functions are used in the fitting, which are defined in equations (4.13), (4.14), (4.15), and (4.16), and the associated parameters are explained in detail below, with E as the independent variable.

$$u = \frac{2\sqrt{\ln 2}(E - E_0)}{\sigma} \tag{4.13}$$

$$G(E) = A_G e^{-u^2} \tag{4.14}$$

$$S(E) = \frac{1}{2} A_S \left(1 - \mathrm{erf}\left(u\right)\right) \tag{4.15}$$

Which are combined to fit the whole function:

$$P(E) = G(E) + S(E) + b \tag{4.16}$$

To perform the actual fitting first only the function $G(E)$ is used, which finds the parameters σ, E_0 and A_G, the standard deviation of the Gaussian, the peak centre, and the Gaussian amplitude, respectively.

After the function $G(E)$ has been successfully fit to the DBAR spectra and the parameters σ and E_0 have been found, the full function $P(E)$ is fitted. The initial guesses of the parameters supplied are the previously found σ, E_0 and A_G. The function $S(E)$ takes the form of a "rounded" step function with parameter A_S as the amplitude of the step.

All curve fitting was performed in MATLAB [78] using the packages for non-linear least-squares regression and fit result statistics reporting [89]. An example of each fitting stage and the resulting background subtracted data are illustrated in figure 4.28.

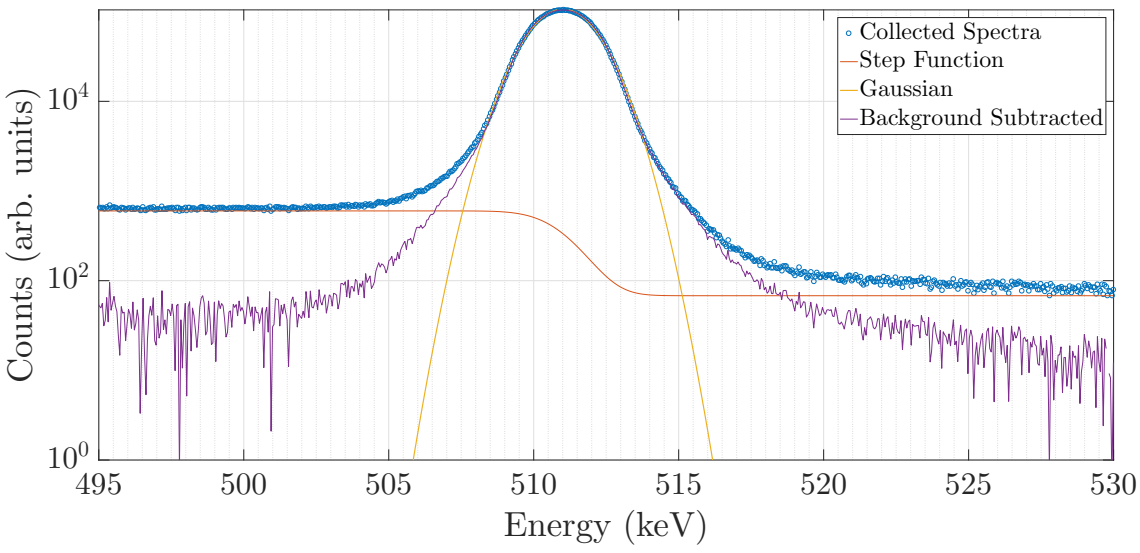

Figure 4.28: Example of the composite functions in the background post-processing function applied to the DBAR spectra of crystalline aluminium.

4.8.3 Post-Processing Results

Using the characterised analogue detector system a DBAR measurement was made of a sample of crystalline aluminium, and results of the post-processing of the DBAR spectra are shown in figure 4.28. The results show a broader curve than the resolution of the system would expect, which can be attributed to the Doppler broadening of the detected annihilation photons. Post processing was applied to the 511keV peak in an attempt to reduce the impact of the background with the single crystal detector arrangement, which successfully reduced the spectrum background.

The linear background parameter, b, is fitted as part of the function $P(E)$, however through adjusting the value for b and performing analysis on the peak it has been found that under estimating the linear background and overestimating the amplitude of the step function leads to qualitatively better results, due to the gradual slope in the high energy region of the spectra. Using a more precise background subtraction gives results with negative data which make comparative analysis more difficult, and a loss of information in the high momentum broadening fraction of the spectra, as the counts in this region of the spectra are relatively low.

Although the filtering steps taken result in perceived better data quality in the 511keV photopeak spectra, the definition of the fitted linear background parameter, b, seemed arbitrary, and qualitatively better fitting was achieved by underestimating this parameter. As shown in this section, allowing some remaining background by underestimating b enables better quantitative analysis than over fitted background subtraction and the final background-subtracted DBAR spectra can be used to make more precise W parameter spectra measurements.

4.9 Conclusion

There were two unsuccessful attempts at implementing a fully digital data collection system for the DBAR measurement being added to the positron materials beamline. The first attempt employed curve fitting on the raw waveforms digitized from the pre-amplifier on the HPGe detector and the second method augmented the first by digitally filtering the collected waveforms.

Directly fitting the waveforms digitized from the pre-amplifier was made inaccurate by the large range of values that the exponential decay parameter could take that satisfied the fitting constraints, within the noise of the digitized signal. The residual was easily optimised with the exponential decay parameter which dominated the fitting algorithm at the expense of the required amplitude parameter.

Using a digital filter to suppress some of the noise in the digitized waveforms significantly improved the effective resolution of the digital system, allowing for better quality fitting of the underlying signal and hence better resolution in the data acquisition system. Despite the fact that the low-pass digital filter method results in significantly better resolution, the initial analogue benchmark was still much better. Although using digital filters resulted in a still unusable system for DBAR experiments, the fact that using post processing resulted in a marked improvement shows that the philosophy behind digital measurements is valid: using post-processing of data after the fact results in immediate gains in data quality.

In the implementation of the analogue measurement configuration the resolution of the system was significantly improved in comparison to the initial resolution benchmark and the manufacturer's calibration. The final estimated resolution at 511keV is 1.19 ± 0.02keV, which is somewhat higher resolution than the manufacturer's calibration.

Full measurements, adjusted for detector efficiency, were made of the radioactive sources used to calibrate the detector system, shown in figures 4.25 and 4.26. A measurement of the radiation background present in the laboratory was made and the radioactive decay of elements present identified, shown in figure 4.27.

For future work in a digital measurement there are different approaches to digital measurements that could be investigated. One avenue of approach is using peak fitting with a digital finite impulse response filter (FIR) that will approximate something like a spectroscopic shaping amplifier, and is what some positron physics groups use to analyse pre-amplifier data [90, 91]. Various FIR filters can be created and fine tuned to represent different types of spectroscopic shaping amplifiers, with the benefit of allowing any timing constants, including those not possible with circuit based amplifiers. The problem with using further filtering methods or FIR type mappings are that they do not directly deal with the issue of noisy signals, however it should be possible to directly get the result of

any analogue pulse shaping using a digital method. This brings the uncertainty directly to the digitizer quality — if the digitization is inaccurate then any associated uncertainties will be passed through to the digital filter or FIR shaping, and the resolution of the system will only improve to a degree as shown in the results presented here as shown in section 4.6, when the digital filter was applied.

Chapter 5

Elemental Specificity using DBAR

In this chapter, the momentum distribution of elements and materials are investigated using Doppler broadening of annihilation radiation. This investigation presents an extended characterisation of the experimental apparatus and examines the limits of the sensitivity of the implementation of the measurement technique.

Traditionally, single detector systems are hindered in examining the elemental specificity of DBAR spectra due to the high background which masks the fraction of positrons that annihilate with high momentum electrons. Using the mathematical corrections presented in the work by Haaks *et al.* [61] and covered in detail in section 4.8, evidence is presented that shows that DBAR spectra that are corrected in this way can reveal more elemental specificity, the distinguishing features of the corrected spectra differ significantly to higher resolution coincidence systems.

By examining the distribution of photon energies around the 511keV for high quality pristine samples, the electron momentum distribution can be compared between elements from related groups in the periodic table, and materials which share similar characteristics. We expect to observe different peak energy distributions which are dependent on the filling of higher electronic shells. Each element or material should exhibit a unique spectrum, as the kinetic energy of the electron in the annihilating pair will depend not only on the shell configuration, but also the spatial distribution which is influenced by proton number.

5.1 Method

5.1.1 Sample Measurement

To collect the data for each sample in this study the DBAR system on the positron materials beamline at ANU was used, as described in section 4.2.

The number of counts in each 511keV peak is approximately 80% that of the total number of counts in the entire spectrum. To ensure a statistically significant number of counts in the peak balanced with a reasonable experimental run time, each spectrum was allowed to accumulate to 10×10^6 counts for each sample. For the aluminium sample 16×10^6 counts were collected as it was to be the reference material. Accumulating this large number of counts ensures that a suitably large number of counts are collected in the high momentum broadening regions of the DBAR spectrum. The high momentum broadening region is of importance in these measurements as the differences in elements are to be found through comparison of the momentum broadening due to positron annihilation with core-shell electrons, which results in high momentum broadening. Further information on this is covered in section 2.5.

The positron-material interaction energy was set to 15keV using the high voltage assembly (described in section 3.2.3) to ensure that the positrons are implanted far from the surface. The deeper positron implantation reduces the impact of positron-surface interaction and significantly reduces the likelihood that positrons will diffuse out of the sample. Even in dense elemental samples, for example lead, the positron diffusion length can be large enough that positrons can diffuse significant distances and insufficient implantation energies will allow positrons to diffuse back to the surface.

5.1.2 Treatment of data

To analyse and compare the data collected for each sample the data was processed to correct for the detector efficiency and remove the background, and finally area normalised to unity. This method is the same as explained in section 4.8.

For improved legibility and comparison to the work in reference [54], the various spectra were first smoothed and then taken in ratio to a measured DBAR spectrum of a defect-free crystalline aluminium sample. The aluminium sample is a single crystal which has been annealed and subsequently stored in vacuum in the positron laboratory, at a constant 23.5°C . The smoothing algorithm used was a 23 point "boxcar" moving average. The choice of 23 points is such that the smoothing window is comparable to the resolution of the system, which is approximately 1.2keV. The characterisation of the experiment and calculation of the resolution is detailed in chapter 4 and in figure 4.24. The uncertainty

in the data taken in ratio to aluminium increases with deviation from 511keV, which is expected as the number of counts in the original spectrum decreases, and the uncertainty in the original DBAR spectrum is proportional to the square root of the counts. For this reason, and as illustrated in figure 5.1, the data at high momentum broadening becomes difficult to read with several spectra present on the same graph. Therefore the smoothed ratio curves have not been plotted with uncertainties.

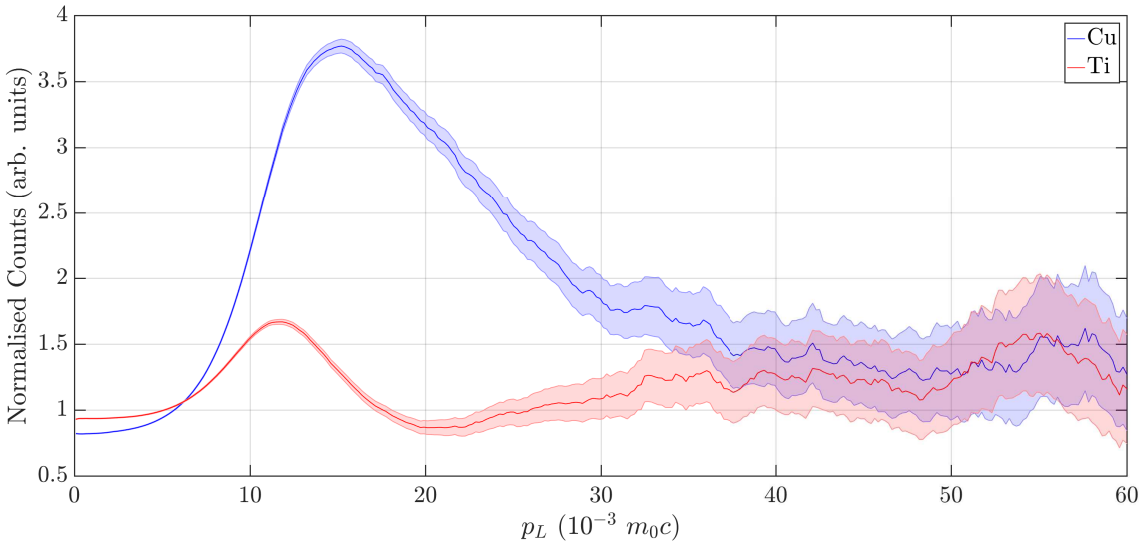

Figure 5.1: Examination of uncertainty in ratio measurements. Copper and titanium are included as examples to show that the uncertainty increases with momentum broadening, with 1σ uncertainty shown in the transparent path above and below the solid main line.

The data was treated in the manner described to provide data in a format which makes comparison between similar elemental samples as straightforward as possible, as well as to compare these measurements to a body of work which covers a large range of elements from across the periodic table and theoretical calculations [54]. To further aid comparison, the spectrum taken in ratio to aluminium is presented in momentum units, p_L.

To compare data from each measured sample it is useful to refer to the elements in terms of electronic shell structure, as the DBAR measurement gives information on the change in electron momentum. The filling order of the electronic shells of the elements proceeds as (for elements up to Radon), in electron configuration notation:

$$1s^2 2s^2 2p^6 3s^2 3p^6 4s^2 3d^{10} 4p^6 5s^2 4d^{10} 5p^6 6s^2 4f^{14} 5d^{10} 6p^6 \tag{5.1}$$

In general the outer most shells will give rise to the observed changes in the DBAR

spectra, so the shorthand notation of the electron configuration is used. For example the electron configuration [Ar] is equivalent to $1s^2 2s^2 2p^6 3s^2 3p^6$, and so for titanium it is the electronic structure of argon plus several more electrons. This is written as [Ar] $4s^2 3d^2$. Using notation in this way immediately gives easy access to the required information rather than verbosely re-stating less useful information each time.

Notably in equation (5.1) the d and f shells are less energetically favourable than the s shells in the level above them, and so fill after the s. This results in elements with partially or wholly filled d shells having large momentum broadening due to the spatially extended electronic shells. The materials investigated by DBAR were separated into groups of materials sharing common properties, so that the comparison is straightforward and the changes specific to the group can be isolated. These groups were transition metals (row 4, group 6, group 11), basic metals, semiconductors, and organic materials.

5.1.3 Details of Measured Materials

The material samples used for the elemental specificity measurements were of the highest available quality with best attempts made to ensure they are defect free. The elemental metals measured are from samples that are used as reference measurement in other experiments at the ANU, and as such are single crystal sample that are regularly annealed in a manner appropriate to the material. The organic materials measured are pristine as manufactured, and highest quality samples were obtained from the manufacturers.

To ensure that the DBAR measurements made of the materials samples were of the bulk and minimise interaction from the surface environment, relevant information from positron studies was collected.

Shown in table 5.1 is the positron diffusion length L_+, and the density of each material. From the density the mean implantation depth of 15keV positrons can be computed and following from this, the mean number of positron diffusion lengths from the surface has been calculated. For each material over the implantation depth should be sufficient to be far away from the surface such that contributions from surface effects are negligible. The tungsten sample mean implantation is approximately 1.17 diffusion lengths from the surface which implies that there is a higher likelihood that positrons could diffuse to the surface before annihilating. The diffusion length in tungsten was calculated using the up-

Sample Material	Density (g/cm^3)	Mean Penetration Depth (nm)	L_+ (nm)	No. L_+ from surface	Reference
Pb	11.34	268.7	26.87	14.93	[92]
Cu	8.92	341.5	34.15	2.44	[93]
In	7.31	461.8	46.18	18.85	[92]
Fe	7.874	386.9			
Mo	10.28	296.4	29.64	2.69	[93]
Si	2.33	1307.5	130.75	18.51	[94]
Ti	4.507	676.0			
Al	2.7	1128.3	112.83	6.92	[93]
Ni	8.908	342.0	34.20	3.11	[95]
Mylar	1.38	2207.6			
Kapton	1.42	2145.4	5.43	395.1	[96]
PMMA	1.18	2581.8			
PTFE	2.2	1384.8			
Au	8.92	341.5	34.15	3.42	[97]
W	19.25	158.3	15.83	1.17	[98]
Ag	10.49	290.4	29.04	2.64	[93]
Ge	5.323	572.3	57.23	8.25	[94]

Table 5.1: Elements investigated by DBAR and selected relevant properties. The positron diffusion length L_+ has been collected from the references listed, where available in the literature. The mean positron implantation depth for 15keV positrons (calculated by equation (2.5)) is converted to the corresponding number of diffusion lengths.

per limit for the diffusion constant D_+ in reference [98] which makes 1.17 diffusion lengths significantly far enough from the surface to minimise the effects of positron diffusion.

5.2 Basic Metals

In these DBAR measurements three basic metals are compared: aluminium, indium, and lead.

These elements are from the basic metals grouping in the periodic table and the expectation in the DBAR spectra is to see an increased broadening in the 511keV spectrum with increasing atomic number, due to filling of higher level electron shells with increasing Z. Figure 5.2 and the inset figure show that there is a clear broadening of the spectra shape, with lead significantly wider than indium, and indium significantly wider than aluminium. This is made clearer in figure 5.3, showing the wider broadening of the heavier lead than indium.

Element	Density (g/cm^3)	Atomic Number	Electron configuration
Al	2.70	13	[Ne] $3s^2 3p^1$
In	7.31	49	[Kr] $5s^2 4d^{10} 5p^1$
Pb	11.35	82	[Xe] $6s^2 4f^{14} 5d^{10} 6p^2$

Table 5.2: Properties of selected basic metals

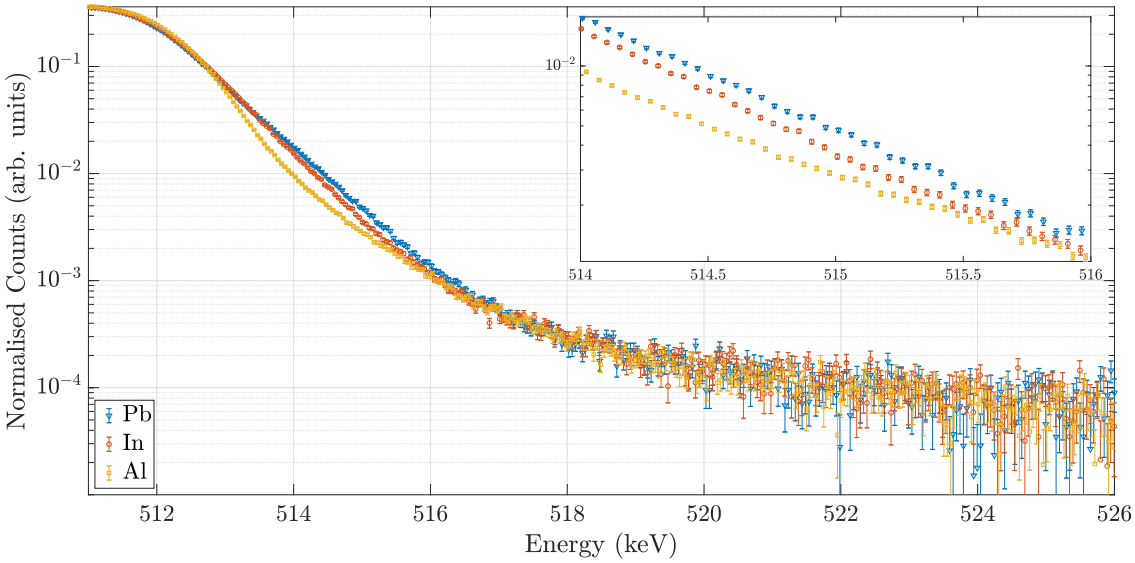

Figure 5.2: Momentum broadening spectrum of basic metals. Aluminium, indium, and lead are compared.

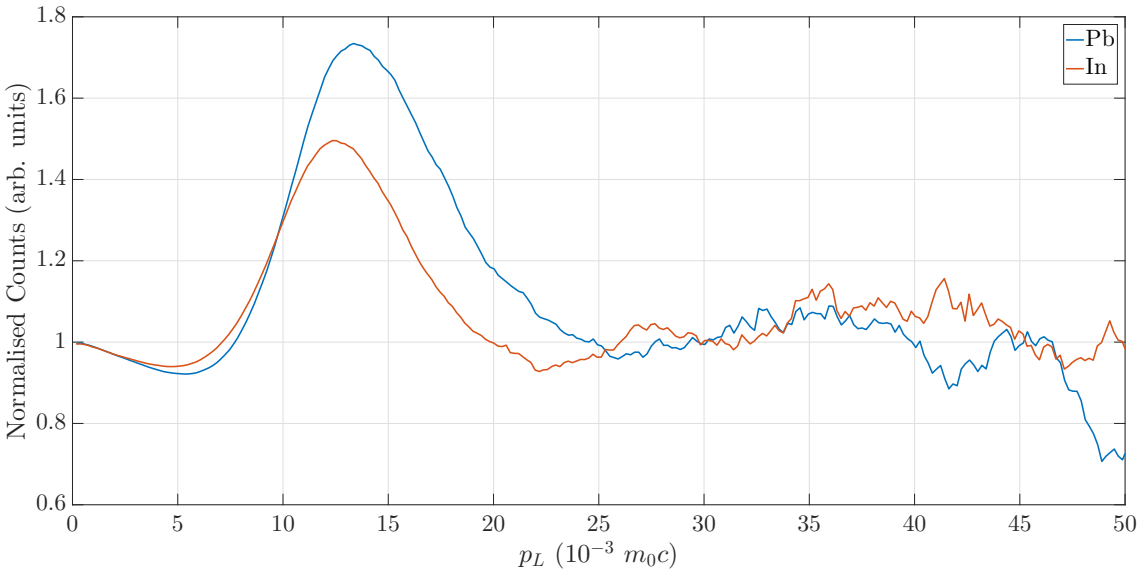

Figure 5.3: Momentum broadening spectrum of the basic metals indium and lead, in ratio to aluminium.

5.3 Transition Metals

In this section, transition metals are investigated. These can be separated into three groups from the periodic table for comparison: row 4, group 6, and group 11.

Element	Density (g/cm^3)	Atomic Number	Electron configuration
Ti	4.54	22	[Ar] $4s^2 3d^2$
Fe	7.87	26	[Ar] $4s^2 3d^6$
Ni	8.91	28	[Ar] $4s^2 3d^8$
Cu	8.96	29	[Ar] $4s^1 3d^{10}$
Mo	10.28	42	[Kr] $4d^5 5s^1$
Ag	10.49	47	[Kr] $4d^{10} 5s^1$
W	19.25	74	[Xe] $4f^{14} 5d^4 6s^2$
Au	8.92	79	[Xe] $4f^{14} 5d^{10} 6s^1$

Table 5.3: Properties of selected transition metals

5.3.1 Row 4 Transition Metals

All of the row 4 transition metals have full 1^{st} and 2^{nd} shells ($1s^2 2s^2 2p^6$) as well as full $3s$ and $3p$ shells. The momentum broadening is expected to increase with increasing atomic number, which we attribute to the filling of the 3D shell. This is shown in figure 5.4.

Of interest is the similarity between nickel and iron in figure 5.5, when compared to copper. There is a much higher broadening in copper than nickel, although there is only one electron difference. The significance in this is that the configuration of the electrons shifts from a full $4s$ shell in nickel and iron, to a full $3d$ shell in copper with an incomplete $4s$ shell.

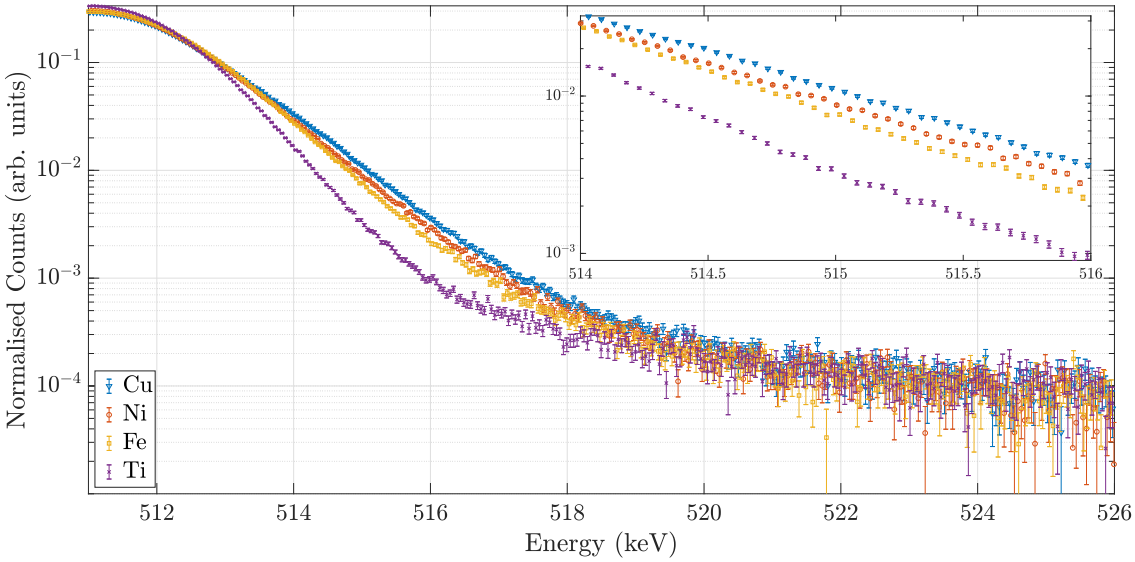

Figure 5.4: Momentum broadening spectrum of row 4 transition metals. Copper, nickel, iron, and titanium are compared.

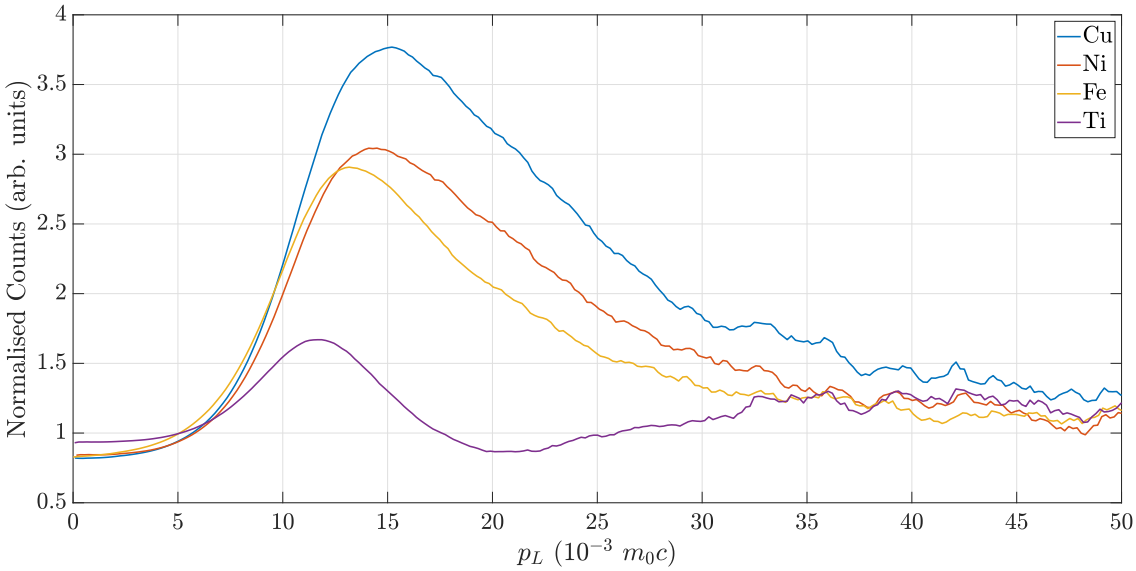

Figure 5.5: Momentum broadening spectrum of row 4 transition metals copper, nickel, iron, and titanium, in ratio to aluminium.

5.3.2 Group 6 Transition Metals

The momentum broadening observed in the DBAR spectra in figure 5.7 increases with atomic number. The line shape for tungsten in ratio to aluminium (shown in figure 5.7) is quite different to the other transition metals in section 5.3.1 and 5.3.3, apart from gold, which also appears unique.

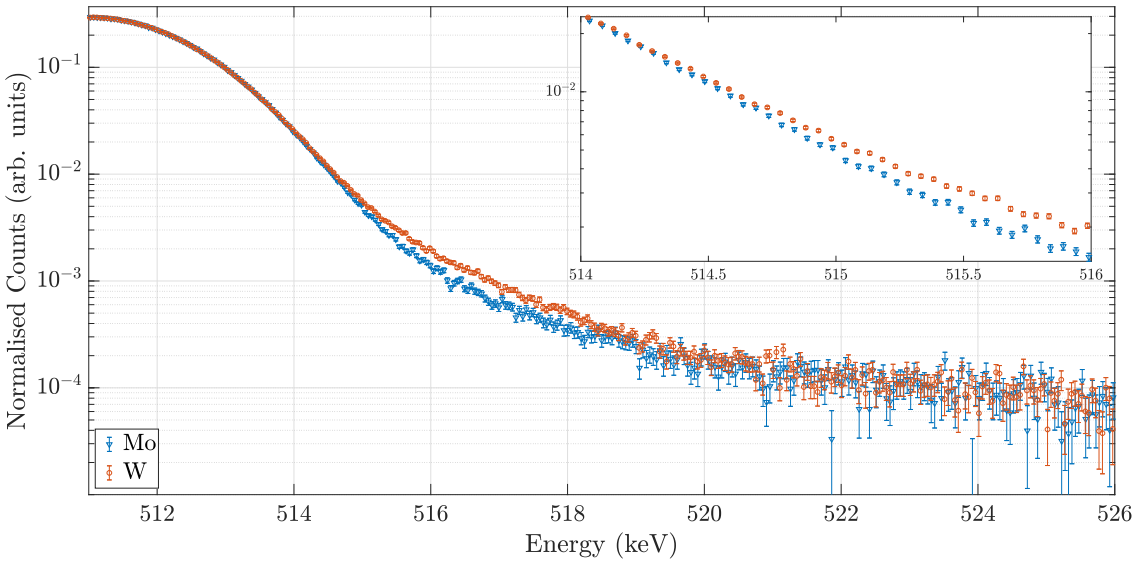

Figure 5.6: Momentum broadening spectrum of group 6 transition metals. Molybdenum and tungsten are compared.

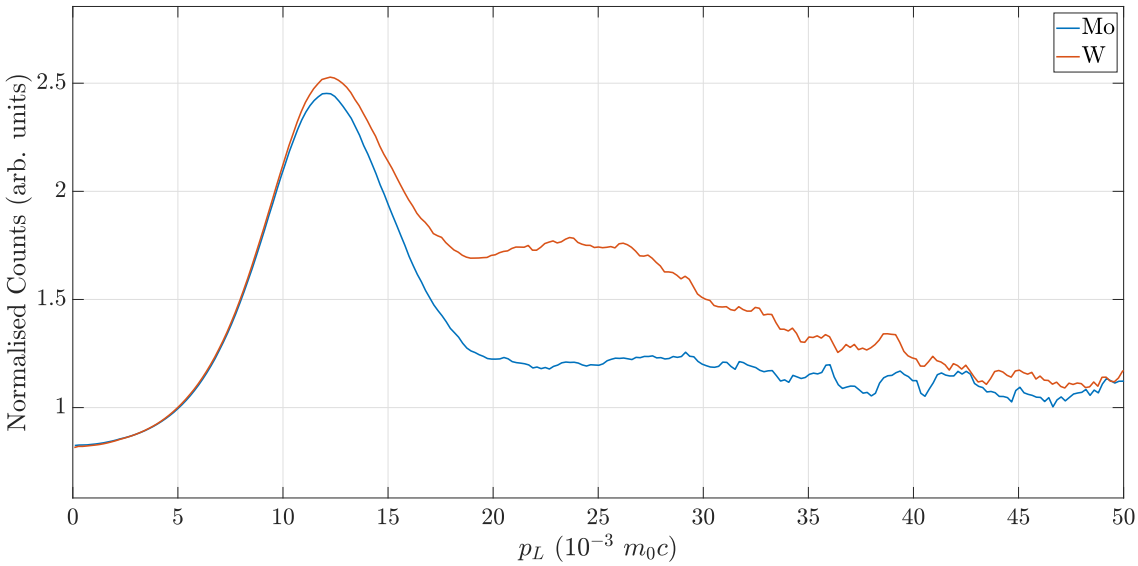

Figure 5.7: Momentum broadening spectrum of group 6 transition metals, molybdenum and tungsten, in ratio to aluminium.

5.3.3 Group 11 Transition Metals

The comparison of the broadening of the DBAR curves in figures 5.8 and 5.9 show that the broadening of the group 11 elements seems to proceed in reverse to the expected increased broadening with increasing electronic shell filling.

Additionally, the copper and silver ratio curves in figure 5.9 show similar line shapes, but the gold ratio curve is significantly different.

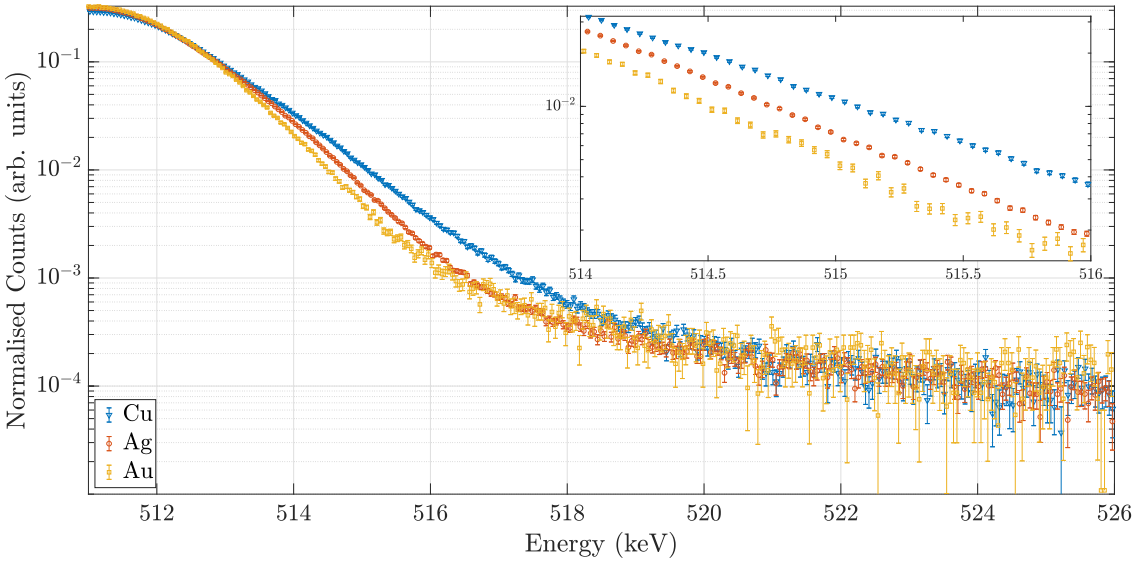

Figure 5.8: Momentum broadening spectrum of group 11 transition metals. Copper, silver and gold are compared.

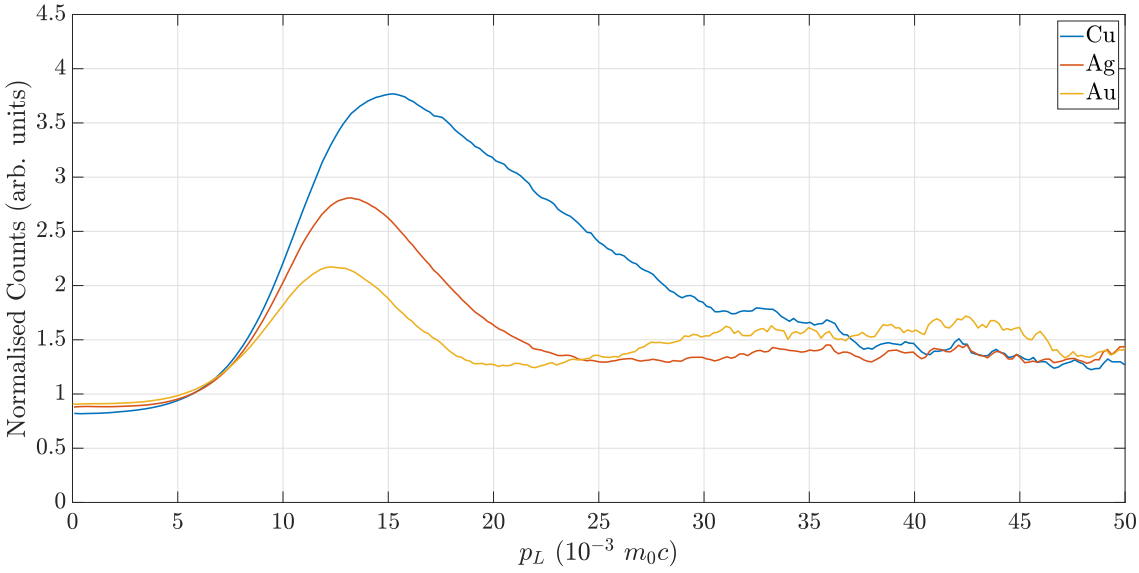

Figure 5.9: Momentum broadening spectrum of group 11 transition metals copper, silver, and gold, in ratio to aluminium.

5.4 Semiconductors

Two available semiconductor materials were measured, silicon and germanium.

Element	Density (g/cm^3)	Atomic Number	Electron configuration
Al	2.70	13	[Ne] $3s^2 3p^1$
Si	2.33	14	[Ne] $3s^2 3p^2$
Ge	5.32	32	[Ar] $4s^2 3d^{10} 4p^2$

Table 5.4: Properties of selected semiconductors

Aluminium and silicon have very similar electron configurations, and only differ in one additional electron in a low momentum shell ($3p^1 \rightarrow 3p^2$), meaning that their DBAR spectra should look very similar. In figure 5.10, the differences between the two spectra seem very small, but in the ratio curve to aluminium in figure 5.11, the differences are more obvious. These differences in spectrum shape occur from the differences in the crystal lattice, which affects the electron distribution around each nuclei.

Germanium is significantly more broadened, as would be expected given it is a row below both aluminium and silicon, therefore containing more high momentum electrons, including a full d shell.

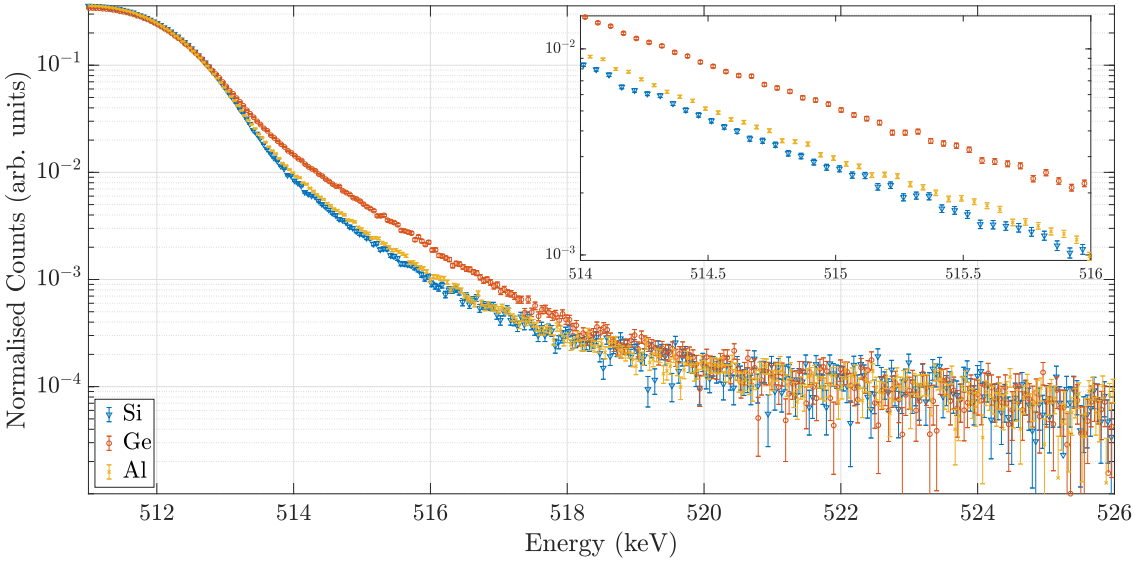

Figure 5.10: Momentum broadening spectrum of semiconductor elements. Silicon and germanium are compared, with aluminium included for reference.

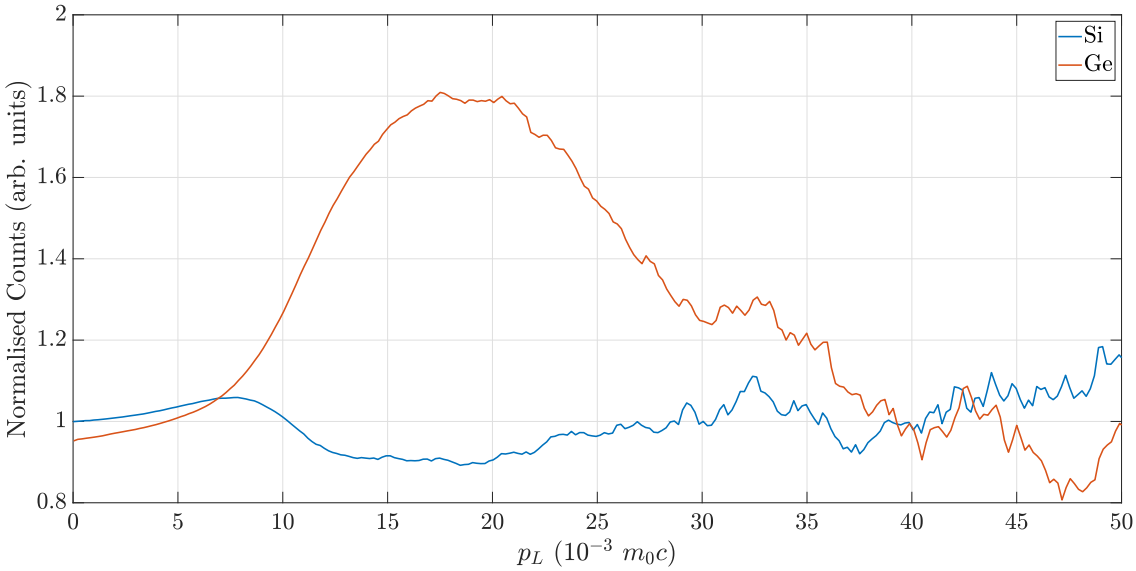

Figure 5.11: Momentum broadening spectrum of semiconductor elements silicon and germanium, in ratio to aluminium.

5.5 Organic Materials

Examining the high momentum fraction in the DBAR spectra for organic materials is different to the interpretation of the same work for elemental samples. The significantly different spectrum shapes for the organic materials arise due to the fact that they are complex molecular substances formed in chains of repeated monomer groups. The polymer chains within these organic materials can be arranged haphazardly in some regions, or with relatively high structure in other areas. Unlike many of the single element samples investigated in the previous sections, the elements that make up the organic materials presented contain relatively light elements and therefore the observed Doppler broadening of the detected annihilation radiation is likely to be significantly smaller.

Material	Chemical Formula	Average Density (g/cm^3)	Total Z per monomer	Average Z per monomer
PTFE	C_2F_4	2.2	48	8
Kapton	$C_{22}H_{10}N_2O_5$	1.42	196	5.02
Mylar	$C_{10}H_8O_4$	1.38	100	4.54
PMMA	$C_5O_2H_8$	1.18	54	3.6

Table 5.5: Properties of selected organic materials.

Positrons annihilating within a polymer material can annihilate in a wide variety of places, each with different characteristics. Similar to annihilation at grain boundaries in polycrystalline metals, annihilation can take place between polymer chains. Due to the significant length of some polymer chains, annihilation can also take place at different locations along the monomer, with different chemical environments. For example, Kapton contains 3 benzene rings as well as various other functional groups including products of oxygen and nitrogen, forming a large molecule.

Due to the much higher complexity in the chemical environment when compared to elemental samples, it is harder to predict what might occur in the DBAR spectra. To attempt some reconciliation with the idea of increasing broadening with electron number and configuration, included in table 5.5 is a column of the averaged atomic number per monomer unit. This is the total atomic number in the monomer divided by the number of atoms in the monomer. Although the broadening in figure 5.12 and 5.13 increases with the density, density does not directly correlate to the chemical environment of the organic

materials. For this reason, looking at average atomic number per monomer is perhaps a better quantity for comparison of organic materials.

From average atomic number per monomer column in table 5.5 the material with the highest Z_{avg}/monomer is PTFE, which makes makes qualitative sense as the PTFE monomer is made of only 6 atoms, 4 of which are fluorine, and fluorine is considerably more electronegative than carbon. Correspondingly, the broadening of the annihilation peak for PTFE is the largest, as can be seen in figure 5.12.

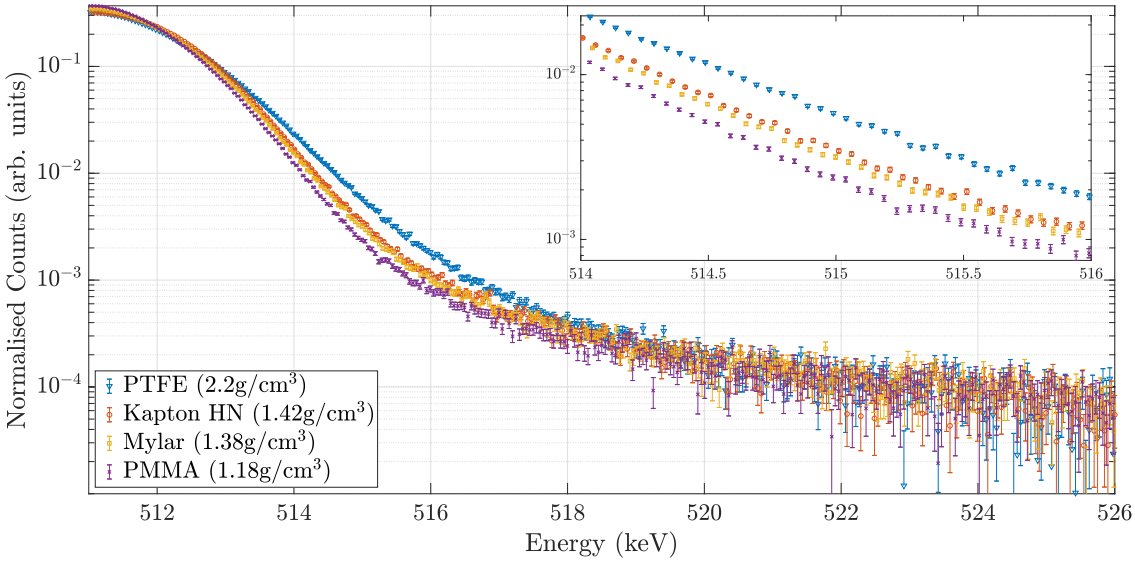

Figure 5.12: Momentum broadening spectrum of organic materials. PTFE, Kapton, Mylar, and PMMA are compared, with the material density included for reference.

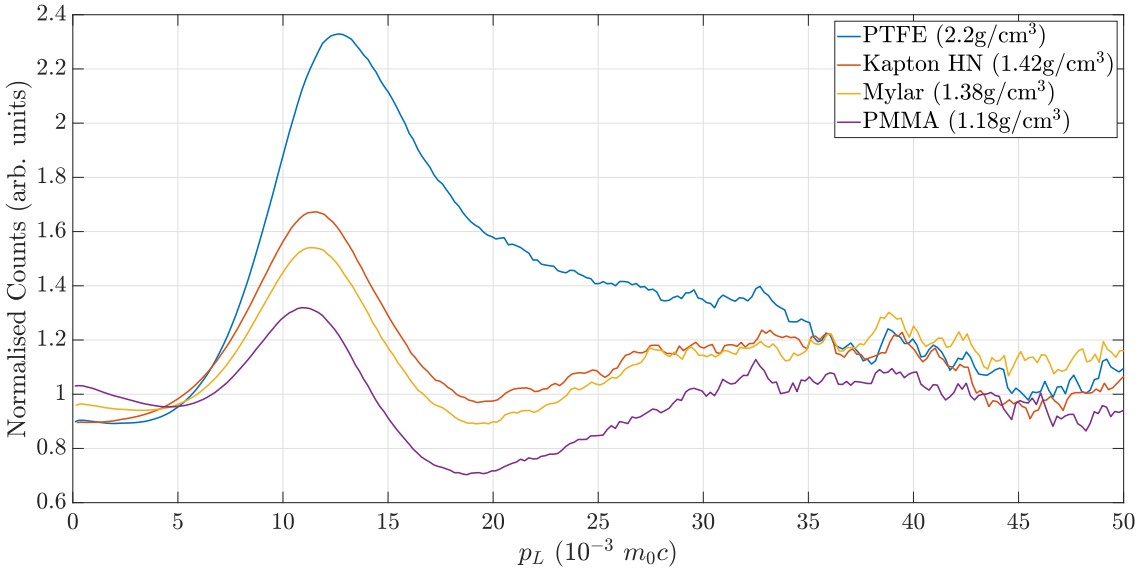

Figure 5.13: Momentum broadening spectrum of organic materials in ratio to aluminium. PTFE, Kapton, Mylar, and PMMA are compared, with the material density included for reference.

5.6 Discussion

The measurements taken in this chapter attempt to look at the high momentum fraction in the DBAR spectra as compared to the work in other references. This type of comparison is an excellent test to get quantitative data on the ability to resolve changes in the high momentum fraction, and understand the shape of ratio curves after the mathematical post-processing of data.

The samples were measured using positrons implanted at 15keV to minimise any surface interaction between the positrons and the sample material. Additional measurements could be made at various positron implantation energies to build up a depth profile of the material. The depth profile measurement would investigate the effects of surface interaction in the momentum broadening curves measured. The derived S parameter information from the depth profile measurements and a measurement of the positronium fraction could be used to experimentally determine the positron diffusion length [99].

Several of the elements that were measured by Asoka-Kumar *et al.* [54] were measured in this experiment and are shown in figure 5.15, in ratio to the measured sample of crystalline aluminium. Figure 4 of the previous work has been reproduced here in figure 5.14 for aid in comparison. The differences between these two figures gives a insight into the improvements to resolution of the DBAR measurement between a single-detector configuration like this experiment and the coincidence measurement used by Asoka-Kumar *et al.*

Although each absolute momentum broadening curve shape is unique to the experiment due to the particulars of each experiment, comparing measurements in ratio to a another element aids in comparison across experiments. The comparison is made easier as the ratio measurement should reduce the impact of experiment specific effects, such as detector resolution functions. The differences in the shape of the ratio curves between this work and the work of Asoka-Kumar *et al.* is most likely due to the difference in the experimental measurement technique. The data in reference [54] was collected using the coincidence technique and is therefore has a significantly reduced background, allowing for much higher accuracy measurement of positrons annihilating at high p_L.

The shape of the ratio curves in the data collected in this experiment still contains some background and removing this completely is not possible in a single detector system,

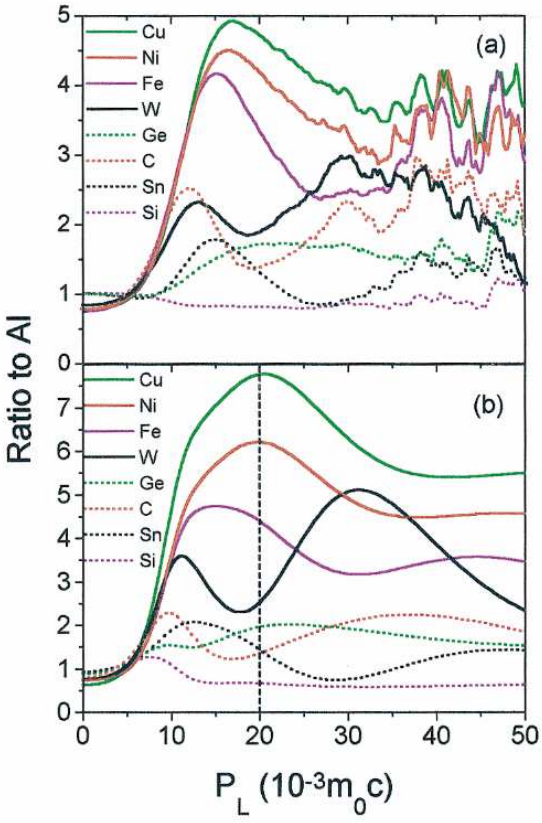

Figure 5.14: Comparison of elemental specificity by Asoka-Kumar *et al.* , from reference [54]. The original caption read "The spectrum for different elements after normalizing to Al: (a) experiment and (b) theory. The theoretical curves for p_L , $20 \times 10^{-3} m_0 c$ [dashed line in (b)] are not accurate."

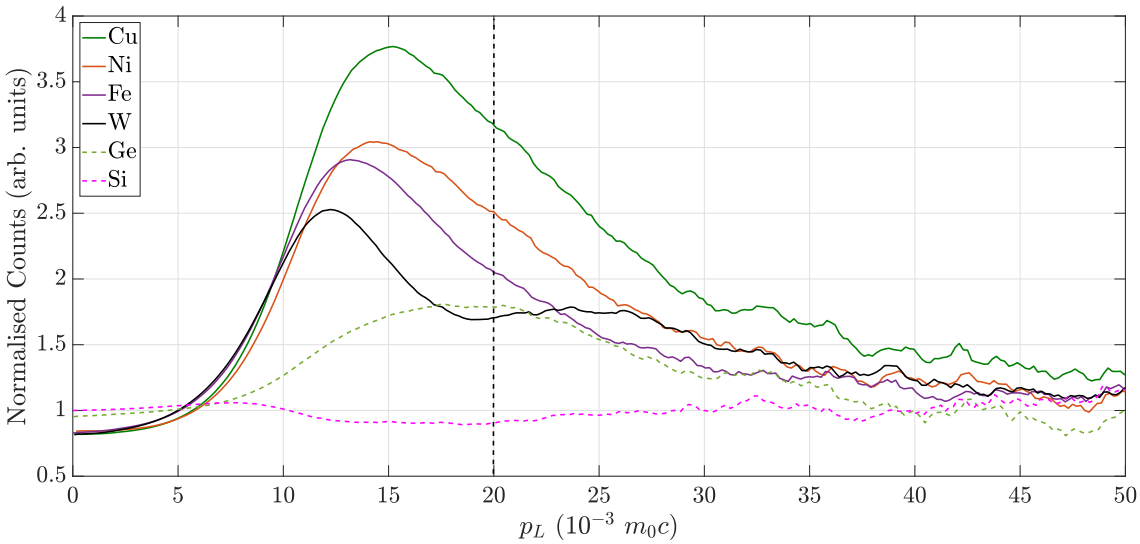

Figure 5.15: Comparison of the momentum broadening in elemental samples, compiled for comparison to the elements measured by Asoka-Kumar *et al.* in reference [54]. The vertical dashed line at $20p_L$ is also reproduced to aid comparison with the reference.

although the main peak to background ratio is approximately 5000. For this reason, the ratio curves after approximately $15 \times 10^{-3} m_0 c$ have a different shape to that of the work in reference [54]. The curve shape (in general) decreases towards 1, as the difference between the the element and the aluminium data decreases, and both spectra become comparable to the background. Although this shape difference does occur, features in the spectra and general trends are distinguishable to $> 35 \times 10^{-3} m_0 c$ for the majority of spectra measured.

Each sample in reference [54] is implanted with 30keV positrons. Although this is a different mean implantation depth for each material as per Mahkov implantation profile calculations, the difference in annihilation environment should be consistent with this experiment. As mentioned previously, at 15keV implantation depth the positron interaction with the surface should contribute negligibly with the spectra, and significant differences in trends between sample data in reference [54] must then only come down to sample preparation.

Comparison with the theoretical work in references [54] and [100] the same deviations in line shape occur as with the comparison of the experimental data alone in reference [54]. To properly evaluate and compare the theoretical calculations presented in [100] it would be necessary scale the the data with a response function representative of the shape of the spectra collected by this experiment, to account for the non-zero background.

Ultimately, this work shows that many of the limitations of a single detector system elemental specificity have been overcome by using DBAR spectra post processing. The measured elemental samples have momentum broadening curves that are unique and easily identifiable using this system, and the spectra are comparable to higher resolution coincidence experiments.

Chapter 6

Experiments with Kapton Polyimide

In this chapter the motivations are discussed for performing experiments on Kapton polyimide. The space environment is discussed with an aim to create space relevant conditions in the laboratory setting, which can be applied as damage experiments on Kapton.

6.1 Properties and Applications of Kapton

Kapton is a durable aromatic polyimide which was originally developed by DuPont in the 1960s and continues to be a commonly used material today as it has many desirable properties which make it suited to a large range of applications. The chemical formula of Kapton is $H_{10}C_{22}N_2O_5$ and the polyimide chain is shown in figure 6.1. Kapton can be found in both general and high performance environments; from insulation in low voltage electrical wiring to aerospace applications in satellites and space mission. The most commonly used types of Kapton film are Kapton-HN, -FN, and -HPP-ST, however many other types are available which provide improved specific material properties such as thermal conductivity, colour pigmentation, or cryogenic insulation [101].

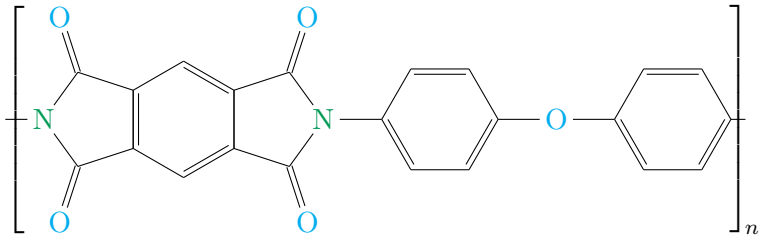

Figure 6.1: Chemical structure of a single Kapton polyimide molecule

Polyimide Films possess unique physical properties that make them ideal candidates

for a variety of electrical and mechanical applications, such as low thermal and electrical conductivity and a wide operating temperature range [101, 102]. The ability of Kapton polyimide films to maintain their physical, electrical, and mechanical properties over a wide temperature ranges and other operating conditions has also opened new applications for plastic films in a large number of fields including aerospace and the biological sciences. Some examples of the uses of Kapton are in positron experiments as a substrate for the radioactive sources that are used for the experiments [39, 103] and as flexible substrates for electronics in the biological health sciences [104].

In spacecraft construction, the James Webb Space Telescopes (JWST) makes use of Kapton in several areas of areas of its design. The JWST will operate much further away from the Earth than other space telescopes, at the Earth - Sun Lagrange point, and will therefore need to operate flawlessly without the option for mechanical fixes like the Hubble Space Telescope. For this reason the parasol-like Sunshield, which blocks the JWST from solar emissions, has been designed with Kapton as its core material. The Sunshield will allow the telescope to remain cool enough to make observations in the near and mid infrared spectrum [105].

6.2 Manipulating the Properties of Kapton

The properties and structure of Kapton films can be changed significantly, and in varying ways, dependent on the processing of the polyimide. Subjecting Kapton to exposure to different temperature environments influences the mechanical properties of Kapton. The mechanical toughness and glass transition temperature of Kapton can be increased by annealing the polyimide below the specified glass transition temperature [106]. Using high temperature annealing regimes, defect networks can be generated within Kapton films which allows Kapton to be used as a molecular sieve [107].

Low energy ion irradiation has remarkably differing results strongly dependent on the species of ion used for the implantation. Low energy irradiation using an O^- beam results in carbon loss in the surface regions through the creation of CO and CO_2 from reaction with the beam [108]. When other elements are used, C-O and C-N bonds are broken, and O and N selectively implanted from the surface layers, creating regions of high carbonization (C-C bonds). Investigation of these layers reveals that they are close to

amorphous graphite [109,110]. Large defect networks can be created through high fluence and long exposure to an ion beam, which increases hardness and elastic modulus [111].

High energy implantation of heavy ions into Kapton creates damaged tracks of disordered carbon through the film [112], as well as generalised carbonization of the sample [113].

6.3 Plasma Damage in Kapton

In the work of Shi *et al.* [114], carbonisation of the Kapton samples immersed in hydrogen plasma was observed using optical transmittance , atomic force microscopy, and FTIR measurements. The concentration of N and O atoms in the Kapton matrix decreased as C=O, C–O–C and C–N bonds were broken during the exposure to the hydrogen plasma.

In exposure to etching plasmas of an O_2/CF_4 mixtures, the CF_4 acts as a catalyist for the etching of the Kapton surface [115]. This was also observed by Lee *et al.* [116], with further analysis revealing that increased carbonisation of the Kapton matrix was dependent on the gas mixture used for the etching, with more damage observed when the Kapton was exposed to plasma mixtures containing oxygen.

In an effort to reproduce conditions similar to the space environment, Sun *et al.* [117] used low energy proton irradiation of Kapton between 60 and 170 keV, which formed pyrolytic carbon free-radicals within the target Kapton samples. The recombination of these free-radicals was also observed, which was faster near the surface than in the bulk.

6.4 The Space Environment

As mentioned earlier in this chapter, Kapton is used in spacecraft construction due to its good thermal characteristics and electrical insulating properties, as well as its flexibility. These desirable properties are well suited to the extreme conditions in satellite missions and interplanetary travel. There are several sources of particles and plasmas that could damage Kapton used in external spacecraft surfaces, including the solar wind and particles trapped within planetary magnetic fields. Since the material properties of Kapton can be influence by processing methods such as ion implantation and plasma etching understanding the damage caused by the space environment is important.

The velocity of a moving spacecraft is high enough to produce effective low energy implantation through impact with particles. A typical low earth orbit speed is approximately 8 kms/s [118], which would give an effective interaction energy of 5eV with an oxygen ion (calculated through basic kinematics).

6.4.1 The van Allen Radiation Belts

The van Allen radiation belts are regions of space close to the Earth which are formed from the Earth's magnetic field. Inside the van Allen radiation belts, objects are primarily exposed to trapped proton and electron plasmas collected from the solar wind and confined by the Earth's magnetosphere. The confined particles are of particular importance to satellites in orbit, as the operating lifetime of the satellites results in a high dose of the trapped particles.

The van Allen radiation belts are described in terms of two regions; the inner van Allen radiation belt, which extends approximately from 0.2 - 2 Earth radii; and the outer van Allen radiation belt, which extends approximately from 3 - 10 Earth radii [119].

The proton energy range for the inner van Allen belt is between 1keV - 300keV, and is most dense closer to the Earth [120]. Imhof and Smith [121] show that the higher energy protons are located within the inner van Allen radiation belt, closer to the Earth. The electron flux for the inner belt has been shown to have electrons around or above 1MeV [122].

The electrons confined in the outer van Allen radiation belt are high energy (at between 1kev - 10MeV) and their concentration is heavily influenced by the current solar wind conditions, thus quite variable [120]. Magnetic storms and other solar events can influence the species and amount of particles present in the belt, and equally so can extended periods of low solar activity [123].

6.4.2 The Solar Wind

The sun constantly emits a particles which make up a varying background that changes with the solar cycle. This is primarily made up of alpha particles, with heavier ions decreasing in abundance with increasing mass. The range in fluence for protons is between $10^3 - 10^7$ protons/cm^2·sr·s, depending on the whether the sun is in a high or low activity

cycle [120].

The solar activity can result in high velocity particles with energies large enough such that they would be implanted a few hundred nanometres into the low density insulating materials on the exterior of spacecraft. Particle velocities from solar radiation sources have been summarised and displayed as the equivalent energy of oxygen ions in table 6.1.

During the solar maximum phase of the 11 year solar cycle, solar particle ejection events from the sun can occur. In general, these events are loosely defined to be a large ejection of particles in a coherent direction, with a total fluence of protons, at energies $\geq$ 30MeV, of $\geq 10^6$ cm^{-2}, although this definition varies [124]. Solar flares and Coronal Mass Ejection (CMEs) events are specific types of solar particle ejection events and have different characteristics that are defined by the process that cause the ejection.

Solar flares are emitted from the sun along interplanetary magnetic field lines, which are shorter events with lower total particle fluxes, typically lasting a few of hours with between 10^7–10^8 cm^{-2} total fluence [124].

CME type events the peak flux of particles from the sun can be as high as $\simeq 10^5$cm$^{-2} \cdot$ s^{-1}, and the event can last for durations on the order of days [120, 124].

Event	Velocity (km/s)	Approximate Energy (keV)
Orbit Speed	8	0.005
Solar Corona	145	1.75
Slow Solar Wind	400	13.2
Fast Solar Wind	750	46.7

Table 6.1: Space relevant particle velocities and equivalent energies for oxygen ions [120, 125, 126].

6.5 Recreating Space-like Conditions in the Laboratory

From the overview presented, the primary considerations for designing an experiment to simulate space conditions are location based — the relative position to the Earth defines the amount and type of environment the material will be exposed to. As a secondary consideration, the duration of a space mission can be simulated by applying the appropriate integrated flux that would apply. Solar minimum and maximum cycles would need to be considered here, as particle fluxes are significantly different.

To investigate the effects of damage in Kapton in conditions relevant to the interplanetary space environment, ion implantation will be carried out as the main damage mode, with a variety of sample preparation factors used to influence the outcome of the implantation in an attempt to characterise the evolution of the damage to Kapton in conditions notionally similar to those found in the solar system.

In ion implantation, one of the most simple variables to control is the amount of implantation performed. The initial variable will therefore be total ion dose, or fluence. A second variable to control in the implantation is the energy of the implanted ion species. Selecting an appropriate energy can mimic the environmental conditions (for example, implanting Kapton using oxygen ions with an energy of 50keV would simulate the fast solar wind [125, 126]) and also aid in analysis of the resulting damage in the sample. By selecting a higher energy for implantation, the final position of the ions is distributed deeper within the material which allows PAS techniques to examine the near surface and region containing the implanted ions separately, by carefully selecting the probe positrons' implantation energy.

As a spacecraft can experience extreme temperature variation depending on which part of it is facing the sun, temperature effects should also be taken into account during environmental recreation. In the laboratory this is relatively simple to perform — samples can be heated or cooled by various means to simulate the temperature variance that a spacecraft would experience.

Interaction with the plasma like environments of the van Allen radiation belts or the upper reaches of a planetary atmosphere can be simulated by exposing Kapton to a hydrogen plasma. Changing the plasma density or sample exposure time will vary the effects of the plasma exposure, as well as the plasma–sample interaction energy, which can be related to a spacecraft mission duration.

To examine the effects of the harsh space environment on spacecraft during a lengthy mission, in the work presented here, Kapton polyimide film was implanted with ions at varying implantation temperature and exposed to plasma.

6.6 Experimental Programme for Ion Damaged Kapton

As noted in the previous section, the three main experiments that were performed to simulate the space environment and damage effects on Kapton are ion implantation, temperature control, and exposure to plasma.

To properly characterise the damage progression in an experimental programme with Kapton as the target material, it is useful to conduct the experiments in such a way that the effects of damage from different sources is individually identifiable. Therefore, a series of measurements will need to be conducted to individually evaluate the effects of temperature, ion irradiation damage (both ballistic damage and chemical effects of ion implantation), and exposure to plasma, before combining the preparations to explore composite effects.

The two components of damage caused by ion implantation are referred to as ballistic damage and chemical effects, and separating out the resulting damage from the two effects separately is important since the properties of Kapton are dependent on the chemical and physical structure. The ballistic damage in ion implantation refers to the damage caused from the transfer of energy from the implanted ions into the target material. The chemical effects refer to the interaction of the implanted ion with the target material where the implanted ions come to rest. At the ion implantation layer the implanted species may chemically interact with the target material, effectively changing the material by replacing constituent atoms or forming new compounds entirely.

The choice of ion species used for implantation in Kapton has a significant impact on the damage type, as described in section 6.2. To investigate these effects separately, ion implantation was performed using an ion species much less likely to interact strongly with the Kapton polyimide chain and another that is likely to readily interact; gallium and oxygen. Gallium was chosen as a medium weight ion to investigate the ballistic effects of ion implantation as it is less reactive than other elements close to it in the periodic table, and the relative ease of implantation in comparison of noble gases. Oxygen was chosen as oxygen is a constituent element in the Kapton polyimide chain and is likely to react with the Kapton [108, 116], as well as being one of the higher abundance ions in particle emissions from the sun [120].

To investigate the effects of temperature on the effects of ion implantation, the im-

plantation was performed with the sample heated or cooled to different temperatures during implantation. The ion implantation facilities used in sample preparation allow for temperature control on the sample stage, where the target samples are held during implantation [127]. The implantation temperature can therefore be varied; the Kapton sample can be cooled by liquid nitrogen, left at room temperature, or heated.

To simulate interaction with the van Allen radiation belt, or cold upper atmospheres of planets, the Kapton samples were exposed to hydrogen plasma using the the MAGnetized Plasma Interaction Device (MAGPIE), a helicon-excited plasma device at the Plasma Research Laboratories at the Australian National University [128]. The MAGPIE experiment allows a material sample to be exposed to a plasma for a varying amount of time with a tunable plasma density and plasma-sample interaction energy, which was used in this work to simulate the effects of a long duration space mission.

To characterise all of the damage effects in the experimental program a progressive series of Kapton samples were created so that the characterisation can identify specific effects from the particular damage source in the sample preparation. The ion implantation was carried out with a higher energy that found in solar particle sources so that surface and implantation layer analysis can be performed separately using positron annihilation spectroscopy. As ion implantation is performed controlling the dose of implanted particles, the effects of increasing fluence can be determined, which relates to the duration of a space mission through the relevant flux of particles in space.

Chapter 7

Ion Implantation into Kapton Polyimide Film

In this chapter data is presented for results from Kapton polyimide film damaged through ion implantation which is analysed using PALS and DBAR. The Kapton samples were implanted with gallium ions to investigate the effects of ballistic damage, and a separate series of samples were implanted with oxygen ions to explore combined ballistic damage and chemical interaction.

7.1 Sample Preparation and Experimental Set-up

Preparation of the implanted Kapton film was performed using the low energy particle accelerator at The Australian National University [127]. Commercially available 50 μm thick Kapton polyimide films (DuPont) were implanted with gallium and oxygen ions at liquid N_2 temperature (LNT), 23°C (RT) and at 250°C (HT). The beam currents were kept below ∼150 nA, to stem any beam induced heating effects. The gallium fluences varied from 1×10^{12} to 1×10^{15} ions·cm^{-2}, and the oxygen fluences were 1×10^{14} and 1×10^{15} ions·cm^{-2}.

In the PALS analysis the energy for the implantation of the positrons was determined by the methods outlined in section 3.4 in order to best interrogate the damage induced from ion implantation. Simulations were made of the ion implantation into Kapton using SRIM/TRIM [67, 68]. The Mahkov implantation profiles for positrons were calculated to overlap with the simulation results from SRIM/TRIM (as described in section 2.3.1) and the positron energies that were a best match were used to make detailed positron implantation simulations using pyPenelope [69]. The positron energies were set to probe

the near surface region of the Kapton samples, and a second measurement was made to probe the region of highest damage induced by the ion implantation and the final resting location of the implanted ions. It should be noted that the range of the implanted positrons calculated in this manner is complicated by the fact that positronium could form and diffuse through the sample; the positronium diffusion length in undamaged Kapton calculated to be $\simeq$ 5.5nm however this could be larger in the presence of a large defect network [14, 96]. Given the likely diffusion length of positrons in Kapton polyimide, this effect on the implantation profile is expected to be negligible. The results of the ion implantation simulations and the corresponding positron implantation profiles for PALS and DBAR measurements are shown in figures 7.1, 7.2, and 7.3. The positron implantation energies to make PALS measurements are outlined in table 7.1.

Kapton Sample	Positron implantation energy (keV)	
	Near Surface	Maximum Damage Region
300keV Gallium	2	5
50keV Oxygen	2	3
100keV Oxygen	2	4.25

Table 7.1: Calculated positron implantation energies for the programme of PALS measurements

The overlap between the implanted positrons and the damage profile in the gallium implanted Kapton samples (shown in figure 7.3 with energies detailed in table 7.1) is not as complete as the oxygen implantation regimes in figures 7.1 and 7.2. The gallium implantation experiments were conducted before the oxygen series, and the initial gallium experiment attempted to fully separate the implanted positron pulse from the near surface region, as well as sample the region in which the implanted gallium comes to rest.

PALS analysis was performed on all of the prepared samples using the positron materials beamline as described in chapter 3. The PALS spectra used as an instrument function was the same sample of undamaged Kapton-HN film for each measurement.

The oxygen implanted samples were additionally investigated using the DBAR experiment as described in chapter 4. A depth profiling DBAR measurement was made using quicker, lower count spectra ($\simeq 1 \times 10^6$ total counts in the region of the 511keV annihilation photopeak) at various positron implantation energies from $0.25 - 15$keV. More

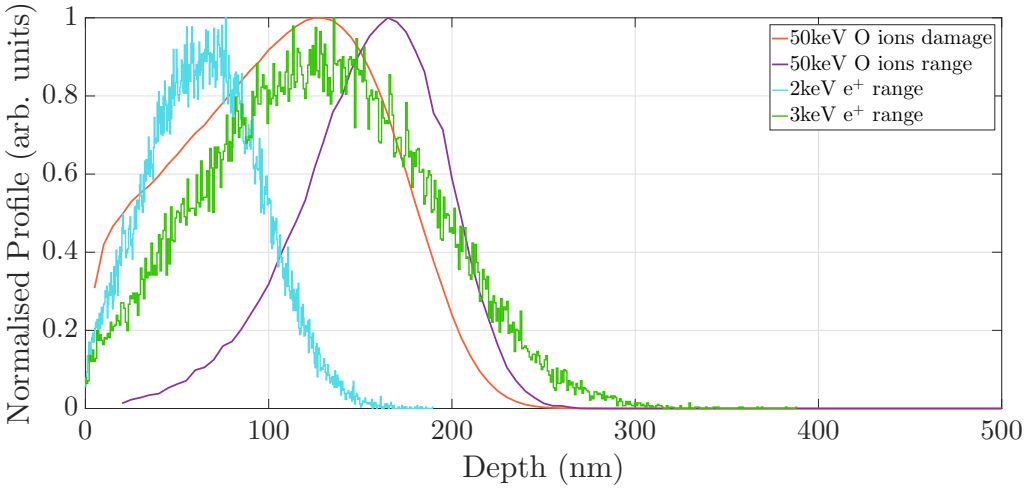

Figure 7.1: Simulataed implantation of 50keV oxygen ions into a substrate of Kapton polyimide film.

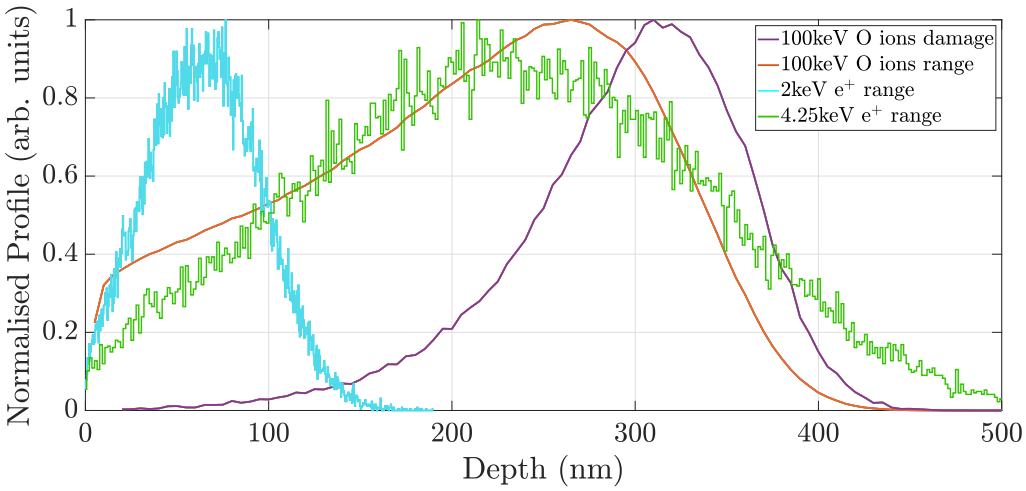

Figure 7.2: Simulated implantation of 100keV oxygen ions into a substrate of Kapton polyimide film.

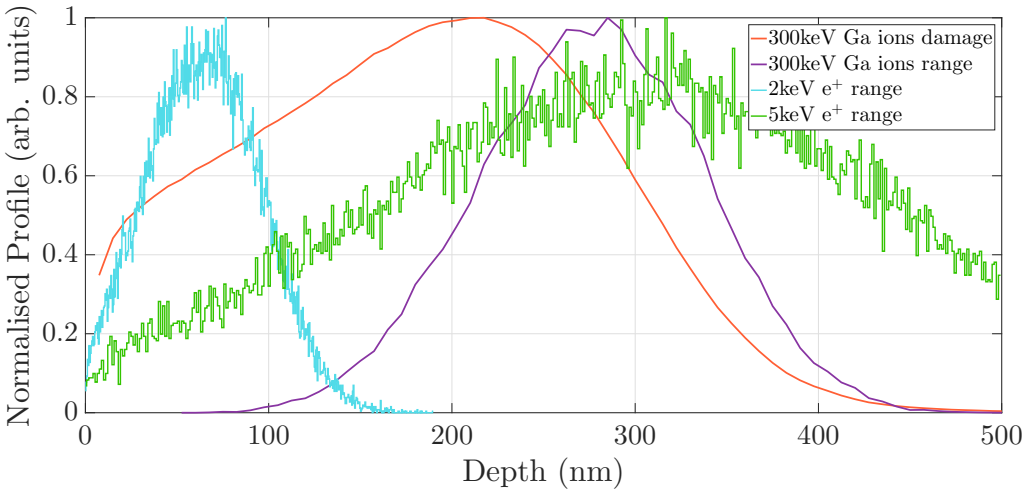

Figure 7.3: Simulated implantation of 300keV gallium ions into a substrate of Kapton polyimide film.

detailed spectra ($\simeq 16 \times 10^6$ total counts) were taken at the positron implantation energies at which PALS measurements were also made.

7.2 300keV Gallium Implantation

As mentioned in the previous section, the Kapton polyimide film implanted with 300keV gallium ions at HT, RT, and LNT temperatures were investigated using PALS at the near surface and damage layer. There were no observed lifetimes in the gallium implanted Kapton samples at fluences below 1×10^{14} ions·cm^{-2}, the only samples with observed lifetimes were those implanted with gallium fluences of 1×10^{14} and 1×10^{15} ions·cm^{-2}. As described in section 3.5, the analysis technique is insensitive to intrinsic positron lifetimes in the Kapton polyimide. Therefore the lack of observed lifetimes does not imply there are no positron lifetimes present in the measured sample, they are not measurable by this PALS analysis technique.

7.2.1 Near Surface Region

2keV Implanted Positrons - Near Surface			
Fluence (ions·cm^{-2})	Implantation Temperature	Lifetime (ns)	Weight (%)
1×10^{14}	HT	0.68 ± 0.05	2.9 ± 0.2
	RT	-	-
	LNT	-	-

Table 7.2: Near surface PALS analysis of Kapton implanted with gallium at 1×10^{14} ions·cm^{-2}, as probed by 2keV positrons.

2keV Implanted Positrons - Near Surface			
Fluence (ions·cm^{-2})	Implantation Temperature	Lifetime (ns)	Weight (%)
1×10^{15}	HT	0.74 ± 0.06	6.0 ± 0.9
	RT	0.67 ± 0.04	5.5 ± 0.3
	LNT	0.83 ± 0.04	3.6 ± 0.1

Table 7.3: Near surface PALS analysis of Kapton implanted with gallium at 1×10^{15} ions·cm^{-2}, as probed by 2keV positrons.

The near surface region of the gallium implanted Kapton was probed by 2keV positrons and the positron lifetimes found are presented in tables 7.2 and 7.3. In this case, the low

fluence implantation at 1×10^{14} ions·cm^{-2} shows damage only in the HT sample. Both the LNT and RT implantation shows no observable lifetimes.

The implantation at 1×10^{15} ions·cm^{-2} shows damage at all three implantation temperatures in this near surface region. The amount of damage increases with temperature as indicated by the increasing weight of the observed lifetime, the LNT sample has the lowest weighting (and therefore defect concentration) but the HT and RT samples have the same weighting (within experimental uncertainty). The size of the defects follows a different pattern, in the three samples it is highest at HT and LNT and the observed lifetime is the same in the LNT and HT samples within experimental uncertainty (1.25σ difference). The lifetime at RT is appreciably different in size at 2.83σ difference from the LNT defect.

In particular, we can infer that these results from PALS analysis show that the RT sample exhibits less damage than the LNT and HT samples.

7.2.2 Maximum Damage Region

5keV Implanted Positrons - Maximum Damage Region			
Fluence (ions·cm^{-2})	Implantation Temperature	Lifetime (ns)	Weight (%)
1×10^{14}	HT	0.46 ± 0.03	5.8 ± 0.5
	RT	-	-
	LNT	0.33 ± 0.03	5.7 ± 0.8

Table 7.4: Maximum damage region PALS analysis of Kapton implanted with gallium at 1×10^{14} ions·cm^{-2}, as probed by 5keV positrons.

5keV Implanted Positrons - Maximum Damage Region			
Fluence (ions·cm^{-2})	Implantation Temperature	Lifetime (ns)	Weight (%)
1×10^{15}	HT	1.03 ± 0.06	3.5 ± 0.1
	RT	0.43 ± 0.02	6.8 ± 0.6
	LNT	0.43 ± 0.02	7.4 ± 0.4

Table 7.5: Maximum damage region PALS analysis of Kapton implanted with gallium at 1×10^{15} ions·cm^{-2}, as probed by 5keV positrons.

The maximum damage region is where the greatest damage has been induced by the implanted gallium ions and is probed by 5keV positrons, with the lifetimes that have been

found detailed in tables 7.4 and 7.5. In this case, we find that the relationships between fluence, sample preparation temperature, and resultant defect are similar to the PALS results for the near surface region.

The Kapton implanted with the low fluence gallium at 1×10^{14} ions$\cdot cm^{-2}$ shows defect a similar concentration in the LNT and HT samples, but the LNT sample has a significantly smaller lifetime (and hence, total defect volume). The RT prepared sample shows no observable lifetime.

The sample prepared with high fluence gallium implantation at 1×10^{15} ions$\cdot cm^{-2}$ shows a pattern of defect concentration decreasing with increasing sample preparation temperature. The RT and LNT prepared samples have the same observed lifetimes, whereas the HT sample has a much larger positron lifetime albeit with a reduced weighting in the lifetime fit. The difference weighting in the LNT and RT samples can be attributed to a qualitative increase in observed damage in the LNT sample, as the compared lifetimes are equal and the weighting is changing, however comparing the weightings directly between the RT or LNT and the HT sample is not as definitive as the associated weighting is related to the magnitude of the observed lifetime.

The observed 1.03 ± 0.06ns lifetime in the HT sample corresponds to a spherical pore radius of 0.17 ± 0.01nm, calculated using the Tao-Eldrup model (the Tao-Eldrup model is applicable in this instance, as the lower limit of lifetimes relevant to this model is approximately 0.4ns) [38, 39]. This lifetime is significantly larger than the lifetimes observed in other samples which imply that the HT sample has the most damage, despite the lowest associated weighting.

7.3 50keV Oxygen Implantation

These samples were prepared with oxygen ion fluences of 1×10^{14} and 1×10^{15} ions$\cdot cm^{-2}$, low and high fluence respectively. Both PALS and DBAR measurements were made on these samples.

7.3.1 50keV Oxygen Implantation at Low Fluence

The results of the PALS analysis of the Kapton samples implanted with 50keV oxygen ions at low fluence are detailed in tables 7.6 and 7.7. There were no observed positron

lifetimes in the near surface region, as probed by 2keV positrons. This null result is shown in table 7.6 for completeness and ease of comparison.

In the Kapton implanted with oxygen at 1×10^{14} ions·cm^{-2} there are lifetimes observed in all three samples at the maximum damage region, which are identical within experimental uncertainty. The weightings of these lifetimes become very large, at 42 ± 5% in the HT sample. The LNT sample has the next largest intensity, followed by the RT sample with the lowest weight.

2keV Implanted Positrons - Near Surface			
Fluence (ions·cm^{-2})	Implantation Temperature	Lifetime (ns)	Weight (%)
1×10^{14}	HT	-	-
	RT	-	-
	LNT	-	-

Table 7.6: Near surface PALS analysis of Kapton implanted with oxygen at 1×10^{14} ions·cm^{-2}, as probed by 2keV positrons.

3keV Implanted Positrons - Maximum Damage Region			
Fluence (ions·cm^{-2})	Implantation Temperature	Lifetime (ns)	Weight (%)
1×10^{14}	HT	0.315 ± 0.019	42 ± 5
	RT	0.34 ± 0.05	12 ± 2
	LNT	0.34 ± 0.04	27 ± 4

Table 7.7: Maximum damage region PALS analysis of Kapton implanted with oxygen at 1×10^{14} ions·cm^{-2}, as probed by 3keV positrons.

From previous work by McGuire and Keeble [129], the intrinsic positron lifetimes in Kapton HN films is approximately 275 and 410 pico-seconds, at $\simeq$ 33% and $\simeq$ 67% weighting respectively, which averages to a lifetime of 342.5 picoseconds. As mentioned in chapter 3, the PALS technique used to measure the lifetimes in this work cannot directly measure the intrinsic lifetimes in materials, and 300 picoseconds is at the lower end of the effective resolution of the experiment. The large weightings observed in these samples could imply that the induced damage is enhancing the intrinsic lifetimes in Kapton, giving rise to the unusually high weighting values found. However, given the insensitivity to the intrinsic lifetimes in Kapton, these observed lifetimes are likely to be distinct from the intrinsic lifetimes in Kapton and generated by the damage from the bombarding ions.

Figures 7.4 and 7.5 show the detailed DBAR measurements from the near surface

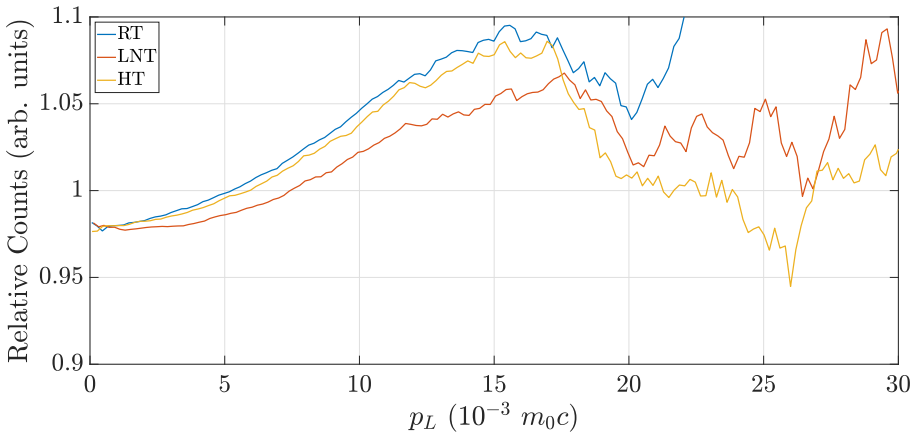

Figure 7.4: Momentum distribution of 50keV oxygen implantation into Kapton film at 1×10^{14} ions·cm^{-2}, as measured by DBAR from positrons implanted at 2keV.

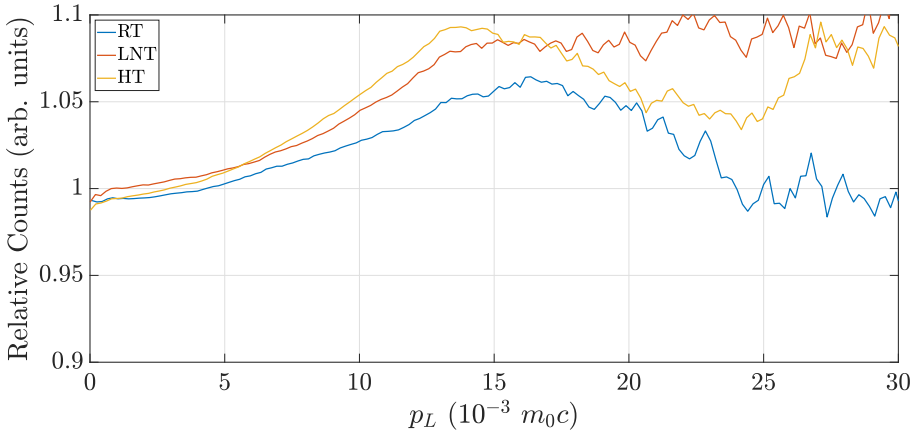

Figure 7.5: Momentum distribution of 50keV oxygen implantation into Kapton film at 1×10^{14} ions·cm^{-2}, as measured by DBAR from positrons implanted at 3keV.

region and damaged layer respectively. The annihilation photopeak counts ($\simeq 16 \times 10^6$ counts) are shown in ratio to the Kapton reference sample to examine the deviations due to the sample preparation and ion implantation.

The shape of each sample's momentum distribution curve is similar at both annihilation depths, however at the near surface region (figure 7.4) the measured samples have an initial normalised count below that of the reference Kapton sample (below 1.0), and at the maximum damage region (figure 7.5) the normalised counts begin much closer to that of the Kapton standard. The ratio curve below 1.0 normalised counts at the surface region indicates that fewer positrons are annihilating with electrons with low momentum. This is further supported by the shape of the broadening curve increasing towards higher counts at larger p_L. The increase in relative counts at high p_L is consistent with the positrons annihilating at sites containing the implanted oxygen, as the positrons will sample the region in which the implanted oxygen inhabits (as shown by the implantation profiles in figure 7.1) and additional oxygen would provide more higher momentum electrons.

Although the momentum distribution curve shapes in the maximum damage region (shown in figure 7.5) are similar to that of the near surface region, at the maximum damage region the HT and LNT samples are closest to one another. The RT sample curve is significantly different and consistently below the HT and LNT curves. The differences in the momentum broadening may be indicated by the weightings associated with the observed positron lifetimes — the RT sample has a significantly lower weight (12±2%) than the HT and LNT samples ($42 \pm 5\%$ and $27 \pm 4\%$, respectively), although this does not adequately account for the difference in weight between the HT and LNT samples, which have similar momentum broadening curves.

The S parameter plot as a function of positron implantation energy in figure 7.6 shows that all three samples start at similar S parameter values and the LNT and HT samples have very similar values throughout the the depth profiling measurement. The RT sample follows the HT sample between $1-2.5$keV after which the RT sample is consistently below the other LNT and HT samples. There is, however, large scatter between the points in the RT curve, despite the data points being smoothed.

The W parameter curve follows the same pattern as the S parameter curve, but inverted. There is is little notable variation from the inverted trends seen in the S parameter

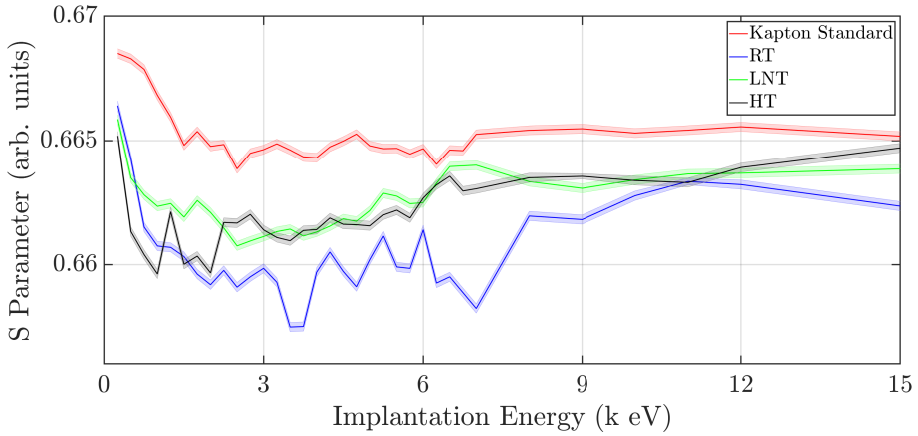

Figure 7.6: S parameter as a function of positron implantation energy in Kapton implanted with 50keV oxygen ions, at 1×10^{14} ions$\cdot cm^{-2}$. The original data has been smoothed by a 3-point moving average to produced the curve and the shaded area represents the uncertainty associated with the central line.

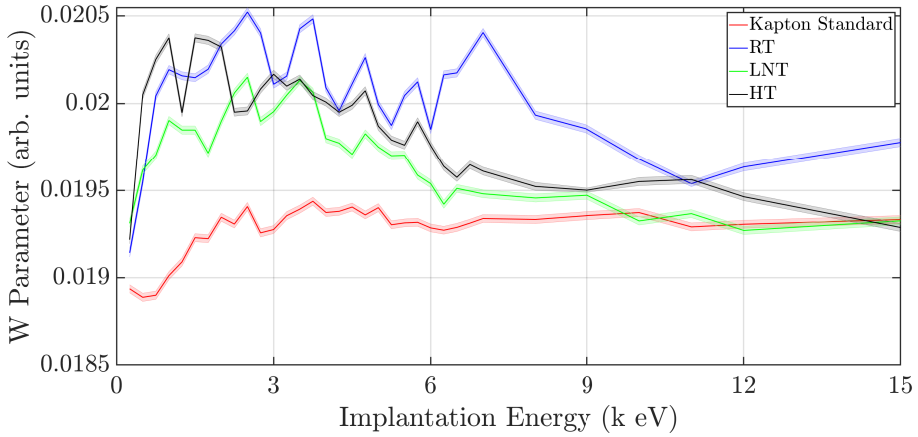

Figure 7.7: W parameter as a function of positron implantation energy in Kapton implanted with 50keV oxygen ions, at 1×10^{14} ions$\cdot cm^{-2}$. The original data has been smoothed by a 3-point moving average to produced the curve and the shaded area represents the uncertainty associated with the central line.

depth profile plot.

7.3.2 50keV Oxygen Implantation at High Fluence

2keV Implanted Positrons - Near Surface			
Fluence (ions·cm^{-2})	Implantation Temperature	Lifetime (ns)	Weight (%)
1×10^{15}	HT	1.22 ± 0.22	2.6 ± 0.3
	RT	0.68 ± 0.05	4.6 ± 0.3
	LNT	0.48 ± 0.02	8.7 ± 0.4

Table 7.8: Near surface PALS analysis of Kapton implanted with oxygen at 1×10^{15} ions·cm^{-2}, as probed by 2keV positrons.

3keV Implanted Positrons - Maximum Damage Region			
Fluence (ions·cm^{-2})	Implantation Temperature	Lifetime (ns)	Weight (%)
1×10^{15}	HT	0.43 ± 0.02	20 ± 1
	RT	0.43 ± 0.04	24 ± 3
	LNT	0.45 ± 0.04	19.1 ± 1.1

Table 7.9: Maximum damage region PALS analysis of Kapton implanted with oxygen at 1×10^{15} ions·cm^{-2}, as probed by 3keV positrons.

The PALS results for 50keV implanted Oxygen at 1×10^{15} as probed by 2keV positrons (near surface region) show a pattern of the observed positron lifetime increasing with implantation temperature. The weighting associated with the lifetime has the opposite trend – HT has the lowest weighting and LNT has the highest. From this pattern the conclusion is that there are more smaller sized imperfections at low temperature, and at high temperature there are larger vacancies at a lower concentration. The largest observed PALS lifetime in the HT sample of 1.22 ± 0.22ns corresponds to a spherical pore of radius 0.20 ± 0.04nm calculated using the Tao-Eldrup model [38, 39].

By contrast to the near surface region, table 7.9 shows that within the maximum damage region all three implantation temperatures yield the same lifetime with very similar weights (within experimental uncertainty).

The momentum distribution of the Kapton sample found with 2keV positrons shows that the RT and LNT samples have momentum distributions that are very similar to one another, and the momentum distribution of the HT sample is lower in the region between $0 - 15p_L$. The RT and LT momentum distributions follow the same pattern with an

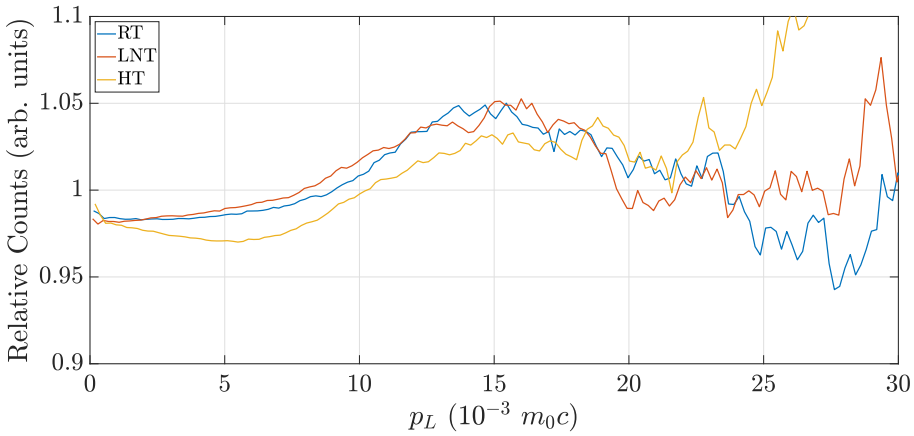

Figure 7.8: Momentum distribution of 50keV oxygen implantation into Kapton film at 1×10^{15} ions·cm^{-2}, as measured by DBAR from positrons implanted at 2keV.

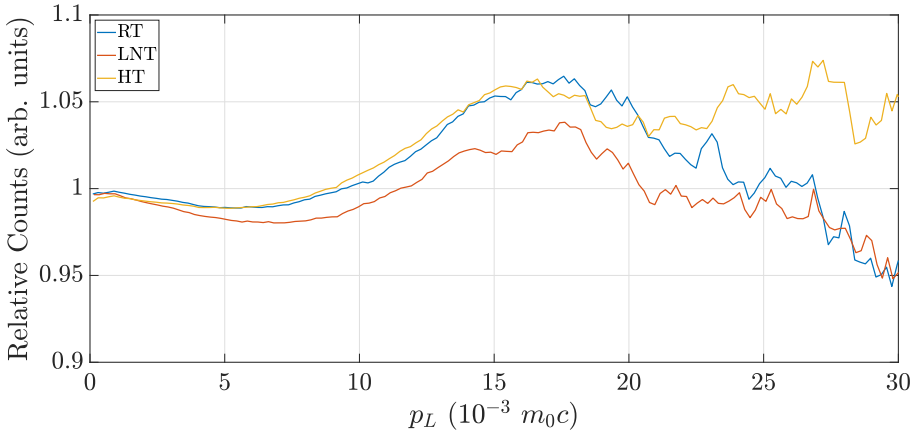

Figure 7.9: Momentum distribution of 50keV oxygen implantation into Kapton film at 1×10^{15} ions·cm^{-2}, as measured by DBAR from positrons implanted at 3keV.

increasing gradient from $0 - 15p_L$. The HT sample shows an initially decreasing gradient until reaching a turning point at $\simeq 5p_L$. The differences in these curves indicates that the chemical environment in the HT sample is different to the RT and LNT samples, and could account for the much larger observed lifetime. The RT curve lies slightly below the LNT momentum distribution between $\simeq 0 - 12p_L$ which indicates a progression from the chemical environment in the LNT sample towards that of the HT sample. The progression in this manner is supported by the results from the PALS analysis in the previous section, showing increasing lifetime with increasing temperature and decreasing weight with temperature.

In the momentum distribution of annihilation radiation from positrons implanted at the maximum damage region (3 keV), the RT and HT samples have very similar momentum

distributions and the LNT sample is consistently lower between $0-20p_L$. Each momentum distribution curve at the maximum damage region starts with a negative gradient, which becomes positive between $5-7p_L$. The momentum distribution curves are consistent with the results from the PALS analysis, although it is difficult to draw any hard conclusions as the PALS lifetimes and weightings are identical within experimental uncertainty and the relative counts for the LNT sample are consistently lower than the other two samples. This suggests that the differences between the samples in the PALS measurements ($\simeq$ 0.426 nanoseconds in the RT and HT samples compared to $\simeq$ 0.451 in the LNT sample) may be real, however is weak due to the experimental uncertainty. Similar to the low fluence samples the momentum distribution at $0p_L$ is very close to 1.0, indicating that there are similar fractions of positrons annihilating with low momentum electrons in the damaged and reference samples. In contrast to the low fluence sample, the LNT sample has a different line shape which suggests that more higher momentum electrons are present at annihilation sites and thus the chemical environment is different. The fact that the observed PALS lifetimes are different between the two implantation fluences ($\simeq$ 0.35ns at low fluence and $\simeq$ 0.45ns at high fluence) supports the idea of the increased fluence creating a different kind of defect and a different chemical environment in which the positrons annihilate.

In the S parameter plot as a function of positron implantation energy, shown in figure 7.10, each sample has significantly different S parameter values close to the surface (at $\simeq$ 0.25keV) and the plots converge at approximately 3keV positron implantation energy. Above 8keV positron implantation energy, the RT and LNT samples are similar to the Kapton standard and the HT sample is consistently below all the other curves. The damaged samples are all consistently below the Kapton reference sample. The convergence at 3keV positron implantation energy aligns well with the similarities in the observed positrons lifetimes at this analysis energy.

The W parameter depth profile measurement shows almost identical behaviour for each of the samples until $\simeq$ 6.5keV positron implantation energy at which point the RT and LNT samples match up with the Kapton reference sample. The HT remains above the other samples from $\simeq 6.5-13$keV. At low positron implantation energy the differences between the three damaged samples is much lower that in the S parameter plot.

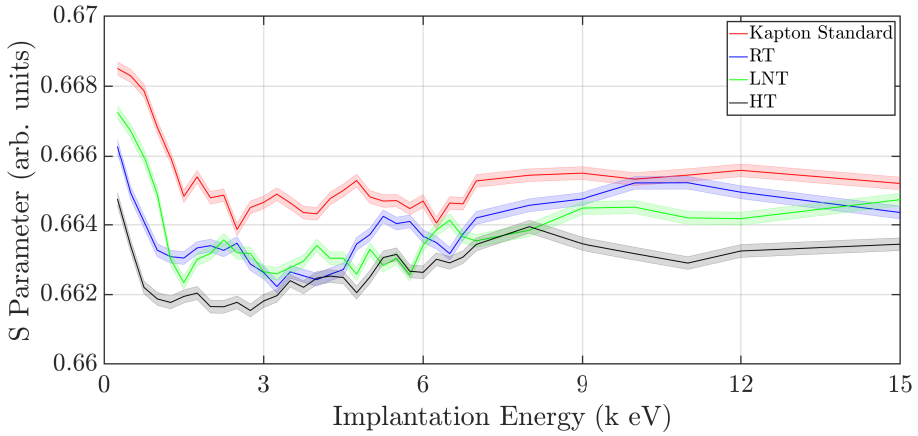

Figure 7.10: S parameter as a function of positron implantation energy in Kapton implanted with 50keV oxygen ions, at 1×10^{15} ions$\cdot cm^{-2}$. The original data has been smoothed by a 3-point moving average to produced the curve and the shaded area represents the uncertainty associated with the central line.

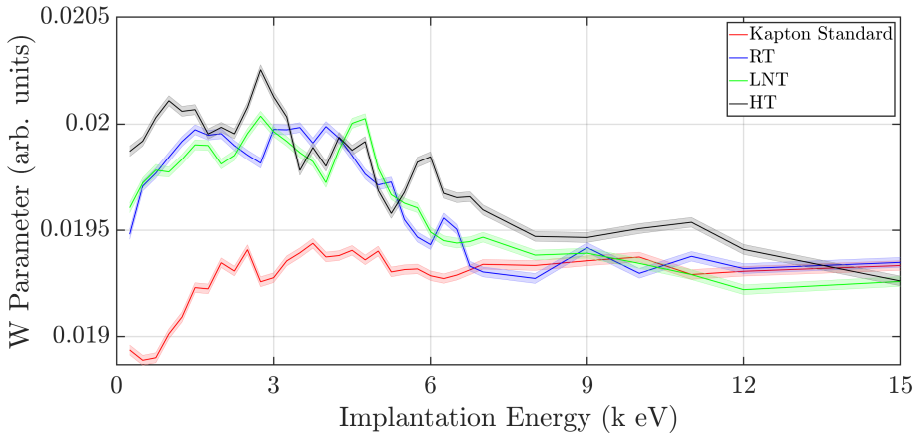

Figure 7.11: W parameter as a function of positron implantation energy in Kapton implanted with 50keV oxygen ions, at 1×10^{15} ions$\cdot cm^{-2}$. The original data has been smoothed by a 3-point moving average to produced the curve and the shaded area represents the uncertainty associated with the central line.

7.4 100keV Oxygen Implantation

The Kapton samples prepared by 100keV oxygen implantation were done so at a single fluence of 1×10^{15} ions $\cdot cm^{-2}$.

7.4.1 100keV Oxygen Implantation at High Fluence

2keV Implanted Positrons - Near Surface			
Fluence (ions$\cdot cm^{-2}$)	Implantation Temperature	Lifetime (ns)	Weight (%)
1×10^{15}	HT	1.5 ± 0.3	1.45 ± 0.16
	RT	0.61 ± 0.04	4.4 ± 0.2
	LNT	-	-

Table 7.10: PALS results for 100keV implanted Oxygen at 1×10^{15} as probed by 2keV positrons

4.25keV Implanted Positrons - Maximum Damage Region			
Fluence (ions$\cdot cm^{-2}$)	Implantation Temperature	Lifetime (ns)	Weight (%)
1×10^{15}	HT	0.35 ± 0.018	9.1 ± 0.7
	RT	-	-
	LNT	0.322 ± 0.015	12.0 ± 0.9

Table 7.11: PALS results for 100keV implanted Oxygen at 1×10^{15} as probed by 4.25keV positrons

The results of the PALS analysis at the surface of the 100keV oxygen implanted Kapton show a large lifetime in the HT sample, and a smaller lifetime in the RT sample. There is no observed lifetime in the LNT sample. The observed lifetimes and related weighting are detailed in table 7.10. The lifetime in the HT sample is over twice that of the RT sample (1.5 nanoseconds compared to 0.61), yet has a much lower weighting (1.45%compared to 4.4%). The interplay between lifetime and weighting in these samples indicate that increasing the implantation temperature results in fewer defects (a reduction in weight), but the defects are larger (an increase in positron lifetime). The observed 1.5 ± 0.3ns lifetime corresponds to a 0.24 ± 0.07nm defect radius calculated using the Tao-Eldrup model [38, 39].

At the maximum damage region, as probed by 4.25keV positrons, the observed positron lifetimes in the HT and LNT samples are the same (within experimental uncertainty), with statistically different weightings — $9.1 \pm 0.7\%$ in the HT sample and $12.0 \pm 0.9\%$

in the LNT sample. This follows the pattern at the surface region, in that increasing the implantation temperature results in a lower positron lifetime weighting, however the two lifetimes observed in this case are 1.35σ apart, making them indistinguishable within experimental uncertainty. Notably, there is no lifetime observed in the RT sample at this positron implantation energy, despite the lifetime observed in the near surface region and the similarities between the momentum broadening curve of the RT sample and that of the HT sample (shown in figure 7.13).

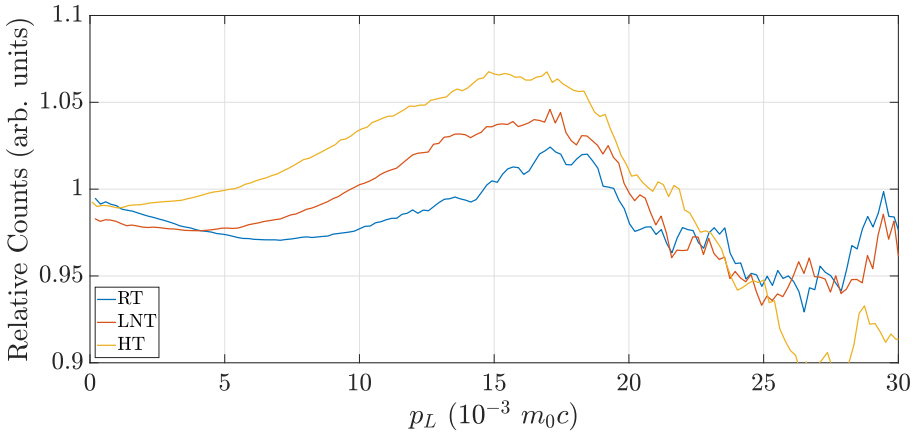

Figure 7.12: Momentum distribution of 100keV oxygen implantation into Kapton film at 1×10^{15} ions·cm^{-2}, as measured by DBAR from positrons implanted at 2keV.

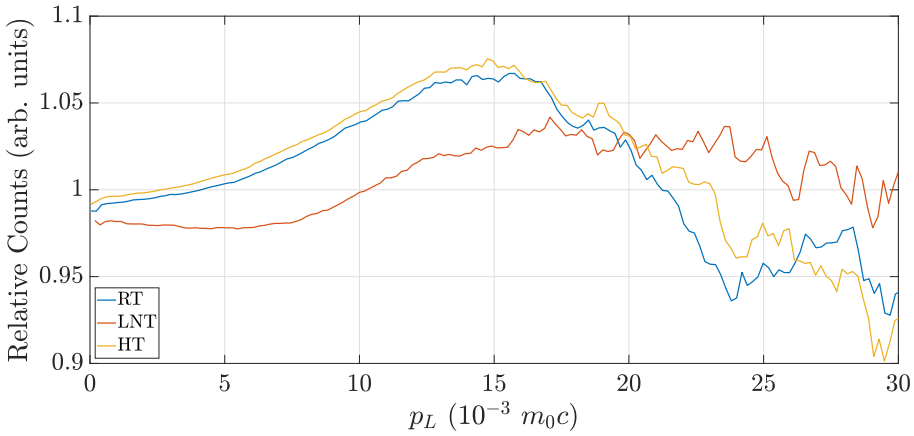

Figure 7.13: Momentum distribution of 100keV oxygen implantation into Kapton film at 1×10^{15} ions·cm^{-2}, as measured by DBAR from positrons implanted at 4.25keV.

The high detail DBAR analysis of the momentum broadening of the 100keV implanted Kapton at the near surface region, as probed by 2keV positrons (figure 7.12), shows that the broadening curve for the LNT and HT samples follow the same curve shape, with the LNT sample displaced from the HT sample. The three momentum broadening curves

have the same curvature between $0-15p_L$, with minima at approximately different points along the x-axis, $0p_L$ for HT, $4p_L$ for LNT, and $7p_L$ for RT.

All three samples start with normalised counts below 1.0 at both the near surface and maximum damage regions (shown in figure 7.13), showing increased momentum broadening compared to the positrons annihilating in the Kapton polyimide in the reference sample. The momentum broadening curve for the both the LNT and HT samples do not change significantly from the near surface and maximum damage region implying that the damage in the both regions results in similar chemical environments. This is notable because the lifetimes and associated weightings found using PALS show large changes between the near surface and maximum damage regions in all three samples despite the similarities in the momentum broadening curves. The RT sample has completely different momentum broadening curves at the near surface region and the maximum damage region, suggesting that the chemical environment in each region is significantly different. The PALS results for this sample show considerable differences too – at the surface a $\simeq$ 0.6ns lifetime is observed, but at the maximum damage region no lifetime is observable.

Figures 7.14 and 7.15 show the DBAR measurements of the S and W parameters as a function of positron implantation energy. In general the W parameter plot in figure 7.15 is the inversion of the S parameter plot in figure 7.14, albeit with different y-axis values.

In the S parameter plot, each damaged sample lies below the Kapton standard, except at low positron implantation energies ($\simeq$ 0.25keV) where both the RT and LNT samples are slightly above the Kapton standard. Between 1.5keV and 3.75keV positron implantation energy, the RT sample changes curve shape, moving away from the LNT curve.

7.5 Discussion

The gallium and oxygen ion implantation of Kapton polyimide film show induced defects and chemical changes with dependencies on ion fluence and implantation temperature.

Visually, the usual golden-brown of the prepared Kapton samples transitions to an almost black, dark brown, clearly showing the implantation area. The colour change increases with implantation fluence, and the samples darken dependent on the implantation temperature — samples prepared at 250°C are darker than the ones implanted at liquid

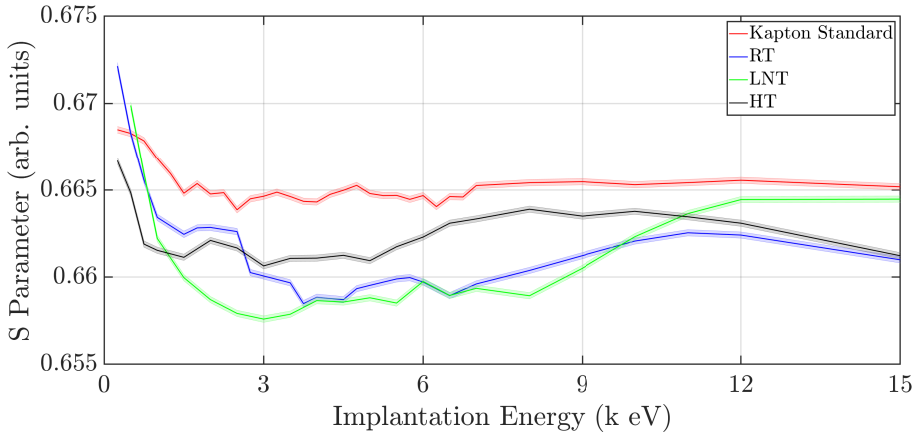

Figure 7.14: S parameter as a function of positron implantation energy in Kapton implanted with 100keV oxygen ions, at 1×10^{15} ions$\cdot cm^{-2}$. The original data has been smoothed by a 3-point moving average to produced the curve and the shaded area represents the uncertainty associated with the central line.

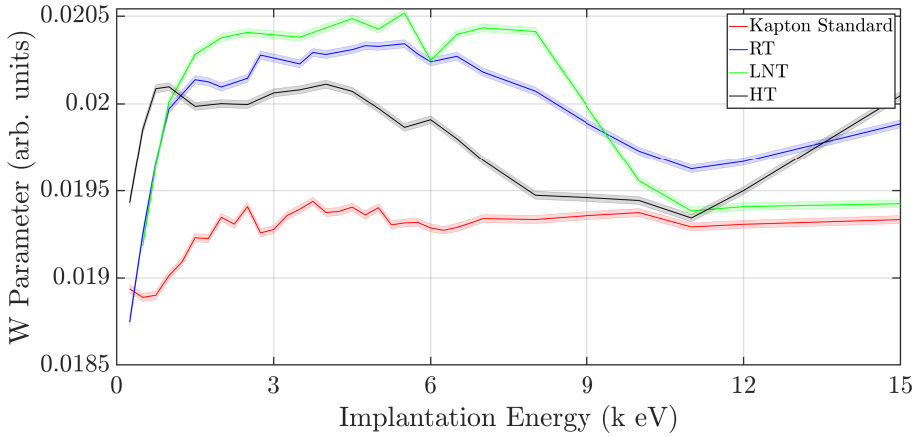

Figure 7.15: W parameter as a function of positron implantation energy in Kapton implanted with 100keV oxygen ions, at 1×10^{15} ions$\cdot cm^{-2}$. The original data has been smoothed by a 3-point moving average to produced the curve and the shaded area represents the uncertainty associated with the central line.

nitrogen temperature, which are darker than the samples implanted at room temperature. The HT sample implanted at 1×10^{15} ions$\cdot cm^{-2}$ is the darkest. The samples implanted with very low fluence show a slight colour change which is almost not visible.

The implantation of the gallium ions below a fluence of 1×10^{14} ions$\cdot cm^{-2}$, detailed in tables 7.2 and 7.4, did not cause enough changes to the Kapton polyimide for the PALS analysis to find any induced lifetimes. At implantation fluences of 1×10^{14} ions$\cdot cm^{-2}$, some of the implanted samples still do not show any lifetimes in the PALS analysis, although all samples do show signs of changes to the material from the DBAR analysis. As there are no PALS lifetimes observed below a fluence of 1×10^{14} ions$\cdot cm^{-2}$ in the gallium implanted samples, this gives a threshold for ballistic damage effects to become large enough to be detected by the PALS analysis technique. Compared to the gallium implantation, the oxygen ions are much lighter (atomic mass of 8 in oxygen and 31 in gallium). The difference in mass and implantation energy suggests that this is the reason that at a fluence of 1×10^{14} ions$\cdot cm^{-2}$ not enough energy is imparted to the Kapton at the surface region to cause damage observable by PALS, similar to the gallium implantation below a fluence of 1×10^{14} ions$\cdot cm^{-2}$.

The temperature dependent effects in general show increasing damage with implantation temperature, however in several of the sample preparation environments the Kapton implanted at room temperature exhibits less damage than this trend would predict. This behaviour is attributed to a "self-healing" property of the Kapton polyimide, where it has enough internal energy to recombine or reorganise to suppress damage. This effect is clear in the PALS lifetimes found at the damage layer in the RT prepared samples of gallium implanted Kapton, detailed in tables 7.4 and 7.5. The HT samples do not show the same self-healing effects as the implantation environment coupled with the energy of the ion beam is sufficient to overcome the effect. This self-healing ability could account for the stability of the physical properties exhibited by Kapton through a large temperature range [101, 102], although this effect is not as pronounced as some of the self-healing abilities of other similar organic materials which have been specifically designed with this purpose in mind [130, 131]. The observed self-healing effect here is a natural resistance the Kapton polyimide possesses.

The DBAR analysis of the oxygen implanted samples indicate that the room temper-

ature implantation varies significantly at the near surface and damage implantation layer, which also manifests in the observed PALS lifetimes. The changes in the momentum broadening curves are shown in figures 7.4, 7.5, 7.8, and 7.9, for the Kapton samples implanted with oxygen at 50keV. The momentum broadening curves for the Kapton samples implanted with oxygen at 100keV are shown in figures 7.12 and 7.13. The uncertainty in these graphs increases with increasing p_L (x axis), and is illustrated in figure 5.1. The change in the momentum broadening curve suggests that the oxygen implantation has different final products at the damage layer as compared to the near surface region which again varies depending on implantation temperature. The change in the the observed broadening fraction is consistent with the expectation that the oxygen ions will interact chemically with the Kapton polyimide chain, resulting in a different chemical environment at annihilation sites.

The S and W parameter depth profiling measurements that were made show large scatter within the data despite the smoothing of the data collected for each sample. Comparing figures 7.4 and figure 5.13 from the earlier chapter shows that the comparison of Kapton to damaged Kapton samples in these comparative ratio curves produces much lower deviations from the reference material; the maximum deviation is $\simeq 1.6$ for Kapton in ratio with aluminium but is only $\simeq 1.1$ for the RT sample in figure 7.4, which is damaged Kapton in ratio to the Kapton reference material. The lower proportion of high momentum electrons present in the constituent elements of the Kapton polyimide means that deviations from the reference spectra will be much smaller and explains the high relative scatter of the S and W parameters. The S and W parameter measurements show that the effects of the oxygen ion implantation are present to a deep level within the samples to a level beyond the calculated implantation depth, and that there could potentially be more information gained at additional measurements at a higher positron implantation energy that was performed. There is also some evidence that the samples prepared at 250°C (the HT samples) could be affected by the heating alone, as the S parameter is significantly below that of the standard at high positron implantation energies (and therefore deep within the sample where we expect no influence of the implanted ions). Figure 7.14 illustrates that even at 15keV positron implantation energy the S parameter for the HT sample is well below that of the Kapton standard used as a reference. Making

the distinction between annealing effects and the ion implantation is difficult without a reference sample of Kapton that has been annealed at 250°C , as the DBAR measurement will still analyse an increasingly large depth region of the Kapton as the positron implantation energy is increased, including the region of maximum damage, despite the majority of positrons annihilating at a deeper level with the material. This can change the S parameter despite the majority of positrons annihilating in the bulk of the Kapton. Temperature studies of Kapton in by Lua and Su [107] examine the transport properties of gases through Kapton as the polyimide is annealed above 350°C though they do not notice significant change in the gas transport until the polyimide has partially transitioned into amorphous carbon at temperatures higher than 250°C , and other studies do not observe changes to electrical properties after annealing Kapton at the same temperatures as used in this experiment [132]. The changes observed appear to be small at this level of implantation – observable by DBAR as it is a sensitive technique, but not large enough to present large scale changes to macroscopic properties.

To characterise the combination of chemical effects and ballistic damage caused by the oxygen implantation, the PAS data is compared to the gallium implanted samples of the same implantation fluence and across different implantation fluences by comparing the results from the same analysis region (near surface or maximum damage region).

Comparing the PALS results of the oxygen implanted Kapton to the gallium implanted samples at the near surface region shows changes to the damage patterns in the PALS results. The Kapton implanted with oxygen at 1×10^{14} ions$\cdot cm^{-2}$ has no observable lifetimes in the near surface region, which is an overall reduction in the induced damage as compared to the gallium implantation at the same fluence, which has a lifetime in the HT sample. The reduction in damage at the near surface region can be attributed to the ballistic and temperature differences in the implantation; the 300keV gallium ions implanted at 250°C impart enough energy in the near surface region of the Kapton to generate a defect large enough to be observed with PALS. The other gallium implanted samples at 1×10^{14} ions$\cdot cm^{-2}$ to not show any damage and nor do those implanted by oxygen at the same fluence.

The near surface region of samples implanted at 1×10^{15} ions$\cdot cm^{-2}$, both at 50keV and 100keV oxygen implantation energy, show different patterns to the samples implanted at

1×10^{14} ions·cm^{-2} as the higher fluence of implanted ions increases the over all damage: there are observable lifetimes in every gallium and oxygen implanted sample in the near surface region apart from the LNT sample implanted with 100keV oxygen ions. The RT samples implanted with oxygen at 1×10^{15} ions·cm^{-2} have the same observed lifetimes and very similar weightings as the gallium implanted samples. The lifetime observed in the LNT Kapton sample implanted with 50keV oxygen is much smaller than for the gallium implanted sample, but has a much larger associated weighting, suggesting that the interplay between the defect size and defect concentration has been reversed in between these two samples. The HT samples show larger lifetimes in the oxygen implanted samples with significantly reduced weightings. Both lifetimes have large associated uncertainties at approximately 20% giving only 2σ difference between both the HT 50keV oxygen lifetime and the HT 100keV oxygen lifetime in comparison to the HT gallium lifetime. As a result, we can conclude that the observed damage in the near surface region in both the gallium and oxygen implanted samples is therefore dominated by the ballistic effects of ion implantation, with little effect from chemical reaction with the implanted oxygen ions.

Comparison of the maximum damage region in Kapton implanted with oxygen to the gallium implanted samples reveals more about differences in the ballistic and chemical effects of the ion implantation, as the positron implantation will sample the layer in which the implanted ions come to rest within the Kapton. There are large differences in the maximum damage region of the Kapton implanted with oxygen and gallium at 1×10^{14} ions·cm^{-2}, the oxygen implanted samples have observable lifetimes at each preparation temperature whereas the gallium samples do not have an observed lifetime in the RT sample. The damage in the gallium implanted samples was characterised in terms of an observed "self-healing" effect, by which the RT sample exhibited less damage than the LNT sample, bucking the temperature dependent damage trend. This is notable as the damage did not follow the expected temperature dependence in lifetime nor weighting, which was constant across the HT and LNT samples. The oxygen implanted sample at 1×10^{14} ions·cm^{-2} also appears to follow the self-healing pattern, not in the observed lifetime but in the associated weighting, which is significantly higher than the gallium implanted samples at this fluence, while the observed lifetimes are constant at $\simeq 0.34$ns. The oxygen's effect here is a large increase to the overall damage, manifested in the weightings associated

with the lifetimes, which must be attributed to the oxygen chemically interacting with the Kapton polyimide chain. A similar pattern is present in the oxygen implantation at 1×10^{15} ions·cm^{-2}, however in this case the observed lifetimes are larger and associated weightings smaller than at 1×10^{14} ions·cm^{-2}, but still much larger than Kapton implanted with gallium at 1×10^{15} ions·cm^{-2}. Notably in both the low and high fluence oxygen implanted samples, the observed lifetime is the same as the gallium implanted counterpart – $\simeq 0.34$ns in the implantation at 1×10^{14} ions·cm^{-2} and $\simeq 0.43$ns in the implantation at 1×10^{15} ions·cm^{-2}. The reduction of lifetimes and weightings here is attributed to conversion of more of the sample to amorphous carbon, similar to the findings of Dlubek *et al.* [133] and others [110, 113]. Although the lifetimes and weightings are reduced, this is a greater amount of damage as the Kapton polyimide chain is being entirely degraded.

Comparing the Kapton implanted with 100keV oxygen at 1×10^{15} ions·cm^{-2} (tables 7.3 and 7.5) to the gallium implanted Kapton at 1×10^{15} ions·cm^{-2} (tables 7.10 and 7.11) at the maximum damage region is difficult as no lifetime was observed in the RT oxygen implanted sample at the damage region. The lifetimes and weightings in the oxygen implanted sample are significantly different to the gallium implanted sample and are more similar to the lifetimes and weightings in the Kapton samples implanted with 50keV oxygen at 1×10^{15} ions·cm^{-2}. This is further evidence for different processes occurring at the maximum damage region in the oxygen implanted samples compared to the gallium implanted samples. The lifetimes are found in the oxygen implanted samples are smaller than those in the gallium implanted sample at $\simeq 0.43$ns in the gallium implanted samples and $\simeq 0.35$ns in the oxygen implanted samples. The associated weightings are also significantly larger in the oxygen implanted samples however there appears to be a similar pattern – decreasing weighting with increasing implantation temperature. The weightings for the larger lifetimes in the gallium implanted samples is between $\simeq 3.5$ – 7.4% and between $\simeq 9.1$ – 12% in the oxygen implanted samples. Additionally, in the HT gallium sample there is a significantly larger lifetime at 1.0 ± 0.06ns however the oxygen implanted HT sample has the same lifetime as the LNT oxygen implanted sample (within experimental uncertainty). Therefore the chemical interaction of the oxygen ions with the Kapton is dominating any ballistic or temperature dependent effects in the creation of defects.

Overall, the addition of chemical interactions to the ballistic damage effects of ion implantation has had tangible impact to the induced damage. The oxygen implantation shows similar levels of damage as compared to implantation with higher energy gallium in the near surface region, and increased damage at the maximum damage region within the Kapton film, which is attributed to chemical interactions of the oxygen with the polyimide chain.

Chapter 8

Plasma Interaction with Kapton Polyimide Film

In this chapter the effects of plasma exposure of Kapton polyimide are explored. Data is presented for pristine and ion implanted Kapton exposed to plasma characterised using PALS and DBAR.

8.1 Sample Preparation and Experimental Set-up

To prepare the Kapton polyimide with ion implantation, commercially available Kapton HN film was implanted with oxygen ions using the low energy implanter at ANU [127], in the same manner as described in section 7.1. Samples were implanted with oxygen ions at 50 and 100keV at a fluence of 1×10^{15} ions$\cdot cm^{-2}$. The beam currents were kept below ∼150 nA, to stem any beam induced heating effects. After implantation, the samples were exposed to H_2 plasma using MAGnetized Plasma Interaction Experiment (MAGPIE) [128].

Prior to experiments the base pressure inside MAGPIE was 2.3×10^{-2} mTorr, while the operating pressure for the hydrogen plasmas was 10 mTorr. The hydrogen plasma was obtained by applying power to a copper antenna surrounding the source production region, at 1kW to perform plasma exposure to undamaged Kapton samples, and at 1.4kW for ion implanted Kapton samples. The plasma was then magnetically focussed into the plasma-material interaction region by using magnetic field of ≃600G. Under these operating conditions a plasma density of $\simeq 1 \times 10^{17} m^{-3}$ was obtained and an ion energy of ≃ 20eV [134]. To prevent overheating above 150°C , MAGPIE was operated in an cyclical manner of 10 minute periods of operation followed by 5 minute rest periods, up to the

total exposure time required.

8.2 Plasma Exposed Kapton

To begin the series of measurements exploring the effects of Kapton polyimide exposed to plasma using MAGPIE, pristine samples of commercially available Kapton HN film were exposed to plasma for a varying amounts of time, up to 10 minutes. Analysis was then conducted using PALS. The measurements made are detailed in table 8.1.

Plasma Exposure Time (minutes)	Positron Implantation Energy (keV)		
	1	2	5
0 (reference sample)	✓	✓	✓
1		✓	✓
2		✓	✓
5		✓	✓
10	✓	✓	✓

Table 8.1: Synopsis of PALS measurements made to plasma exposed Kapton polyimide film

No lifetimes were observed in any of the samples exposed to plasma using 2 and 5 keV positrons, therefore additional measurements were made using 1keV implanted positrons to analyse the region even closer to the surface. Positrons implanted with an energy of 1keV have a mean implantation depth of approximately 28nm using a Mahkov implantation profile detailed in section 2.3.1. The additional analysis at 1keV still did not result in any observed positron lifetimes.

The lack of induced lifetimes in the Kapton is unsurprising as the penetration depth of the H_2 plasma particles is very small as due to the low mass and relatively low energy of the Kapton-plasma interaction.

8.3 50keV Implanted Oxygen and Plasma Exposure

The samples characterised in this section were implanted with 50keV oxygen ions at a fluence of 1×10^{15} ions$\cdot cm^{-2}$ then were exposed to plasma.

PALS characterisation was performed with positron implantation energies of 2 and 3keV, to probe the near surface and region of maximum damage. The simulated positron implantation profiles compared to the oxygen implantation profile calculated with SRIM/TRIM

[67, 68] and pyPenelope [69] are shown in figures 7.1.

DBAR characterisation was performed as described in chapter 4. Depth profiling measurements were made with each DBAR spectra containing $\simeq 1 \times 10^6$ with positron implantation energies varying between 0.25 – 15keV. Detailed measurements were made with positron implantation energies at 2keV and 3keV, corresponding with the energies used for PALS characterisation, with $\simeq 16 \times 10^6$ total counts in the region of the 511keV annihilation photopeak.

2keV Implanted Positrons - Near Surface			
Fluence (ions·cm^{-2})	Implantation Temperature	Lifetime (ns)	Weight (%)
1×10^{15}	HT	0.76 ± 0.03	5.82 ± 0.19
	RT	0.51 ± 0.02	10.9 ± 0.4
	LNT	0.714 ± 0.017	6.14 ± 0.14

Table 8.2: Near surface PALS analysis of plasma exposed Kapton implanted with 50keV oxygen at 1×10^{15} ions·cm^{-2}, as probed by 2keV positrons.

3keV Implanted Positrons - Maximum Damage Region			
Fluence (ions·cm^{-2})	Implantation Temperature	Lifetime (ns)	Weight (%)
1×10^{15}	HT	0.66 ± 0.03	4.1 ± 0.2
	RT	0.43 ± 0.09	7 ± 1
	LNT	0.49 ± 0.01	9 ± 2

Table 8.3: Maximum damage region PALS analysis of plasma exposed Kapton implanted with 50keV oxygen at 1×10^{15} ions·cm^{-2}, as probed by 3keV positrons.

At the near surface region of these samples, the PALS analysis shows lifetimes at each ion implantation temperature. The lifetimes found in the HT and LNT samples (0.76±0.03 and 0.714 ± 0.017, respectively) are identical within experimental uncertainty (1.334σ). The lifetime observed in the RT sample is statistically different from both the HT and LNT samples (7.77σ and 6.93σ).

The weighting associated with each lifetime at the near surface region shows an inverse to the pattern in the lifetimes - the RT sample has the highest weighting associated with the lifetime indicating the highest defect concentration. The HT and LNT samples have weightings which are identical within experimental uncertainty (1.39σ).

From the PALS analysis at the maximum damage region the largest lifetime is observed in the HT sample at 0.66±0.03ns, followed by the LNT sample and the lowest lifetime in

the RT sample as shown in table 8.3. The relatively large uncertainty associated with the lifetime in the RT sample makes comparison difficult. The RT lifetime has an uncertainty of $\simeq$ 21% which is much higher than the HT and LNT samples ($\simeq$ 4.5% and $\simeq$ 2.0% uncertainty respectively). Comparing the lifetime in the RT and LNT with a two-tailed test gives a difference of 0.66σ suggesting that the two lifetimes are the same within experimental uncertainty.

There is also large uncertainty in the weighting of each lifetime, again making comparison difficult. The weightings increase with decreasing ion implantation temperature however the large uncertainties in the LNT and RT weightings imply that there is no meaningful difference. The weightings in the HT and RT samples are 2.7σ apart, and the weightings in the HT and LNT samples are 2.3σ apart. The weighting in the RT and LNT samples are the same within experimental uncertainty.

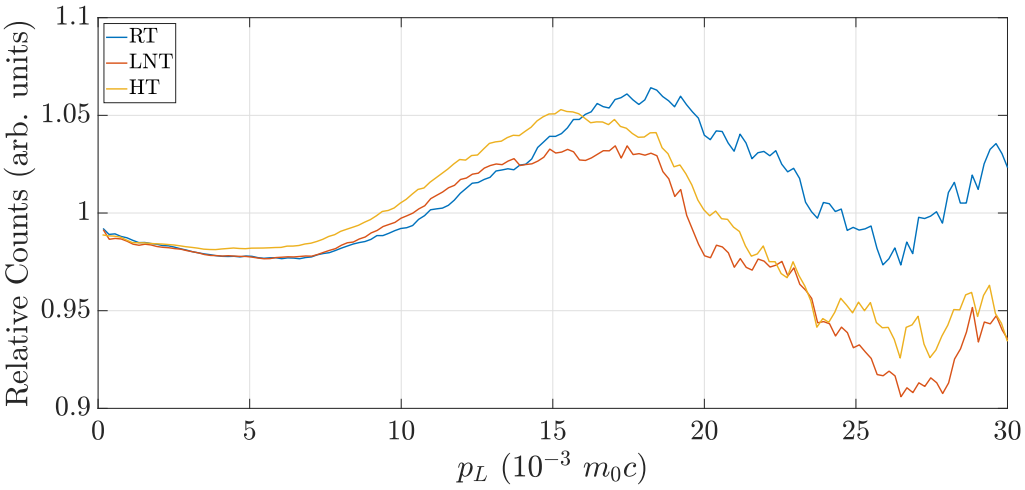

Figure 8.1: Near surface momentum distribution of plasma exposed Kapton implanted with 50keV oxygen at 1×10^{15} ions$\cdot cm^{-2}$, as measured by DBAR from positrons implanted at 2keV.

The momentum distributions of the annihilation photons in ratio to the Kapton reference sample are illustrated in figures 8.1 and 8.2. In both the near surface and maximum damage region the HT and LNT samples show similar line shapes. The significant difference between the two ratio curves is an increased maximum at $\simeq 15p_L$ between the near surface and maximum damage region. Above $15p_L$ both the LNT and HT samples show decreasing trends. The difference between the LNT and HT samples is less at the near surface region than the maximum damage region.

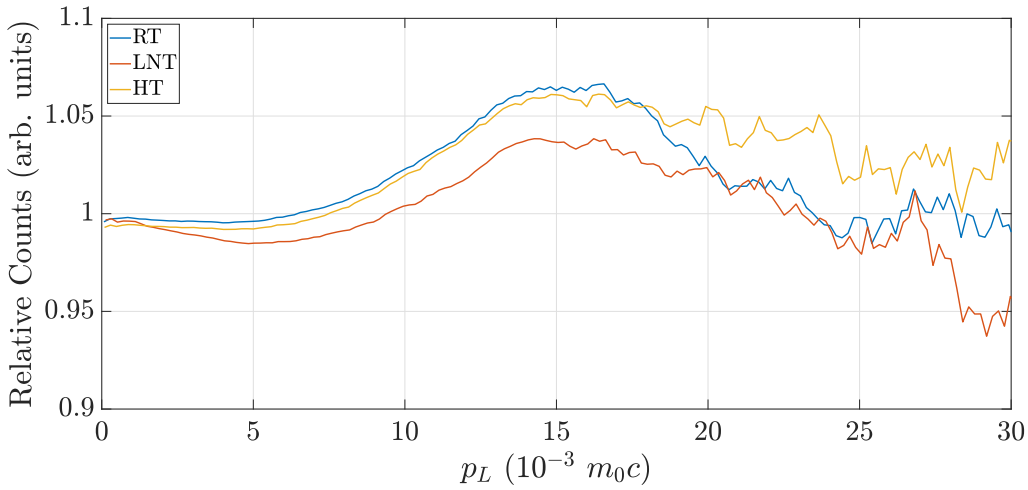

Figure 8.2: Maximum damage region momentum distribution of plasma exposed Kapton implanted with 50keV oxygen at 1×10^{15} ions·cm^{-2}, as measured by DBAR from positrons implanted at 3keV.

The RT sample's DBAR ratio curve changes significantly between the near surface and maximum damage region. In the near surface region the curve closely follows the LNT sample but with a higher maximum at larger p_L of $\simeq 17p_L$ compared to $\simeq 15p_L$ for the LNT sample. Above $15p_L$ the RT sample shows much a larger broadening ratio than the LNT and HT samples. At the damage layer, the sample prepared at RT has a ratio curve much closer to that of the HT sample.

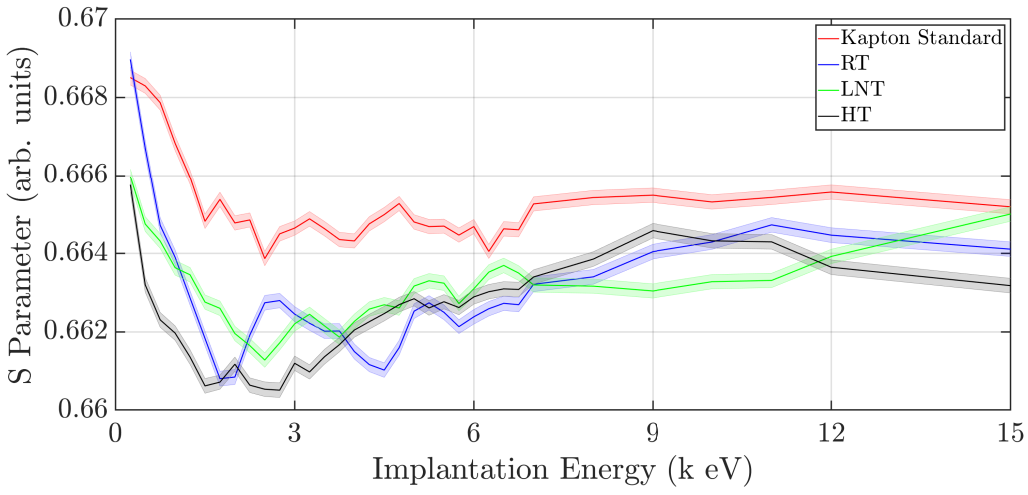

Figure 8.3: S parameter as a function of positron implantation energy in plasma exposed Kapton implanted with 50keV oxygen ions, at 1×10^{15} ions·cm^{-2}. The original data has been smoothed by a 3-point moving average to produced the curve and the shaded area represents the uncertainty associated with the central line.

The S and W parameter depth profiling curves (figures 8.3 and 8.4) are similar for the

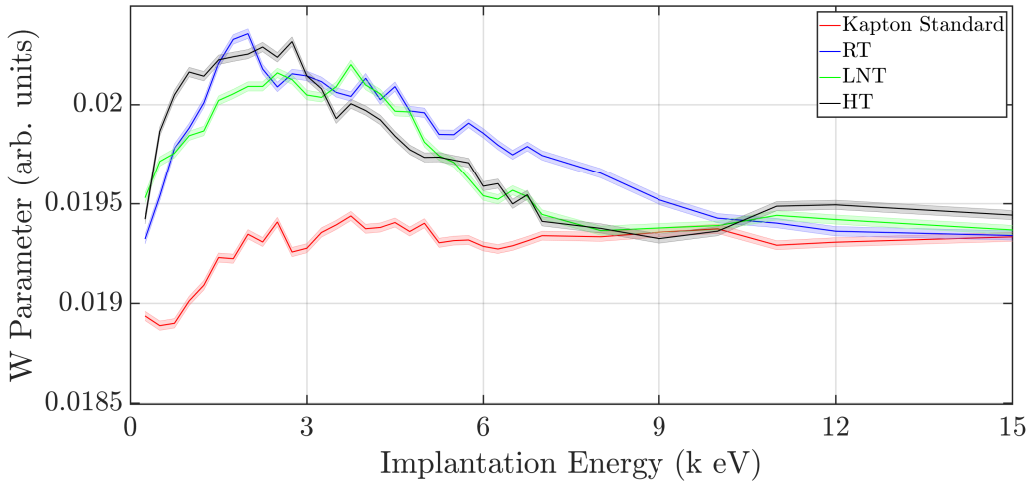

Figure 8.4: W parameter as a function of positron implantation energy in plasma exposed Kapton implanted with 50keV oxygen ions, at 1×10^{15} ions$\cdot cm^{-2}$. The original data has been smoothed by a 3-point moving average to produced the curve and the shaded area represents the uncertainty associated with the central line.

LNT and HT samples, but the RT sample has several differences.

In the S parameter plot the RT sample starts at 0.25keV positron implantation energy with an S parameter value approximately that of the reference sample, before reaching values similar to both the LNT and HT sample from approximately 2keV positron implantation energy and higher.

In the W parameter plot the RT sample has a similar value to the LNT and HT samples until approximately 6keV positron implantation energy, at which point the RT sample's W parameter remains greater than the LNT and HT samples, which are in line with the reference sample.

The differences in the RT sample seen in the DBAR analysis aligns with the differences seen in the PALS analysis at the near surface (the RT sample is significantly different to both the LNT and HT samples, which are similar to one another), however there is no PALS data at the 6 - 9keV positron implantation energy to investigate the difference in the RT sample at that depth, which corresponds to a mean implantation depth of $\simeq$ 558nm (calculated by a Mahkov implantation profile detailed in equation (2.4)). This depth is far beyond the range of the ion implantation range suggested by the simulations conducted in SRIM/TRIM and shown in figure 7.1.

The DBAR measurements of the HT sample at 3keV cannot explain the difference in the lifetime and associated weighting in comparison to the two lifetimes as the ratio curve

in figure 8.2 and the depth profiled S and W parameters show values similar to those of the RT sample. The lack of difference in the DBAR data implies that the the same type of defect with the same chemical environment is created in the RT sample and HT sample, but in the HT sample the defects are larger yet in a lower concentration.

The DBAR analysis shows that a different chemical environment is present in the LNT samples as measured by 3keV positrons, however the lifetime is equal to that of the RT sample within experimental uncertainty. This apparent equality in lifetimes is in part due to the large ($\simeq 20\%$) uncertainty in the RT sample's observed positron lifetime, which results in a statistical difference of 0.66σ in comparison to the LNT positron lifetime.

8.4 100keV Implanted Oxygen and Plasma Exposure

The Kapton samples in this section were implanted with 100keV oxygen ions at a fluence of 1×10^{15} ions$\cdot cm^{-2}$ before being exposed to plasma. The sample characterisation was performed in the same manner as described in the previously, section 8.3. The positron implantation energies for the PALS and detailed DBAR characterisation were 2keV and 4.25keV to analyse the near surface and maximum damage regions respectively, and the oxygen and positron implantation profiles are shown in figure 7.2. The results from the near surface PALS analysis are presented in table 8.4, and the PALS analysis of the maximum damage region is presented in table 8.5.

The PALS analysis of the 100keV oxygen implanted Kapton film exposed to plasma shows markedly different results to plasma exposed Kapton implanted with oxygen at 50keV. The HT sample shows no induced lifetimes at the near surface or maximum damage region. The LNT sample shows a lifetime at only the near surface region.

At the near surface region the weightings in the RT and LNT samples are identical within experimental uncertainty (0.32σ difference) but the lifetimes are statistically different (3.49σ) this implies the RT sample has less damage than the LNT sample, in the near surface region.

Only one lifetime was found by probing the maximum damage region with 4.25keV positrons, which was 0.43 ± 0.02ns observed in the RT sample. No lifetimes were observed in the LNT or HT samples.

The ratio curves from the DBAR analysis show large differences near the surface region,

2keV Implanted Positrons - Near Surface			
Fluence (ions·cm^{-2})	Implantation Temperature	Lifetime (ns)	Weight (%)
1×10^{15}	HT	-	-
	RT	0.30 ± 0.04	9 ± 3
	LNT	0.465 ± 0.016	8.5 ± 0.4

Table 8.4: Near surface PALS analysis of plasma exposed Kapton implanted with 100keV oxygen at 1×10^{15} ions·cm^{-2}, as probed by 2keV positrons.

4.25keV Implanted Positrons - Maximum Damage Region			
Fluence (ions·cm^{-2})	Implantation Temperature	Lifetime (ns)	Weight (%)
1×10^{15}	HT	-	-
	RT	0.43 ± 0.02	4.8 ± 0.3
	LNT	-	-

Table 8.5: Maximum damage region PALS analysis of plasma exposed Kapton implanted with 100keV oxygen at 1×10^{15} ions·cm^{-2}, as probed by 4.25keV positrons.

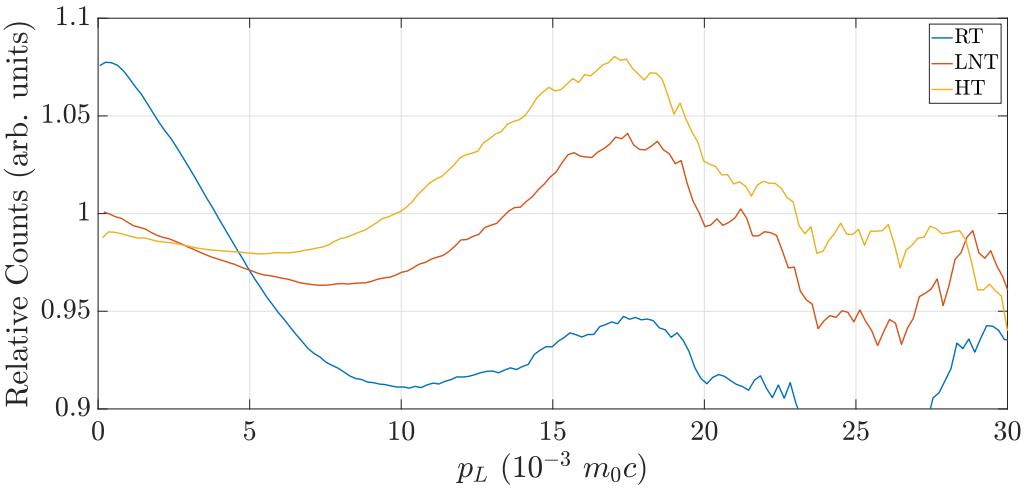

Figure 8.5: Near surface momentum distribution of plasma exposed Kapton implanted with 100keV oxygen at $1{\times}10^{15}$ ions·cm^{-2}, as measured by DBAR from positrons implanted at 2keV.

as probed by 2keV positrons and shown in figure 8.5, the curve for the RT sample shows a completely different shape to the LNT and RT samples and the LNT and HT samples are similar to one another. The RT sample shows more annihilation at low p_L in comparison to the reference sample of pristine Kapton indicating more positrons are annihilating with low momentum electrons. The LNT sample at the near surface region starts at $\simeq$1 at $0p_L$ — the same as the reference sample — however less positrons annihilate with mid-range momentum electrons between 0–$12p_L$. The HT sample shows less positrons annihilating

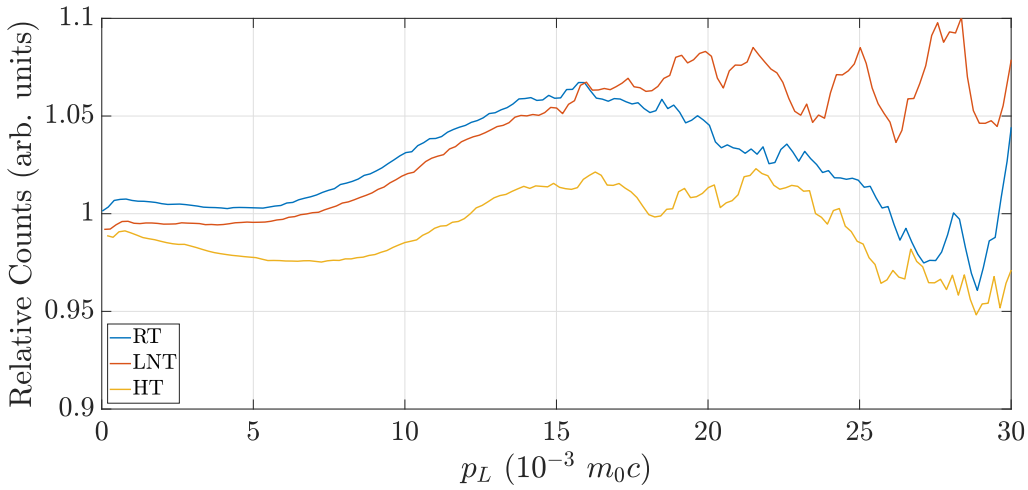

Figure 8.6: Maximum damage region momentum distribution of plasma exposed Kapton implanted with 100keV oxygen at $1{\times}10^{15}$ ions·cm^{-2}, as measured by DBAR from positrons implanted at 4.25keV.

with low energy electrons and much more annihilation with higher energy electrons, as show by the peak at $\simeq 17p_L$.

At the damage layer, shown in figure 8.6, each sample shows a similar curve shape between 0–$15p_L$, offset by one another in the y-axis. The HT sample shows the least change from the reference and is below the RT and LNT samples, and the RT and LNT samples are similar in shape to one another. From 0–$5p_L$, the LNT sample is very close to the Kapton reference sample and the RT sample is consistently above the reference.

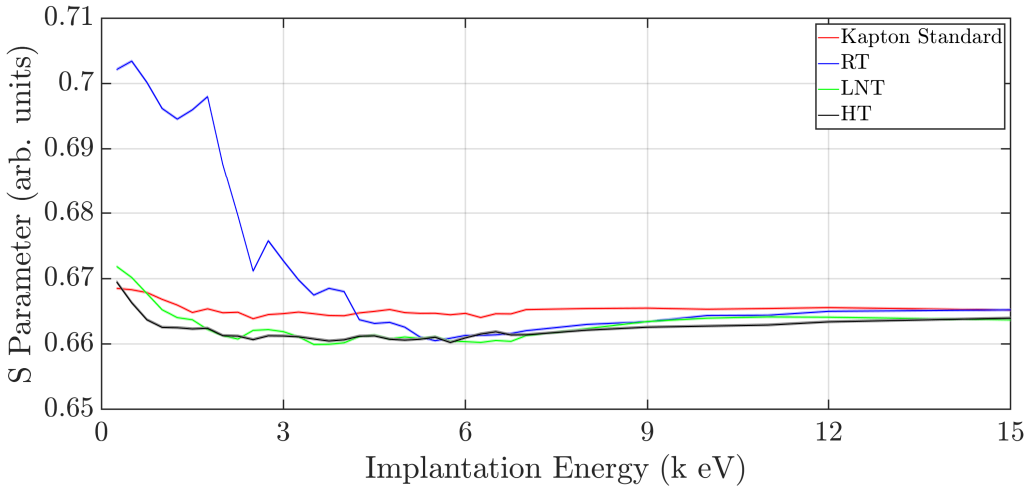

Figure 8.7: S parameter as a function of positron implantation energy in plasma exposed Kapton implanted with 100keV oxygen ions, at 1×10^{15} ions·cm^{-2}. The original data has been smoothed by a 3-point moving average to produced the curve and the shaded area represents the uncertainty associated with the central line.

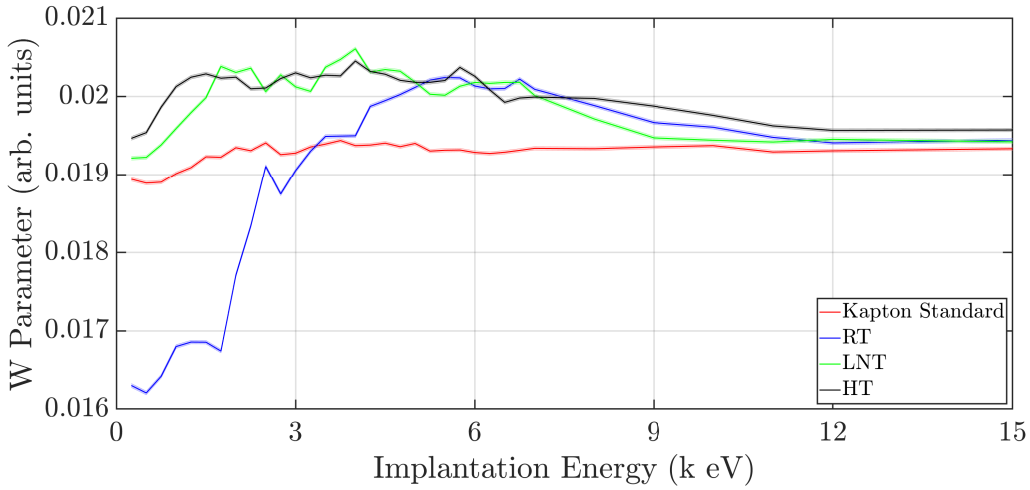

Figure 8.8: W parameter as a function of positron implantation energy in plasma exposed Kapton implanted with 100keV oxygen ions, at 1×10^{15} ions·cm^{-2}. The original data has been smoothed by a 3-point moving average to produced the curve and the shaded area represents the uncertainty associated with the central line.

Comparing the S-parameter as a function of depth between the 3 samples, shown in figure 8.7, it is very clear how different the RT sample is compared to the LNT and HT samples. At approximately 5keV the S-parameter profile matches the patterns of the LNT and HT samples.

In the W parameter depth profile plot (figure 8.8), the W parameter remains significantly greater than the reference in all the damaged samples at positron implantation energies between 6–8keV. The effects of the 100keV oxygen ion implantation have an effect on the Kapton to a deep level, past the mean implantation range suggested by the simulations conducted in SRIM/TRIM and shown in figure 7.2. This was also observed in the 100keV oxygen implantation into Kapton *without* the subsequent plasma exposure, and the sample implanted with oxygen at 50keV and exposed to plasma. The S parameter at this depth within the sample is similar to that of the reference material.

8.5 Discussion

Exposing the Kapton samples to H_2 plasma using MAGPIE has had a clear effect on the damage as demonstrated by PALS and DBAR analysis, particularly in the RT sample at the near surface region and at all temperatures at the maximum damage region.

The colour change that was observed in the ion implanted Kapton in chapter 7 is

again observed, the samples show a darkening in the implanted region like the other ion implanted Kapton samples, as described in section 7.5. The amount of change in the sample colour in the ion implanted Kapton that has also been exposed to plasma follows the same pattern as before, however the Kapton samples that were exposed to plasma alone do not show any change in colour.

To aid in comparison across the samples, tables 8.6, 8.7, contain the number of standard deviations lifetimes and weightings are apart from the corresponding measurement in the samples with and without plasma exposure. The standard deviation for comparison are calculated using equation 8.1:

$$\text{Number of standard deviations, } \sigma = \frac{|x_1 - x_2|}{\sqrt{\sigma_{x_1}^2 + \sigma_{x_2}^2}} \tag{8.1}$$

where x_i is the measurement value, and σ_{x_i} is the associated uncertainty in the value x_i.

Implantation Region →		Near Surface		Maximum Damage	
Fluence (ions·cm^{-2})	Implantation Temperature	Lifetime (no. σ)	Weight (no. σ)	Lifetime (no. σ)	Weight (no. σ)
1×10^{15}	HT	− 2.1	+ 9.1	+ 6.4	− 15.6
	RT	− 3.16	+ 12.6	0	− 4.7
	LNT	+ 8.9	− 6.0	+ 0.9	− 4.4

Table 8.6: Comparison of the PALS analysis in plasma exposed Kapton samples which have been implanted with 50keV oxygen ions at 1×10^{15} ions·cm^{-2}. An increase or decrease in the observed lifetime or weighting in the plasma exposed sample is indicated by a + or − respectively.

Implantation Region →		Near Surface		Maximum Damage	
Fluence (ions·cm^{-2})	Implantation Temperature	Lifetime (no. σ)	Weight (no. σ)	Lifetime (no. σ)	Weight (no. σ)
1×10^{15}	HT	− 5	− 9.1	− 19	− 13
	RT	− 5.5	+ 1.5	+ 21	+ 16
	LNT	+ 29	+ 21	− 21	− 13

Table 8.7: Comparison of the PALS analysis in plasma exposed Kapton samples which have been implanted with 100keV oxygen ions at 1×10^{15} ions·cm^{-2}. An increase or decrease in the observed lifetime or weighting in the plasma exposed sample is indicated by a + or − respectively.

The change in size of the observed PALS lifetimes and the change in the associated weighting again show a pattern of interplay between increasing lifetime and decreasing weighting. For example, in the the HT sample of Kapton implanted with oxygen at 50keV

at the near surface (detailed in table 8.6), the lifetime in the implanted sample exposed to hydrogen plasma is smaller than the sample without plasma exposure, however the associated weight has increased in the plasma exposed sample. The reverse relationship is true for this HT sample in the observed positron lifetimes at the maximum damage region. The only instances of both observed values increasing or decreasing occurs when comparison is between a sample that has no observed lifetime and one that does, such as the HT sample implanted with 100keV oxygen ions (detailed in table 8.7).

In the 50keV oxygen implanted Kapton at the near surface region the HT sample shows a similar lifetime with and without plasma exposure (2.1σ shown in table 8.6) however the uncertainty in the lifetime in the non-plasma exposed sample is very large at $\simeq 18\%$ and approximately 7 times larger than the lifetime in the plasma exposed sample, making comparison difficult. In the HT and RT samples the lifetimes have decreased in comparison to the equivalent samples that have not been exposed to plasma and the associated weightings have increased. The LNT sample exhibits the opposite trend.

At the damage region in the 50keV implanted samples, both the RT and LNT samples have positron lifetimes that are identical within experiment uncertainty and each measurement has comparable uncertainty values. The HT sample has significant differences: the plasma exposed sample has a much larger lifetime (0.43 ± 0.02ns compared to 0.66 ± 0.03ns with plasma exposure, 6.4σ difference), but a much lower weighting ($20 \pm 1\%$ compared to $5.82 \pm 0.19\%$ with plasma exposure). The general trend at this region is a decrease in the weightings associated with the observed positron lifetimes. The much larger lifetime in the plasma exposed HT sample suggests that the plasma exposure has a deep reaching effect in the Kapton, further past the natural penetration depth of the plasma alone. The increased lifetime (detailed in table 8.3) and the change in DBAR momentum distribution (detailed in figures 7.9 and 8.2) show a larger defect of different chemical composition in the plasma exposed sample.

At the near surface region of the Kapton implanted with oxygen at 100keV, shown in table 8.7, only the RT sample exhibits a lifetime measurable with PALS analysis in both the plasma and non-plasma exposed samples. The samples prepared without plasma exposure have lifetimes at HT and RT, but not LNT, whereas the sample exposed to plasma has observable lifetimes at RT and LNT and not in the HT sample. The lifetime

in each RT sample is very different, however the uncertainty in the weighting for the plasma exposed sample is $\simeq 30\%$, making the two weightings only 1.5σ apart using a two-tailed comparison. The other values presented in table 8.7 are a comparison to a lifetime of 0ns with a weighting of 0%, where no lifetime was observed in a sample.

At the damage region of the 100keV oxygen implanted Kapton the sample exposed to plasma only the RT sample has an observed positron lifetime, whereas in the non-plasma exposed sample there are lifetimes in only the HT and LNT samples.

The exposure of oxygen implanted Kapton to H_2 plasma has had various effects to the damage induced by the ion implantation, without strong evidence for a consistent pattern. The depth profiling of the samples using the DBAR method has shown a large difference in the RT in particular in the cross-comparison between plasma and non-plasma exposed samples, as well as the patterns of sample preparation temperature established in chapter 7. The stark change implies that the plasma exposure causes different chemical products through interaction of the plasma with the damage Kapton polyimide chain. The observed changes in the damage as analysed by the PAS techniques show that there are differences up to the region of maximum damage in the Kapton, which is significantly deeper than the plasma components could penetrate alone. The exposure of Kapton to plasma alone did not produce an observable lifetimes through PALS analysis.

In the RT implanted with 100keV oxygen ions and exposed to plasma, the very high S parameter (as shown in the DBAR depth profiling in figure 8.7) is from positrons annihilating with electrons with low momentum, indicating that the chemical structure has change significantly due to the way this sample was prepared. This suggests that the hydrogen from the plasma is bonding with the damaged polyimide chain, providing this "low momentum" environment. Additionally, the bonding of the hydrogen to damage sites explains the lack of observed lifetimes as the hydrogen from the plasma can travel through the defect network and fill in the available open volume.

An important factor to consider in the analysis and comparison of the plasma exposed samples is that the experimental conditions for the plasma exposure also heats the sample. The preparation of the plasma exposure was conducted in such a way as to keep the temperature below 150°C to prevent damage to the MAGPIE experimental apparatus, however this temperature could have induced further damage effects into the Kapton, or

changed the damage from the oxygen implantation. The Kapton specification states that a second order transition occurs between 360°C and 410°C , and a shrinkage of 0.17% at 150°C and 1.25% at 400°C [101,102]. Ordinarily the temperature of 150°C in the Kapton polyimide would not produce as significant effects as have been observed, however the ion implantation preceding the plasma exposure and additional heating to 150°C could have caused enough damage to the Kapton that this relatively low temperature is enough to exacerbate the effects of the plasma exposure.

The lack of any observed positron lifetimes in several of the plasma exposed samples, despite some evidence of damage from DBAR analysis, could be due to several factors. As previously discussed in the results of chapter 7, there is a progression towards an amorphous carbon or carbonised phase of the Kapton due to the high levels of induced damage, which is also seen in other ion implantation studies [110, 113, 133]. A similar phenomenon appears to be occurring in the samples exposed to plasma — the formation of stable defects is not possible due to excessive damage in the Kapton sample from the ion implantation and plasma exposure.

An alternative explanation to the lack of observed lifetimes is that the induced defects are filling with hydrogen from the exposure to plasma. This would account for the lack of observed lifetimes in some of the Kapton samples implanted with oxygen ions at 100keV and exposed to plasma. In particular, the large defects observed in the HT sample without plasma exposure which are not present in the equivalent plasma exposed HT sample could be exhibiting this defect filling behaviour.

The pattern of interaction of the hydrogen plasma with the Kapton samples implanted with oxygen at 100keV is complicated to directly identify, and it seems likely that there is a combination of defect filling and defect recombination due to excessive damage.

The large weightings associated with the positron lifetimes that has been attributed to chemical interaction of Kapton and oxygen at the region of maximum damage (presented in the tables 7.7 and 7.9) are not present in the equivalent plasma exposed samples (presented in tables 8.2 and 8.3). In the Kapton implanted with oxygen ions at 100keV, there is a similar range of weightings between $\simeq$ 1.5–12% in samples with and without exposure to plasma.

There is continued evidence in the plasma exposed samples to suggest the effects of the

damage due to ion implantation (and therefore changes to this damage through exposure to plasma) persists to a depth within the samples greater than suggested by the range of the implanted ions. There are significant differences in the S and W parameters of the all samples in this chapter as probed by 6keV positrons, which is mean implantation depth of approximately 558nm. This is much greater than the mean implantation range of oxygen ions at either 50keV or 100keV, which correspond to mean implantation ranges of approximately 190nm and 350nm respectively. Comparison of the S and W parameter plots for the ion implanted Kapton samples (figures 7.10, 7.11, 7.14, and 7.15) and those of the plasma exposed samples (figures 8.3, 8.4, 8.7, and 8.8) show that the evidence for damage past the mean implantation depth is greater in the samples that have been exposed to plasma.

Plasma exposed Kapton (without ion implantation) has no damage observable with PALS, however the exposure of oxygen ion implanted Kapton to plasma significantly changes the observed damage from the ion implantation alone and affects the Kapton to a deeper penetration depth. There is evidence indicating chemical interaction between the hydrogen plasma with the damage sites in the Kapton and the types of interaction are influenced by the temperature effects in the sample preparation.

Chapter 9

Conclusion

In this chapter, the outcomes of the development of the DBAR spectroscopy technique and analysis of damaged Kapton polyimide are discussed in reference to the goals set out for this thesis in the introduction, chapter 1.

9.1 DBAR Experiment

The initial section of the work presented in this thesis was the development of the DBAR measurement technique. The DBAR experiment was an additional, complementary measurement added to the established positron materials beamline used by the positron group at the Australian National University.

Although the DBAR experiment was implemented successfully, it was implemented using an analogue measurement technique rather than the initially proposed fully digital method. Throughout chapter 4, attempts were made to improve the effective resolution of the digital measurement through application of enhancements to the curve fitting routine used as part of the analysis of the digital data and digital filtering applied to the waveforms collected from the HPGe detector apparatus. Significant improvements to the resolution were made using these methods which emphasises the paradigm set out by digital measurements; with digital data collection, data can be re-analysed when suitable new techniques have been developed, which can lead to better results. As the digital measurement did not meet the requirements for implementing the DBAR technique, it was ultimately implemented using a more traditional analogue measurement which met the energy resolution requirements. The experimental apparatus was characterised using radioactive check sources with well known properties, and a measurement of the background radiation environment in the laboratory was made.

As part of the characterisation of the DBAR technique spectrum post-processing was implemented on the spectra collected for DBAR measurements. The post-processing reduced the effects of the background in the region of the 511keV photopeak from sources such as 3 photon positron annihilation and incomplete charge collection in the HPGe detector. The implementation of this post-processing improved the quality of the DBAR spectra beyond that traditionally expected from a single detector DBAR measurement.

Following its characterisation, the DBAR experiment was used to examine the differences in the observed broadening in different material samples, including high purity elemental samples and a small selection of organic materials. The experiment was successfully able to detect differences in the DBAR spectra due to the different atomic configurations in the elemental samples, as well as differences in the organic materials. The results were used to reproduce the work of Asoka Kumar *et al.* which provided a good evaluation of the capabilities of the DBAR experiment in comparison to the higher resolution coincidence measurement originally used.

9.2 Space Relevant Damage in Kapton Polyimide Film

A series of damage experiments were conducted to simulate facets of the harsh conditions that spacecraft insulators are exposed to through long term interplanetary missions. Damage to Kapton polyimide film was conducted using ion implantation at three different implantation temperatures using gallium and oxygen ions, and samples were additionally exposed to plasma.

Characterisation of the induced damage was done through PALS and DBAR and the results interpreted in terms of temperature dependent effects, ballistic and chemical damage from the ion implantation, and the effects of exposure to hydrogen plasma. The results of the PAS techniques were analysed in comparison to a pristine sample of the Kapton film used; in the PALS measurements the pristine Kapton was used as an instrument function, and in the DBAR measurements the reference Kapton sample was use in two ways. The momentum broadening curves were taken in ratio to the DBAR measurement of the pristine sample and depth-profiling data was directly compared to the depth profiled pristine Kapton sample.

9.2.1 Ion Implantation into Kapton Polyimide Film

The characterisation of the damage using the positron sensory techniques showed the evolution of the Kapton polyimide into a region of amorphous carbon across the implantation region, which is attributed to the breaking of $C-O$ and $C-N$ bonds.

The observed damage effects from ion implantation increased with implantation fluence in both the oxygen and gallium implanted Kapton samples. Gallium implantation at fluences at 1×10^{12} and 1×10^{13} ions$\cdot cm^{-2}$ did not have any observed PALS lifetimes. The gallium and oxygen implanted samples exhibited positron lifetimes at an implantation fluence of 1×10^{14} ions$\cdot cm^{-2}$, the near surface region showed less damage than ion implantation layer.

The detailed PAS characterisation was conducted by implanting positrons to the near surface and maximum damage regions, which were determined by simulation. Less precise DBAR depth profiling was conducted to higher positron implantation energies, to a depth within the Kapton past the simulated effects of ion implantation. The results of the S and W analysis in the deep region of the samples shows that the ion implantation has measurable effects significantly further than the calculated ion implantation range.

Temperature dependence in the damage quantity was observed, samples that were implanted at higher temperatures exhibit the most damage, followed by implantation at liquid nitrogen temperatures, and the least damage was observed in samples prepared at room temperature. The lower damage at room temperature is attributed to a "self-healing" effect which occurs as there is enough energy in the Kapton matrix to recover from some of the damage to the polyimide chain through recombination of broken chemical bonds, or for the polyimide chains to move into voids created by the implantation. In the samples prepared at liquid nitrogen temperature the energy required to recover from this damage is not present, therefore the resulting damage from implantation is higher. The high preparation temperature results in an implantation environment with sufficient energy to increase the damage from the ion implantation to a level that the Kapton polyimide molecules are unable to overcome through recombination or reordering.

The differences in the observed positron lifetimes between the oxygen and gallium implanted Kapton samples indicate that there are different chemical environments in the defects generated from the ion implantation. The changes in the depth profiled DBAR

spectra as well as differences in the momentum distribution curves at the near surface and implantation regions show that there are different defects in the near surface region (from ballistic effects) and the region of maximum damage (from chemical interactions of the oxygen ions).

The analysis of the near surface region of the samples show that the ballistic damage from the oxygen ions is less than that of the gallium ions, which is as expected due to the mass difference between the two ion species.

At the region of maximum damage the oxygen implanted samples exhibit different defects which is attributed to the chemical interaction between the Kapton polyimide chain and the implanted oxygen. Oxygen will readily react with all of the constituent elements in the Kapton polyimide chain opening the possibility for chemical interaction between the implanted oxygen ions when they come to rest within the Kapton film. After ballistic damage has taken place from the oxygen implantation, portions of the Kapton chain that have been forcibly separated due to broken chemical bonds could form new bonds with the implanted oxygen.

9.2.2 Plasma Interaction with Kapton Polyimide Film

The effects of plasma damage in Kapton were explored by exposing pristine and ion implanted Kapton to hydrogen plasma and characterisation of these samples was performed using PALS and DBAR.

The pristine Kapton samples were exposed to plasma for varying amounts of time and were investigated using PALS. No positron lifetimes were observed as a result of the plasma exposure. However, the plasma exposure had significant effect on the ion implanted Kapton samples and large changes were observed in the positron lifetimes and the chemical environment at positron annihilation sites, as measured by DBAR.

The plasma exposure had a significant effect on the ion implanted Kapton samples at both the near surface and the maximum damage region. Changes in the positron lifetimes observed with and without plasma exposure suggest that there is interaction between the hydrogen and the defects induced by ion implantation. The changes in the observed positron lifetimes and their associated weightings were inter-related; where positron lifetimes increased in the plasma exposed samples, the associated weighting typically de-

creased, and the reverse relationship occurred for decreasing positron lifetimes.

The pattern of positron lifetimes observed in the samples shows that the effects of the plasma exposure depend on the preparation of the Kapton, which is consistent with the temperature dependent effects observed in the gallium and oxygen implanted Kapton that were not exposed to plasma.

The PAS characterisation of the plasma exposed samples shows evidence that damage effects are increase through exposure to Kapton and defect filling with hydrogen appears to be taking place. The combination of these two effects complicates the analysis of the PAS results as several of the samples have no observed positron lifetimes but show significant damage from the DBAR analysis. Comparison between the samples with and without plasma exposure show that the temperature of the Kapton during ion implantation has an impact on the defect filling due to the temperature dependence in the damage products, which are present in the Kapton before the exposure to plasma.

Similarly to the ion implanted samples that were not exposed to plasma, the depth profiling DBAR measurements show damage effects past the depth indicated by the ion implantation simulation. In the samples exposed to plasma, these deep level damage effects are greater than that of the samples without plasma exposure.

The data collected suggests that the plasma exposure allows the already damaged Kapton matrix to readily react with the hydrogen present in the plasma, resulting in a significantly different chemical environment than would be present from the effects of ion implantation alone. The change in PAS results due to plasma exposure at the ion implantation damage region shows that the plasma exposure can effect change several hundred nanometres below the Kapton surface. The hydrogen introduced would bond with any dangling bonds remaining in the damaged Kapton matrix due to ion damage.

9.3 Future Work

The work presented in this thesis has several potential extensions, including expansion of the experimental apparatus and additional measurements of damage Kapton.

9.3.1 Positron Materials Beamline

The integration of the Doppler broadening of annihilation radiation measurement was successful in providing complementary measurements to the positron annihilation lifetime spectroscopy measurement that was already operational on the positron materials beamline, which expanded the characterisation ability of the experiment. Despite the enhancements to the experimental resolution using mathematical post-processing on the collected DBAR spectra, there is still a significant signal background, particularly in the region where the detected annihilation photon has an energy $E < 511$keV. To improve this the fast BaF_2 detector used in PALS measurements could be used as a secondary detector in order to create a partial coincidence measurement in the DBAR experiment. The BaF_2 detector would not be able to collect information on the detected photon energy, but it would be located in a collinear arrangement with the High-Purity Germanium detector, to detect two photon products of positron-electron annihilation, and thus greatly reduce the three photon background currently being detected. A side effect of this coincidence configuration would be a reduction in the count rate of the DBAR measurement due to the significantly decreased solid angle acceptance to ensure that photons from the same annihilation event are detected properly.

Once a coincidence measurement has been implemented, using the trapped beam for measurements to combine the PALS experiment with the partial coincidence DBAR measurement would result in the creation of an AMOC system. As described in section 2.6, an AMOC measurement would provide further information from positron-electron annihilation events linking the DBAR and PALS measurement techniques together. The count rate reduction would be alleviated by continuing a mixed programme of measurements — pure DBAR measurements for relatively rapid depth profiling of a particular sample, with slower AMOC measurements conducted at depths within the sample that appear particularly interesting.

9.3.2 Expanded Characterisation of Damaged Kapton

The analysis of damaged Kapton using PALS and DBAR has revealed much about the damage products that occur in the sample from the damage experiments that were performed, however other characterisation techniques can provide more specific information

on these products and therefore provide even greater insight into the processes at work.

Raman spectroscopy is a good candidate to characterise the chemical structures that are present in the damage Kapton [135], as well as Fourier Transform Infra-Red (FTIR) spectroscopy [136]. These techniques can be used to identify the chemical bonds present in a material and can be used to compare the relative abundance of these bonds between different sample preparations and this has been successfully applied to study damage in Kapton [114, 116, 137]. Applying these techniques would allow the chemical environment to be analysed further throughout the damaged Kapton samples and assist in relating the DBAR momentum distribution information that was observed to the information about the chemical bonds determined through Raman spectroscopy or FTIR.

Gallium was used as an implanted ion to investigate the effects of ballistic damage from the implantation with a lower contribution of chemical interaction between the Kapton and the implanted ion. Gallium is relatively heavy compared to the other elements in the Kapton polyimide chain, therefore an investigation into ballistic damage using a lighter ion than gallium may give results which have a stronger relationship to the damage caused through oxygen implantation. Candidate ions for this study could be silicon, to use an element which is not present in the Kapton polyimide, or carbon, which would have some chemical interaction with the polyimide chain as it makes up approximately 56% (stoichiometrically) of the Kapton molecule.

In addition to using an alternative implanted ion to study the damage effects from implantation, further understanding of the relationship between the implanted ion dose and resultant damage could be obtained by the characterisation of Kapton samples implanted at "intermediate" fluences, such as 5×10^{14} and 5×10^{15} ions$\cdot cm^{-2}$. This is of interest as there were no observed lifetimes in some of the Kapton samples prepared with an implanted fluence of 1×10^{14} ions$\cdot cm^{-2}$. Finding the threshold at which defects become observable to PAS measurements would provide an idea of the mission length at which the damage effects observed in the laboratory become significant to the operation of the spacecraft.

As Kapton is used widely as an insulator for both thermal and electrical applications, ion implantation can have implications for the conductivity of the target material. The increasing carbonisation observed in the damaged samples in this work and that of the

literature [112, 114, 116, 137] could form a conductive layer of graphite or amorphous carbon. Determination of the effects of the ion implantation and plasma exposure to the conductivity as a large enough conductive layer could subvert the insulating properties of the Kapton.

As commented in the discussions in chapters 8 and 7, the S parameter depth profile measurements indicate that the damage in the Kapton samples extends to a deeper region in the samples than was investigated by the PALS measurements. Returning to the previously measured Kapton samples and performing additional high detail DBAR measurements and PALS measurements with a higher positron implantation energy would provide further information for the characterisation of the induced damage. As shown in the SRIM/TRIM simulations for the oxygen implantation in figures 7.1, 7.2, and 7.3, the implanted ions form a layer which is deeper than the region of maximum damage. The higher implantation energy PALS and DBAR measurements suggested would sample more of this observed extended damage region and provide further insight to the chemical environment.

The Kapton samples in which there are no observed lifetime after ion implantation and plasma exposure are intriguing as there is evidence to suggest defects are being filled by hydrogen from the plasma. The plasma exposure of the Kapton samples characterised in this work was 30 minutes so to further explore these effects the duration of the plasma exposure should be varied, in order to characterise the conditions necessary to start the defect filling process. As the only samples of Kapton that were exposed to plasma were implanted at a fluence of 1×10^{15} ions$\cdot cm^{-2}$, exposure of lower fluence ion implanted Kapton to hydrogen plasma would also contribute to a better understanding of the interaction between the hydrogen and the damaged Kapton matrix.

The preparation of the plasma exposed Kapton damaged by ion implantation was performed in two stages; the Kapton was implanted with ions then exposed to plasma. The effects of the plasma exposure to the induced damage from ion implantation were characterised in chapter 8, however it is unlikely that in a real environment the exposure to ions and plasma would be a discrete, separated process. To attempt to better understand the processes driving the observed damage, additional samples should be created with the plasma exposure performed before the ion implantation. The Kapton samples that were

exposed to plasma alone did not have any induced lifetimes found by PALS (as detailed in section 8.2), however the effects of the surface processing due to the plasma exposure could impact subsequent ion implantation, for example increasing the penetration depth of the ions, or increasing the induced damage in the near surface region.

Appendix A: Calibration data for the DBAR system

This section contains additional data used in the calibration of the HPGe crystal detector assembly used in the DBAR experiment.

A.1 Efficiency and Resolution Calibration

This section contains the data used to calibrate the photon energy dependent efficiency of the analogue DBAR detector system. Additionally the data from the measurements for efficiency were used to calibrate the resolution of the system from the well known peak energies in the radioactive sources.

Element	Source Activity (Bq)	Reference peak energy (keV)	Photons per 100 disintegrations	Measured Peak Area (Counts)	Peak area uncertainty (counts)	Scaled efficiency	Efficiency Uncertainty	Peak FWHM (keV)	FWHM uncertainty (keV)
Co60	18441.06	1173.228(3)	99.85(3)	737821	953	39.82	0.64	1.619	0.0021
		1332.492(4)	99.9826(6)	658844	917	35.51	0.51	1.697	0.0024
Eu152	23120.24	121.7817(3)	28.41(13)	937018	1020	141.23	8.00	0.883	0.0010
		244.6974(8)	7.55(4)	184827	494	104.83	4.48	1.008	0.0027
		344.2785(12)	26.59(12)	536388	743	86.38	3.00	1.085	0.0015
		367.7891(20)	0.862(5)	16159	219	80.27	3.77	1.114	0.0153
		411.1165(12)	2.238(10)	38703	257	74.05	2.43	1.127	0.0076
		443.965(3)	2.8(2)	51742	272	79.13	3.00	1.172	0.0062
		563.99(7)	0.457(13)	4535	179	42.49	3.53	1.121	0.0446
		656.489(5)	0.1437(18)	1214	144	36.18	18.93	1.223	0.1465
		778.9045(24)	12.97(6)	146083	405	48.23	0.95	1.403	0.0039
		867.38(3)	4.243(23)	42516	248	42.91	0.80	1.431	0.0084
		964.079(18)	14.5(6)	137372	408	40.57	0.70	1.528	0.0046
		1112.076(3)	13.41(6)	115714	367	36.95	0.56	1.598	0.0051
		1212.948(11)	1.416(9)	11097	140	33.56	0.63	1.424	0.0181
		1299.142(8)	1.633(9)	12334	129	32.34	0.53	1.613	0.0171
		1408.013(3)	20.85(8)	143724	413	29.52	0.36	1.732	0.0050
Ba133	25965.85	276.3989(12)	7.16(5)	190792	493	101.95	4.23	1.008	0.0026
		302.8508(5)	18.34(13)	461750	688	96.33	3.73	1.032	0.0015
		356.0129(7)	62.05(19)	1405513	1257	86.66	3.01	1.077	0.0010
		383.8485(12)	8.94(6)	195991	467	83.88	2.86	1.109	0.0027
		160.6121(16)	0.638(4)	25453	394	152.63	14.92	0.957	0.0149
		223.2368(13)	0.453(3)	12763	309	107.79	11.48	0.893	0.0218
Cs137	35185.36	661.657(3)	84.99(20)	394802	3086	64.50	1.92	1.314	0.0021

Table A.1: Calibration data for 7cm data

Element	Source Activity (Bq)	Reference peak energy (keV)	Photons per 100 disintegrations	Measured Peak Area (Counts)	Peak area uncertainty (counts)	Scaled efficiency	Efficiency Uncertainty	Peak FWHM (keV)	FWHM uncertainty (keV)
Co60	18441.06	1173.228(3)	99.85(3)	437103	696	23.63	0.22	1.625	0.0026
		1332.492(4)	99.9826(6)	394664	668	21.30	0.18	1.696	0.0029
Eu152	23120.24	121.7817(3)	28.41(13)	560390	894	85.08	2.91	0.887	0.0014
		244.6974(8)	7.55(4)	112610	460	64.33	1.73	0.98	0.0040
		344.2785(12)	26.59(12)	332147	629	53.88	1.17	1.082	0.0021
		367.7891(20)	0.862(5)	11896	230	59.52	2.74	1.063	0.0206
		411.1165(12)	2.238(10)	24077	254	46.40	1.10	1.109	0.0118
		443.965(3)	2.8(2)	31979	261	49.26	1.26	1.14	0.0093
		563.99(7)	0.457(13)	3889	164	36.70	2.92	0.889	0.0375
		656.489(5)	0.1437(18)						
		778.9045(24)	12.97(6)	94375	329	31.38	0.41	1.425	0.0050
		867.38(3)	4.243(23)	29003	214	29.48	0.40	1.481	0.0110
		964.079(18)	14.5(6)	93357	326	27.77	0.33	1.524	0.0053
		1112.076(3)	13.41(6)	76169	304	24.50	0.25	1.565	0.0063
		1212.948(11)	1.416(9)	7689	130	23.42	0.38	1.62	0.0275
		1299.142(8)	1.633(9)	8691	113	22.95	0.30	1.719	0.0223
		1408.013(3)	20.85(8)	100072	329	20.70	0.18	1.794	0.0059
Ba133	25965.85	276.3989(12)	7.16(5)	121237	423	65.05	1.75	1.004	0.0035
		302.8508(5)	18.34(13)	291973	583	61.16	1.51	1.022	0.0020
		356.0129(7)	62.05(19)	888738	975	55.03	1.21	1.071	0.0012
		383.8485(12)	8.94(6)	121443	388	52.19	1.12	1.091	0.0035
		160.6121(16)	0.638(4)	13582	394	81.78	8.31	0.881	0.0256
		223.2368(13)	0.453(3)	10015	321	84.93	10.29	1.007	0.0323
Cs137	35185.36	661.657(3)	84.99(20)	233639	2394	38.12	0.73	1.305	0.0027

Table A.2: Calibration data for 15cm data

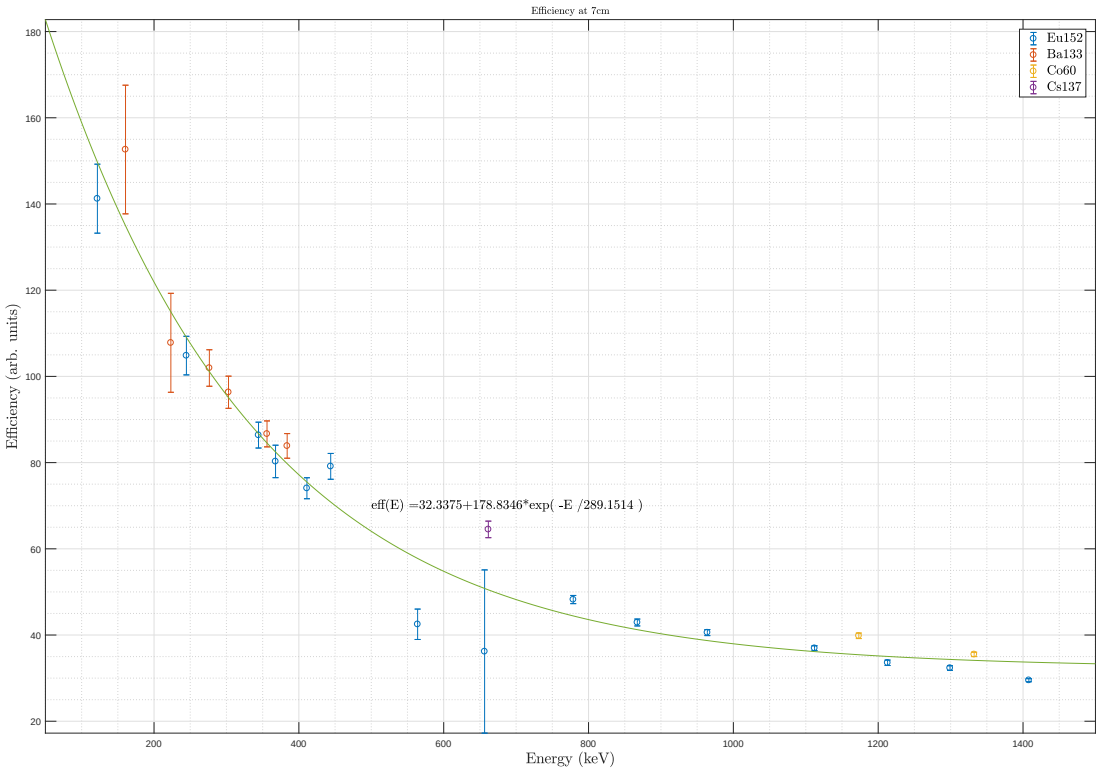

Figure A.1: Calculated efficiency with sources placed at 7cm from the detector endcap

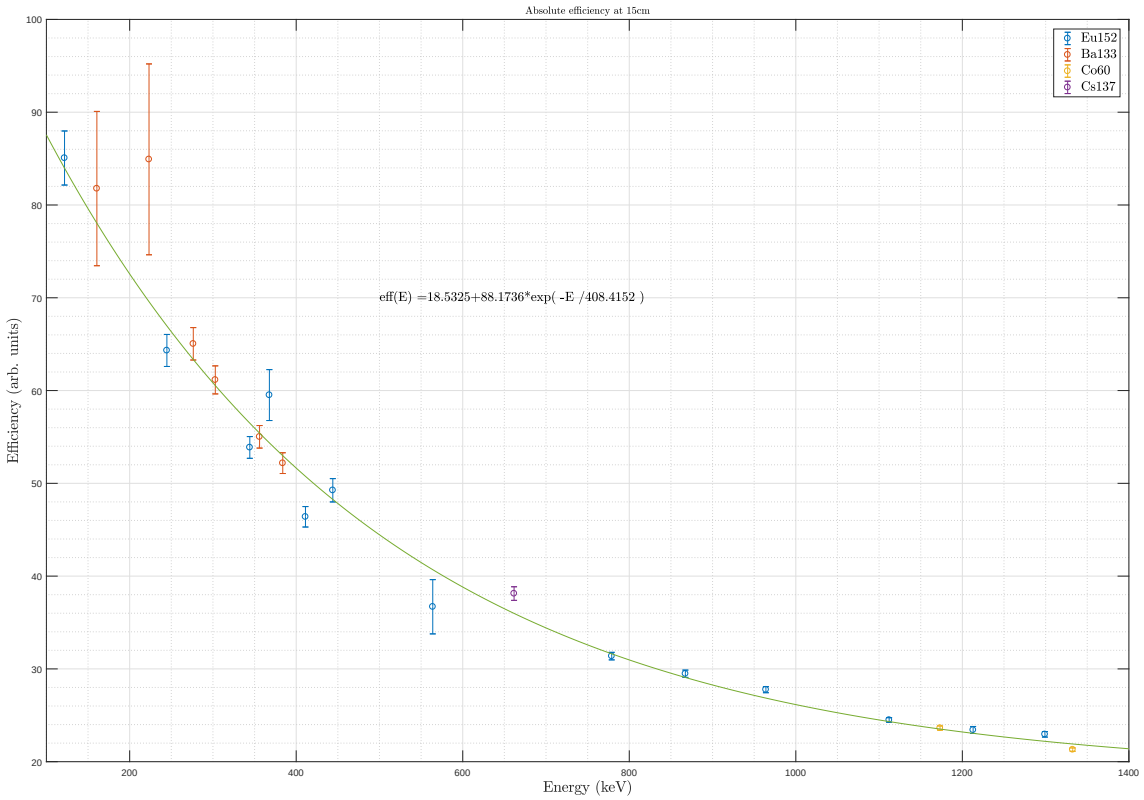

Figure A.2: Calculated detector efficiency with the souces placed 15cm from the detector endcap

Bibliography

[1] P. A. M. Dirac, "The quantum theory of the electron," Proceedings of the Royal Society of London A, vol. 117, no. 778, pp. 610–624, 1928.

[2] H. Weyl, "Gravitation and the Electron," Proceedings of the National Academy of Science, vol. 15, pp. 323–334, April 1929.

[3] P. A. M. Dirac, "A theory of electrons and protons," Proceedings of the Royal Society of London A, vol. 126, no. 801, pp. 360–365, 1930.

[4] P. A. M. Dirac, "On the annihilation of electrons and protons," Mathematical Proceedings of the Cambridge Philosophical Society, vol. 26, pp. 361–375, July 1930.

[5] J. R. Oppenheimer, "Two notes on the probability of radiative transitions," Phys. Rev., vol. 35, pp. 939–947, April 1930.

[6] P. A. M. Dirac, "Quantised singularities in the electromagnetic field," Proceedings of the Royal Society of London A, vol. 133, no. 821, pp. 60–72, 1931.

[7] C. D. Anderson, "The positive electron," Phys. Rev., vol. 43, pp. 491–494, March 1933.

[8] G. P. S. O. P. M. S. Blackett, "Some photographs of the tracks of penetrating radiation," Proceedings of the Royal Society of London A, vol. 139, no. 839, pp. 699–726, 1933.

[9] R. P. Feynman, "The theory of positrons," Phys. Rev., vol. 76, pp. 749–759, September 1949.

[10] Y. Nambu, "The use of the proper time in quantum electrodynamics I," Progress of Theoretical Physics, vol. 5, no. 1, pp. 82–94, 1950.

[11] C. Amsler, "Proton-antiproton annihilation and meson spectroscopy with the crystal barrel," Rev. Mod. Phys., vol. 70, pp. 1293–1339, October 1998.

[12] C. Amsler, D. S. Armstrong, I. Augustin, C. A. Baker, B. M. Barnett, C. J. Batty, K. Beuchert, P. Birien, J. Bistirlich, P. Blum, R. Bossingham, H. Bossy, K. Braune, J. Brose, D. V. Bugg, M. Burchell, T. Case, S. U. Chung, A. Cooper, K. M. Crowe, H. P. Dietz, S. v. Dombrowski, M. Doser, W. Dünnweber, D. Engelhardt, M. Englert, M. A. Faessler, C. Felix, G. Folger, R. Hackmann, R. P. Haddock, F. H. Heinsius, N. P. Hessey, P. Hidas, P. Illinger, D. Jamnik, Z. Jávorfi, H. Kalinowsky, B. Kämmle, T. Kiel, J. Kisiel, E. Klempt, M. Kobel, H. Koch, C. Kolo, K. Königsmann, M. Kunze, R. Landua, J. Lüdemann, H. Matthaey, M. Merkel, J. P. Merlo, C. A. Meyer, U. Meyer-Berkhout, L. Montanet, A. Noble, F. Ould-Saada, K. Peters, G. Pinter, S. Ravndal, A. H. Sanjari, E. Schäfer, B. Schmid, P. Schmidt, S. Spanier, C. Straßburger, U. Strohbusch, M. Suffert, D. Urner, C. Völcker, F. Walter, D. Walther, U. Wiedner, N. Winter, J. Zoll, and Č. Zupančič, "Antiproton-proton annihilation at rest into two-body final states," Zeitschrift für Physik C Particles and Fields, vol. 58, no. 2, pp. 175–189, 1993.

[13] A. Ore and J. L. Powell, "Three-photon annihilation of an electron-positron pair," Phys. Rev., vol. 75, pp. 1696–1699, June 1949.

[14] A. E. Ruark, "Positronium," Phys. Rev., vol. 68, pp. 278–278, December 1945.

[15] J. A. Wheeler, "Polyelectrons," Annals of the New York Academy of Sciences, vol. 48, no. 3, pp. 219–238, 1946.

[16] M. Deutsch, "Evidence for the formation of positronium in gases," Phys. Rev., vol. 82, pp. 455–456, May 1951.

[17] A. Deller, A. M. Alonso, B. S. Cooper, S. D. Hogan, and D. B. Cassidy, "Measurement of Rydberg positronium fluorescence lifetimes," Phys. Rev. A, vol. 93, p. 062513, June 2016.

[18] K. Michishio, R. Suzuki, K. Wada, I. Mochizuki, T. Hyodo, A. Yagishita, and Y. Nagashima, "Profiles of a positronium beam produced using the photodetachment of positronium negative ions," Nuclear Instruments and Methods in Physics Research Section A: Accelerators, Spectrometers, Detectors and Associated Equipment, vol. 785, pp. 5 – 8, 2015.

[19] M.-M. Bé, V. Chisté, C. Dulieu, X. Mougeot, E. Browne, V. Chechev, N. Kuzmenko, F. Kondev, A. Luca, M. Galán, A. Nichols, A. Arinc, and X. Huang, Table of Radionuclides, vol. 5 of Monographie BIPM-5. Pavillon de Breteuil, F-92310 Sèvres, France: Bureau International des Poids et Mesures, 2010.

[20] M. M. Alauddin, "Positron emission tomography (PET) imaging with ^{18}F-based radiotracers," Am J Nucl Med Mol Imaging, vol. 2, pp. 55–76, December 2011.

[21] R. M. Crocker, A. J. Ruiter, I. R. Seitenzahl, F. H. Panther, S. Sim, H. Baumgardt, A. Möller, D. M. Nataf, L. Ferrario, J. J. Eldridge, M. White, B. E. Tucker, and F. Aharonian, "Diffuse galactic antimatter from faint thermonuclear supernovae in old stellar populations," Nature Astronomy, vol. 1, p. 0135, May 2017.

[22] Y. Bordulev, R. Laptev, A. Lider, and M. Kroening, "Development of a digital spectrometric system for material studying by positron annihilation techniques," Proceedings 7th International Forum on Strategic Technology, 2012.

[23] R. J. Wilson and A. P. Mills, "Positron and positronium emission from tungsten (111)," Phys. Rev. B, vol. 27, pp. 3949–3954, April 1983.

[24] N. Zafar, J. Chevallier, G. Laricchia, and M. Charlton, "Single-crystal nickel foils as positron transmission-mode moderators," Journal of Physics D: Applied Physics, vol. 22, no. 6, p. 868, 1989.

[25] A. I. Williams, D. J. Murtagh, S. E. Fayer, S. L. Andersen, J. Chevallier, . Kövér, P. Van Reeth, J. W. Humberston, and G. Laricchia, "Moderation and diffusion of positrons in tungsten meshes and foils," Journal of Applied Physics, vol. 118, no. 10, 2015.

[26] A. P. Mills and E. M. Gullikson, "Solid neon moderator for producing slow positrons," Applied Physics Letters, vol. 49, no. 17, pp. 1121–1123, 1986.

[27] M. J. Puska and R. M. Nieminen, "Theory of positrons in solids and on solid surfaces," Rev. Mod. Phys., vol. 66, pp. 841–897, July 1994.

[28] A. Makhov, "The penetration of electrons into solids. 1. the intensity of an electron beam, transverse paths of electrons," Soviet Physics, Solid State, vol. 2, no. 9, pp. 1934–1941, 1961.

[29] A. Makhov, "The penetration of electrons into solids. 2. the distribution of electrons in depth," Soviet Physics, Solid State, vol. 2, no. 9, pp. 1942–1944, 1961.

[30] A. Vehanen, K. Saarinen, P. Hautojärvi, and H. Huomo, "Profiling multilayer structures with monoenergetic positrons," Phys. Rev. B, vol. 35, pp. 4606–4610, April 1987.

[31] S. Valkealahti and R. M. Nieminen, "Monte-carlo calculations of kev electron and positron slowing down in solids," Applied Physics A, vol. 32, no. 2, pp. 95–106, 1983.

[32] S. Valkealahti and R. M. Nieminen, "Monte Carlo calculations of keV electron and positron slowing down in solids. II," Applied Physics A, vol. 35, no. 1, pp. 51–59, 1984.

[33] V. Ghosh, "Positron implantation profiles in elemental and multilayer systems," Applied Surface Science, vol. 85, pp. 187 – 195, 1995.

[34] D. W. Gidley, H.-G. Peng, and R. S. Vallery, "Positron annihilation as a method to characterize porous materials," Annual Review of Materials Research, vol. 36, no. 1, pp. 49–79, 2006.

[35] R. E. Bell and R. L. Graham, "Time distribution of positron annihilation in liquids and solids," Phys. Rev., vol. 90, pp. 644–654, May 1953.

[36] D. J. Sprouster, C. Campbell, S. J. Buckman, G. Impellizzeri, E. Napolitani, S. Ruffell, and J. P. Sullivan, "Defect complexes in fluorine-implanted germanium," Journal of Physics D, vol. 46, no. 50, p. 505310, 2013.

[37] E. Vance, J. Davis, K. Olufson, D. Gregg, M. Blackford, G. Griffiths, I. Farnan, J. Sullivan, D. Sprouster, C. Campbell, and J. Hughes, "Leaching behaviour of and Cs disposition in a UMo powellite glass–ceramic," Journal of Nuclear Materials, vol. 448, no. 1–3, pp. 325 – 329, 2014.

[38] S. J. Tao, "Positronium annihilation in molecular substances," The Journal of Chemical Physics, vol. 56, no. 11, pp. 5499–5510, 1972.

[39] M. Eldrup, D. Lightbody, and J. Sherwood, "The temperature dependence of positron lifetimes in solid pivalic acid," Chemical Physics, vol. 63, no. 1–2, pp. 51 – 58, 1981.

[40] S. Thraenert, E. M. Hassan, D. Enke, D. Fuerst, and R. Krause-Rehberg, "Verifying the RTE model: ortho-positronium lifetime measurement on controlled pore glasses," Physica Status Solidi C, vol. 4, no. 10, pp. 3819–3822, 2007.

[41] K. Wada and T. Hyodo, "A simple shape-free model for pore-size estimation with positron annihilation lifetime spectroscopy," Journal of Physics: Conference Series, vol. 443, no. 1, p. 012003, 2013.

[42] A. Kawasuso, M. Hasegawa, M. Suezawa, S. Yamaguchi, and K. Sumino, "Charge state dependences of positron trapping rates associated with divacancies and vacancy-phosphorus pairs in si," Japanese Journal of Applied Physics, vol. 34, no. 5R, p. 2197, 1995.

[43] P. Mascher, S. Dannefaer, and D. Kerr, "Positron trapping rates and their temperature dependencies in electron-irradiated silicon," Phys. Rev. B, vol. 40, pp. 11764–11771, December 1989.

[44] M. Charlton and J. W. Humberston, Positron Physics. Cambridge Monographs on Atomic, Molecular and Chemical Physics, Cambridge University Press, 2000.

[45] S. J. Gilbert, C. Kurz, R. G. Greaves, and C. M. Surko, "Creation of a monoenergetic pulsed positron beam," Applied Physics Letters, vol. 70, no. 15, pp. 1944–1946, 1997.

[46] K. Saarinen and V. Ranki, "Identification of vacancy complexes in si by positron annihilation," Journal of Physics: Condensed Matter, vol. 15, no. 39, p. S2791, 2003.

[47] J. P. Sullivan, J. Roberts, R. W. Weed, M. R. Went, D. S. Newman, and S. J. Buckman, "A trap-based positron beamline for the study of materials," Measurement Science and Technology, vol. 21, no. 8, 2010.

[48] J. D. Baerdemaeker and C. Dauwe, "Development and application of the Ghent pulsed positron beam," Applied Surface Science, vol. 194, no. 1–4, pp. 52 – 55, 2002. 9th International Workshop on Slow Positron Beam Techniques for Solids and Surfaces.

[49] M. Maekawa and A. Kawasuso, "Development of pulsed positron beam line with compact pulsing system," Nuclear Instruments and Methods in Physics Research Section B: Beam Interactions with Materials and Atoms, vol. 270, pp. 23 – 27, 2012.

[50] K. Fallström and T. Laine, "Construction of the Helsinki University of Technology (HUT) pulsed positron beam," Applied Surface Science, vol. 149, no. 1–4, pp. 44 – 48, 1999.

[51] M. Yamawaki, Y. Kobayashi, K. Hattori, and Y. Watanabe, "Optimization of the scintillator size for positron lifetime measurements," Journal of Physics: Conference Series, vol. 443, no. 1, p. 012099, 2013.

[52] D. W. Gidley, W. E. Frieze, T. L. Dull, A. F. Yee, E. T. Ryan, and H.-M. Ho, "Positronium annihilation in mesoporous thin films," Phys. Rev. B, vol. 60, pp. R5157–R5160, August 1999.

[53] S. Szpala, P. Asoka-Kumar, B. Nielsen, J. P. Peng, S. Hayakawa, K. G. Lynn, and H.-J. Gossmann, "Defect identification using the core-electron contribution in Doppler-broadening spectroscopy of positron-annihilation radiation," Phys. Rev. B, vol. 54, pp. 4722–4731, August 1996.

[54] P. Asoka-Kumar, M. Alatalo, V. J. Ghosh, A. C. Kruseman, B. Nielsen, and K. G. Lynn, "Increased elemental specificity of positron annihilation spectra," Phys. Rev. Lett., vol. 77, pp. 2097–2100, September 1996.

[55] M. Alatalo, H. Kauppinen, K. Saarinen, M. J. Puska, J. Mäkinen, P. Hautojärvi, and R. M. Nieminen, "Identification of vacancy defects in compound semiconductors by core-electron annihilation: Application to InP," Phys. Rev. B, vol. 51, pp. 4176–4185, February 1995.

[56] S. DeBenedetti, C. E. Cowan, W. R. Konneker, and H. Primakoff, "On the angular distribution of two-photon annihilation radiation," Phys. Rev., vol. 77, pp. 205–212, January 1950.

[57] S. DeBenedetti, C. E. Cowan, and W. R. Konneker, "Angular distribution of annihilation radiation," Phys. Rev., vol. 76, pp. 440–440, August 1949.

[58] S. Eichler, J. Gebauer, F. Börner, A. Polity, R. Krause-Rehberg, E. Wendler, B. Weber, W. Wesch, and H. Börner, "Defects in silicon after B^+ implantation: A study using a positron-beam technique, Rutherford backscattering, secondary neutral mass spectroscopy, and infrared absorption spectroscopy," Phys. Rev. B, vol. 56, pp. 1393–1403, July 1997.

[59] R. S. Brusa, C. Macchi, S. Mariazzi, G. P. Karwasz, N. Laidani, R. Bartali, and M. Anderle, "Amorphous carbon film growth on Si: Correlation between stress and generation of defects into the substrate," Applied Physics Letters, vol. 86, no. 22, 2005.

[60] J. Čížek, M. Vlček, and I. Procházka, "Digital spectrometer for coincidence measurement of Doppler broadening of positron annihilation radiation," Nuclear Instruments and Methods in Physics Research Section A, vol. 623, no. 3, pp. 982 – 994, 2010.

[61] M. Haaks, T. Staab, and K. Maier, "Analyzing the high-momentum part of positron annihilation Doppler spectra with a single germanium detector," Nuclear Instruments and Methods in Physics Research Section A, vol. 569, no. 3, pp. 829 – 836, 2006.

[62] Y. Fukaya, M. Maekawa, A. Kawasuso, I. Mochizuki, K. Wada, T. Shidara, A. Ichimiya, and T. Hyodo, "Total reflection high-energy positron diffraction: An ideal diffraction technique for surface structure analysis," Applied Physics Express, vol. 7, no. 5, p. 056601, 2014.

[63] H. Ceeh, J. A. Weber, M. Leitner, P. Böni, and C. Hugenschmidt, "The source-sample stage of the new two-dimensional angular correlation of annihilation radiation spectrometer at Technische Universität München," Review of Scientific Instruments, vol. 84, no. 4, p. 043905, 2013.

[64] K. Inoue, Y. Nagai, Z. Tang, T. Toyama, Y. Hosoda, A. Tsuto, and M. Hasegawa, "Time evolution of positron affinity trapping at embedded nanoparticles by age-momentum correlation," Phys. Rev. B, vol. 83, p. 115459, March 2011.

[65] T. J. Murphy and C. M. Surko, "Positron trapping in an electrostatic well by inelastic collisions with nitrogen molecules," Phys. Rev. A, vol. 46, pp. 5696–5705, November 1992.

[66] A. P. Mills, "Time bunching of slow positrons for annihilation lifetime and pulsed laser photon absorption experiments," Applied physics, vol. 22, pp. 273–276, July 1980.

[67] J. F. Ziegler and J. P. Biersack, "The stopping and range of ions in matter," in Treatise on Heavy-Ion Science (D. Bromley, ed.), pp. 93–129, Springer US, 1985.

[68] J. F. Ziegler, "SRIM-2003," Nuclear Instruments and Methods in Physics Research Section B, vol. 219 – 220, pp. 1027 – 1036, 2004.

[69] P. T. Pinard, H. Demers, F. Salvat, and R. Gauvin, "pyPENELOPE." http://pypenelope.sourceforge.net/, 2006. Accessed: 2018.

[70] J. Roberts, Positron annihilation lifetime studies of inorganic materials using a new positron beamline. PhD thesis, Research School of Physics and Engineering, November 2012.

[71] G. F. Knoll, Radiation detection and measurement. John Wiley & Sons, 2010.

[72] Amptek, "Multichannel analyzer pocket MCA MCA8000A." http://www.amptek.com/pdf/mca8000a.pdf, 2005. Accessed: 2016.

[73] Amptek, "ADMCA multichannel analyzer software." http://amptek.com/mca8000a-multichannel-analyzer-software-downloads/, 2005. Accessed: 2016.

[74] M.-M. Bé, V. Chisté, C. Dulieu, E. Browne, V. Chechev, N. Kuzmenko, R. Helmer, A. Nichols, E. Schönfeld, and R. Dersch, Table of Radionuclides, vol. 2 of Monographie BIPM-5. Pavillon de Breteuil, F-92310 Sèvres, France: Bureau International des Poids et Mesures, 2004.

[75] A. Garnsworthy, C. Pearson, D. Bishop, B. Shaw, J. Smith, M. Bowry, V. Bildstein, G. Hackman, P. Garrett, Y. Linn, J.-P. Martin, W. Mills, and C. Svensson, "The GRIFFIN data acquisition system," Nuclear Instruments and Methods in Physics Research Section A: Accelerators, Spectrometers, Detectors and Associated Equipment, vol. 853, pp. 85 – 104, 2017.

[76] S. Korolczuk, S. Mianowski, J. Rzadkiewicz, P. Sibczynski, L. Swiderski, and I. Zychor, "Digital acquisition in high count rate gamma-ray spectrometry," IEEE Transactions on Nuclear Science, vol. 63, pp. 1668–1673, June 2016.

[77] Tektronics, "Information regarding HiRes operation mode." https://www.tek.com/support/faqs/i-could-not-find-any-information-regarding-increase-bits-resolution-hires-mode-there-an/. Accessed: February 2014.

[78] MATLAB, version 9.1.0.441655 (R2016b). Natick, Massachusetts: The MathWorks Inc., 2016.

[79] G. Rossum, Python Reference Manual. Amsterdam, The Netherlands, The Netherlands: CWI (Centre for Mathematics and Computer Science), 1995.

[80] B. Gough, GNU Scientific Library Reference Manual - Third Edition. Network Theory Ltd., 3rd ed., 2009.

[81] S. Bochkanov, "ALGLIB." http://www.alglib.net/. Accessed: 2015.

[82] W. G. Cochran, "The χ^2 test of goodness of fit," Ann. Math. Statist., vol. 23, pp. 315–345, September 1952.

[83] M. S. P. Toolbox, version 9.1.0.441655 (R2016b). Natick, Massachusetts: The MathWorks Inc., 2016.

[84] J. Kaiser and R. Schafer, "On the use of the I_0-Sinh window for spectrum analysis," IEEE Transactions on Acoustics, Speech, and Signal Processing, vol. 28, pp. 105–107, February 1980.

[85] P. Welch, "The use of fast Fourier transform for the estimation of power spectra: A method based on time averaging over short, modified periodograms," IEEE Transactions on Audio and Electroacoustics, vol. 15, pp. 70–73, June 1967.

[86] M.-M. Bé, V. Chisté, C. Dulieu, E. Browne, C. Baglin, V. Chechev, N. Kuzmenko, R. Helmer, F. Kondev, D. MacMahon, and K. Lee, Table of Radionuclides, vol. 3 of Monographie BIPM-5. Pavillon de Breteuil, F-92310 Sèvres, France: Bureau International des Poids et Mesures, 2006.

[87] M.-M. Bé, V. Chisté, C. Dulieu, E. Browne, V. Chechev, N. Kuzmenko, R. Helmer, A. Nichols, E. Schönfeld, and R. Dersch, Table of Radionuclides, vol. 1 of Monographie BIPM-5. Pavillon de Breteuil, F-92310 Sèvres, France: Bureau International des Poids et Mesures, 2004.

[88] L. Varnell and J. Trischuk, "A peak-fitting and calibration program for ge(li) detectors," Nuclear Instruments and Methods, vol. 76, no. 1, pp. 109 – 114, 1969.

[89] M. Statistics and M. L. Toolbox, version 9.1.0.441655 (R2016b). Natick, Massachusetts: The MathWorks Inc., 2016.

[90] V. T. Jordanov and G. F. Knoll, "Digital synthesis of pulse shapes in real time for high resolution radiation spectroscopy," Nuclear Instruments and Methods in Physics Research Section A, vol. 345, no. 2, pp. 337 – 345, 1994.

[91] J. Stein, F. Scheuer, W. Gast, and A. Georgiev, "X-ray detectors with digitized preamplifiers," Nuclear Instruments and Methods in Physics Research Section B, vol. 113, no. 1–4, pp. 141 – 145, 1996.

[92] E. Gramsch, K. G. Lynn, J. Throwe, and I. Kanazawa, "Positron diffusion in solid and liquid metals," Phys. Rev. B, vol. 59, pp. 14282–14301, June 1999.

[93] E. Soininen, H. Huomo, P. A. Huttunen, J. Mäkinen, A. Vehanen, and P. Hautojärvi, "Temperature dependence of positron diffusion in cubic metals," Phys. Rev. B, vol. 41, pp. 6227–6233, April 1990.

[94] E. Soininen, J. Mäkinen, D. Beyer, and P. Hautojärvi, "High-temperature positron diffusion in Si, GaAs, and Ge," Phys. Rev. B, vol. 46, pp. 13104–13118, November 1992.

[95] A. Vehanen, K. G. Lynn, P. J. Schultz, E. Cartier, H.-J. Güntherodt, and D. M. Parkin, "Variable-energy positron studies of metallic glasses," Phys. Rev. B, vol. 29, pp. 2371–2381, March 1984.

[96] C. Palacio, J. D. Baerdemaeker, and C. Dauwe, "Determination of the positron diffusion length in Kapton by analysing the positronium emission," Applied Surface Science, vol. 255, no. 1, pp. 213 – 216, 2008. Proceedings of the Eleventh International Workshop on Slow Positron Beam Techniques for Solids and Surfaces.

[97] S. Pendyala and J. W. McGowan, "Diffusion of slow positrons from gold," Canadian Journal of Physics, vol. 52, no. 12, pp. 1051–1056, 1974.

[98] A. Vehanen, K. G. Lynn, P. J. Schultz, and M. Eldrup, "Improved slow-positron yield using a single crystal tungsten moderator," Applied Physics A, vol. 32, no. 3, pp. 163–167, 1983.

[99] H. Huomo, E. Soininen, and A. Vehanen, "Analysis of positron diffusion data," Applied Physics A, vol. 49, no. 6, pp. 647–658, 1989.

[100] M. Alatalo, B. Barbiellini, M. Hakala, H. Kauppinen, T. Korhonen, M. J. Puska, K. Saarinen, P. Hautojärvi, and R. M. Nieminen, "Theoretical and experimental study of positron annihilation with core electrons in solids," Phys. Rev. B, vol. 54, pp. 2397–2409, July 1996.

[101] DuPont, "Kapton polyimide film general specifications." http://www.dupont.com/content/dam/assets/products-and-services/membranes-films/assets/DEC-Kapton-general-specs.pdf, 2012. Accessed: 2015.

[102] DuPont, "Kapton HN polyimide film technical datasheet." http://www.dupont.com/content/dam/assets/products-and-services/membranes-films/assets/DEC-Kapton-HN-datasheet.pdf, 2011. Accessed: 2015.

[103] M. A. Monge and J. del Rio, "Position annihilation in Kapton source-supporting foils," Journal of Physics: Condensed Matter, vol. 6, no. 13, p. 2643, 1994.

[104] T. Kinkeldei, N. Muenzenrieder, C. Zysset, K. Cherenack, and G. Troester, "Encapsulation for flexible electronic devices," IEEE Electron Device Letters, vol. 32, pp. 1743–1745, December 2011.

[105] J. P. Gardner, J. C. Mather, M. Clampin, R. Doyon, M. A. Greenhouse, H. B. Hammel, J. B. Hutchings, P. Jakobsen, S. J. Lilly, K. S. Long, J. I. Lunine, M. J. Mccaughrean, M. Mountain, J. Nella, G. H. Rieke, M. J. Rieke, H.-W. Rix, E. P. Smith, G. Sonneborn, M. Stiavelli, H. S. Stockman, R. A. Windhorst, and G. S. Wright, "The James Webb Space Telescope," Space Science Reviews, vol. 123, pp. 485–606, April 2006.

[106] J. E. Lincoln, R. J. Morgan, and E. E. Shin, "Effect of thermal history on the deformation and failure of polyimides," Journal of Polymer Science Part B, vol. 39, no. 23, pp. 2947–2959, 2001.

[107] A. C. Lua and J. Su, "Structural changes and development of transport properties during the conversion of a polyimide membrane to a carbon membrane," Journal of Applied Polymer Science, vol. 113, no. 1, pp. 235–242, 2009.

[108] D. C. Ferguson, U. S. N. Aeronautics, and S. Administration, Laboratory degradation of Kapton in a low energy oxygen ion beam. Washington, D.C. : National Aeronautics and Space Administration, 1983.

[109] J.-P. Jeun, J.-W. Shin, Y.-C. Nho, and P.-H. Kang, "The effect of Ne+ ion implantation on polyimide film," Journal of Industrial and Engineering Chemistry, vol. 15, no. 1, pp. 56 – 61, 2009.

[110] D. Xu, X. Xu, and S. Zou, "Structural investigation of aromatic polyimide films modified by ion beams: A comparative study," Applied Physics Letters, vol. 59, no. 24, pp. 3110–3112, 1991.

[111] S. F. Ahmed, K.-R. Lee, J. il Yoon, and M.-W. Moon, "Nanoporous structures of polyimide induced by Ar ion beam irradiation," Applied Surface Science, vol. 258, no. 8, pp. 3841 – 3845, 2012.

[112] J.-P. Salvetat, J.-M. Costantini, F. Brisard, and L. Zuppiroli, "Onset and growth of conduction in polyimide Kapton induced by swift heavy-ion irradiation," Phys. Rev. B, vol. 55, pp. 6238–6248, March 1997.

[113] N. Mathakari, V. Jadhav, D. Kanjilal, V. Bhoraskar, and S. Dhole, "Surface and structural changes in polyimide by 100 MeV Ag^{7+} ion irradiation," Surface and Coatings Technology, vol. 203, no. 17–18, pp. 2620 – 2624, 2009. SMMIB-15 15th International Conference on Surface Modification of Materials by Ion Beams.

[114] J. Shi, C. Gong, X. Tian, S. Yang, and P. K. Chu, "Optical properties and chemical structures of Kapton-H film after proton irradiation by immersion in a hydrogen plasma," Applied Surface Science, vol. 258, no. 8, pp. 3829 – 3834, 2012.

[115] B. Lamontagne, A. M. Wrobel, G. Jalbert, and M. R. Wertheimer, "Large-area microwave plasma etching of polyimide," Journal of Physics D: Applied Physics, vol. 20, no. 7, p. 844, 1987.

[116] S. Lee, Y.-C. Tien, and C.-F. Hsu, "FTIR analysis of plasma damage of Kapton," Plasmas and Polymers, vol. 4, pp. 229–239, September 1999.

[117] C. Sun, Y. Wu, J. Xiao, R. Li, D. Yang, and S. He, "Pyrolytic carbon free-radical evolution and irradiation damage of polyimide under low-energy proton irradiation," Journal of Applied Physics, vol. 110, no. 12, 2011.

[118] J. Sampaio, E. Wnuk, R. Vilhena de Moraes, and S. Fernandes, "Resonant orbital dynamics in LEO region: Space debris in focus," Mathematical Problems in Engineering, vol. 2014, pp. 1–12, January 2014.

[119] N. Y. Ganushkina, I. Dandouras, Y. Y. Shprits, and J. Cao, "Locations of boundaries of outer and inner radiation belts as observed by cluster and double star," Journal of Geophysical Research: Space Physics, vol. 116, no. A9, pp. n/a–n/a, 2011. A09234.

[120] S. Bourdarie and M. Xapsos, "The near-Earth space radiation environment," IEEE Transactions on Nuclear Science, vol. 55, pp. 1810–1832, August 2008.

[121] W. L. Imhof and R. V. Smith, "Proton intensities and energy spectrums in the inner Van Allen belt," Journal of Geophysical Research, vol. 69, no. 1, pp. 91–100, 1964.

[122] J. F. Fennell, S. G. Claudepierre, J. B. Blake, T. P. O'Brien, J. H. Clemmons, D. N. Baker, H. E. Spence, and G. D. Reeves, "Van Allen probes show that the inner radiation zone contains no MeV electrons: ECT/MagEIS data," Geophysical Research Letters, vol. 42, no. 5, pp. 1283–1289, 2015. 2014GL062874.

[123] Z. Su, F. Xiao, H. Zheng, Z. He, H. Zhu, M. Zhang, C. Shen, Y. Wang, S. Wang, C. A. Kletzing, W. S. Kurth, G. B. Hospodarsky, H. E. Spence, G. D. Reeves, H. O. Funsten, J. B. Blake, and D. N. Baker, "Nonstorm time dynamics of electron radiation belts observed by the Van Allen probes," Geophysical Research Letters, vol. 41, no. 2, pp. 229–235, 2014.

[124] E. Benton and E. Benton, "Space radiation dosimetry in low-Earth orbit and beyond," Nuclear Instruments and Methods in Physics Research Section B, no. 1–2, pp. 255 – 294, 2001. Advanced Topics in Solid State Dosimetry.

[125] S. T. Lepri, E. Landi, and T. H. Zurbuchen, "Solar wind heavy ions over solar cycle 23: ACE/SWICS measurements," The Astrophysical Journal, vol. 768, no. 1, p. 94, 2013.

[126] R. von Steiger and T. H. Zurbuchen, "Kinetic properties of heavy solar wind ions from Ulysses-SWICS," Geophysical Research Letters, vol. 33, no. 9, pp. n/a–n/a, 2006. L09103.

[127] A. J. Watt, A. H. Hayes, B. A. King, R. G. Elliman, and D. C. Weisser, "The design and construction of a low energy ion implanter and ion source test facility," in 10th Australian conference on nuclear techniques of analysis Proceedings, (Australia), p. 244, 1998.

[128] B. D. Blackwell, J. F. Caneses, C. M. Samuell, J. Wach, J. Howard, and C. Corr, "Design and characterization of the Magnetized Plasma Interaction Experiment (MAGPIE): a new source for plasma-material interaction studies," Plasma Sources Science and Technology, vol. 21, no. 5, p. 055033, 2012.

[129] S. McGuire and D. J. Keeble, "Positron lifetime and implantation in kapton," Journal of Physics D, vol. 39, no. 15, p. 3388, 2006.

[130] B. C. Tee, C. Wang, R. Allen, and Z. Bao, "An electrically and mechanically self-healing composite with pressure-and flexion-sensitive properties for electronic skin applications," Nature nanotechnology, vol. 7, no. 12, p. 825, 2012.

[131] X. F. Lei, Y. Chen, H. P. Zhang, X. J. Li, P. Yao, and Q. Y. Zhang, "Space survivable polyimides with excellent optical transparency and self-healing properties derived from hyperbranched polysiloxane," ACS Applied Materials & Interfaces, vol. 5, no. 20, pp. 10207–10220, 2013. PMID: 24040935.

[132] A. N. Hammoud, E. D. Baumann, E. Overton, I. T. Myers, J. L. Suthar, W. Khachen, and J. R. Laghari, "High temperature dielectric properties of apical, kapton, peek, teflon af, and upilex polymers," in [Proceedings] 1992 Annual Report: Conference on Electrical Insulation and Dielectric Phenomena, pp. 549–554, October 1992.

[133] G. Dlubek, R. Buchhold, C. Hübner, A. Nakladal, and K. Sahre, "Local free volumes in boron-bombarded Kapton polyimide: A positron lifetime study," Journal of Polymer Science Part B, vol. 37, no. 17, pp. 2539–2543, 1999.

[134] C. M. Samuell and C. S. Corr, "Atomic and molecular hydrogen gas temperatures in a low-pressure helicon plasma," Plasma Sources Science and Technology, vol. 24, no. 4, p. 045003, 2015.

[135] E. Smith and G. Dent, Modern Raman spectroscopy: a practical approach. John Wiley & Sons, 2013.

[136] P. R. Griffiths and J. A. De Haseth, Fourier transform infrared spectrometry, vol. 171. John Wiley & Sons, 2007.

[137] M. Mikhailov, L. Dundun, and J. Dechuan, "Study of the optical properties of a reflecting coating prepared from a Kapton film with deposited aluminum," Russian Physics Journal, vol. 43, no. 7, pp. 552–557, 2000.